

UNCLASSIFIED

AD NUMBER

AD869325

LIMITATION CHANGES

TO:

Approved for public release; distribution is unlimited.

FROM:

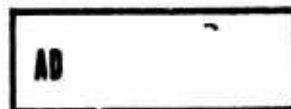
Distribution authorized to U.S. Gov't. agencies and their contractors; Critical Technology; FEB 1970. Other requests shall be referred to Army Aviation Materiel Laboratories, Fort Eustis, VA 23604. This document contains export-controlled technical data.

AUTHORITY

usaamrl ltr, 23 jun 1971

THIS PAGE IS UNCLASSIFIED

AD 869325



USAAVLABS TECHNICAL REPORT 70-5

A FEASIBILITY STUDY OF A HIGH-SPEED BURNER

By

Irving Fruchtman

February 1970

U. S. ARMY AVIATION MATERIEL LABORATORIES
FORT EUSTIS, VIRGINIA

CONTRACT DAAJ02-68-C-0092

GENERAL APPLIED SCIENCE LABORATORIES, INC.
SUBSIDIARY OF THE MARQUARDT COMPANY
WESTBURY, L. I., NEW YORK

This document is subject to special export controls, and each transmittal to foreign governments or foreign nationals may be made only with prior approval of US Army Aviation Materiel Laboratories, Fort Eustis, Virginia 23604.



136

Disclaimers

The findings in this report are not to be construed as an official Department of the Army position unless so designated by other authorized documents.

When Government drawings, specifications, or other data are used for any purpose other than in connection with a definitely related Government procurement operation, the United States Government thereby incurs no responsibility nor any obligation whatsoever; and the fact that the Government may have formulated, furnished, or in any way supplied the said drawings, specifications, or other data is not to be regarded by implication or otherwise as in any manner licensing the holder or any other person or corporation, or conveying any rights or permission, to manufacture, use, or sell any patented invention that may in any way be related thereto.

Disposition Instructions

Destroy this report when no longer needed. Do not return it to the originator.

ACCESSION FOR		
CPSTI	WHITE SECTION	<input type="checkbox"/>
DDC	DIFF SECTION	<input checked="" type="checkbox"/>
UNANNOUNCED		<input type="checkbox"/>
JUSTIFICATION		
CY		
DISTRIBUTION/AVAILABILITY CODES		
DIST.	AVAIL.	END. OR SPECIAL
2		



DEPARTMENT OF THE ARMY
HEADQUARTERS US ARMY AVIATION MATERIEL LABORATORIES
FORT EUSTIS, VIRGINIA 23604

This report was prepared by the General Applied Science Laboratories (GASL) under the terms of Contract DAAJ02-68-C-0092. It consists of a discussion and presentation of findings along with the approach followed to design, fabricate, and test a high-speed burner for turbomachine applications. The unique feature of a high-speed burner is that the combustion process can take place at higher Mach numbers than it can with current gas turbine combustion systems. Being able to conduct the burning process at higher Mach numbers will reduce the diffusion requirements of a compressor diffuser, therefore resulting in a more efficient compressor diffuser and combustor system.

The object of this contractual effort was to determine the feasibility of a high-speed combustion chamber having a burner entrance Mach number of approximately 0.5.

In general, this experimental effort resulted in the demonstration of ignition and partial combustion of liquid JP-4 fuel with burner entrance Mach numbers as high as 1.0.

The conclusion and recommendations contained herein are concurred in by this Command. This concurrence does not imply that a high-speed burner is practical for gas turbine applications. However, it is believed that the concept shows some promise, and further investigations will be required to prove or disprove the practicability of such a system.

Task 1G162204A01409
Contract DAAJ02-68-C-0092
USAAVLABS Technical Report 70-5
February 1970

A FEASIBILITY STUDY OF A HIGH-SPEED BURNER

Final Report

GASL Technical Report 730

By

Irving Fruchtman

Prepared by

General Applied Science Laboratories, Inc.
Subsidiary of The Marquardt Company
Westbury, L.I., New York

for

U. S. ARMY AVIATION MATERIEL LABORATORIES
FORT EUSTIS, VIRGINIA

This document is subject to special export controls, and each transmittal to foreign governments or foreign nationals may be made only with prior approval of U.S. Army Aviation Materiel Laboratories, Fort Eustis, Virginia 23604.

ABSTRACT

The theoretical analyses, the design, and the experimental verification of a high-speed combustion chamber are described. For turbomachines, this type of burner is used when compressor outflow speed is so high that diffusion to low speed presents severe pressure loss penalties. The present study showed that for a low-mass-flow, high-pressure-ratio turbomachine, combined diffuser and combustor losses are minimum for a burner entrance Mach number of about 0.5. The use of the GASL finite rate chemistry and turbulent mixing programs is discussed along with the combustor modeling and flame spread predictions. Finally, a series of experiments is described, and burner pressure loss and temperature profiles are shown over a wide range of burner airflow conditions, i.e., pressures from 1 to 11 atmospheres and inlet air temperatures from ambient to 1200°R.

FOREWORD

The work reported here was conducted for the U. S. Army Aviation Materiel Laboratories and was authorized by Task 1G162204A01409 under Contract Number DAAJ02-68-C-0092.

The author is indebted to the staff of General Applied Science Laboratories, Inc. for their able assistance, and in particular to Mr. Eli Reiss for his help in facility design and experiments. Also gratefully acknowledged is the help and guidance of Messrs. Nicholas Kailos, Lawrence Bell, and David Cale of the U. S. Army Aviation Materiel Laboratories.

BLANK PAGE

TABLE OF CONTENTS

	<u>Page</u>
ABSTRACT	iii
FOREWORD	v
LIST OF ILLUSTRATIONS	ix
LIST OF TABLES	xiii
LIST OF SYMBOLS	xiv
I. INTRODUCTION	1
II. BURNER INLET CONDITIONS	3
Off-Design	3
Estimation of Combustor Performance . . .	4
Diffuser - Turning Loss Model and Evaluation of Optimum Burner Entrance Conditions	17
Method of Computing Burner Off-Design Performance	27
III. BURNER DESIGN	32
Ignition	33
Fuel Injection	35
Jet Breakup	35
Heat-Up	38
Combustion	43
IV. DESCRIPTION OF FACILITY	55
Test Setup	55
Instrumentation	62
V. PRESENTATION AND DISCUSSION OF THE EXPERIMENTAL DATA	67

	<u>Page</u>
Temperature Distribution	69
Static Pressure Distribution	75
Total Pressure	75
Comparison of Experiment and Theory . . .	83
VI. CONCLUSIONS AND RECOMMENDATIONS	85
LITERATURE CITED	86
APPENDIXES	
I. Flame Stabilization and Ignition . .	89
II. Review of Mixing Analysis	95
III. Review of Finite-Rate Chemical Kinetics	98
IV. Heat Transfer Analysis	103
V. Thermocouple-Probe Correction	111
VI. Total Temperature Distribution Data .	114
DISTRIBUTION	117

LIST OF ILLUSTRATIONS

<u>Figure</u>		<u>Page</u>
1	Burner Exit Mach Number - Constant Pressure Burning	7
2	Burner Area Ratio - Constant Pressure Burning	8
3	Burner Recovery - Constant Pressure Burning	10
4	Fuel-Air Ratio vs Altitude at Various Power Levels	11
5	Burner Recovery - Constant-Mach-Number Burning	13
6	Burner Area Ratio - Constant-Mach-Number Burning	14
7	Burner Pressure Ratio - Constant-Mach-Number Burning	15
8	Burner Recovery - Constant-Area Burning	18
9	Burner Exit Mach Number - Constant-Area Burning	19
10	Burner Static Pressure Ratio - Constant-Area Burning	20
11	Comparison of Pressure Recovery Generated by Each Burner Model	21
12	Diffuser Recovery - For an Expansion From $M_{2\alpha} = 0.8$ to $M_{2\beta}$	25
13	Combined Diffuser and Combustor Pressure Recovery vs Burner Inlet Mach Number	26

<u>Figure</u>		<u>Page</u>
14	Compressor Rotor Outlet Mach Number vs Pressure Ratio	29
15	Burner Inlet Mach Number vs percentage of Power, Mach Number = 0.5 at Maximum Power	30
16	Diffuser, Burner, and Combined Recovery vs Percentage of Power, Design Mach Number =0.5.	31
17	Ignition and Fuel Injection Systems . . .	34
18	Calculated Fuel-Air Ratio at Slot Region.	42
19	Definitions of Coordinate System	44
20	Isotherms Produced by Saturated Fuel- Air Layer	49
21	Flame Propagation With Stoichiometric Fuel Layer	50
22	Temperature Profiles at Various Axial Stations	51
23	Isotherms Produced by "Low" Temperature Pilot f/a = 0.0405 Fuel-Air Layer	53
24	Drawing of Typical Igniter and Flameholder Slot	54
25	Schematic of Test Facility	56
26	Burner Centerbody	58
27	Viewing Port and Instrument Port Housing	59

<u>Figure</u>		<u>Page</u>
28	Detail Drawing of Igniter Region	60
29	Layout of Main Fuel Injector Configuration	61
30	Typical Plug Mass Flow Rates	63
31	Fuel Piping Schematic for Army/GASL Combustor	64
32	Calibration Results of Cavitating Venturis	66
33	Definition of Circumferential Stations . .	68
34	Circumferential Temperature Distribution, 25,000 ft, 100 Percent Power	71
35	Circumferential Temperature Distribution, 25,000 ft, 60 Percent Power	72
36	Circumferential Temperature Distribution, Sea Level, 100 Percent Power	73
37	Circumferential Temperature Distribution, Sea Level, 60 Percent Power	74
38	Axial Static Pressure Distribution With and Without Burning, $M_3=0.48$, $P_3=128$ psia.	76
39	Axial Distribution of Static Pressure, $M = 0.58$, No Burning	77
40	Burner Pressure Recovery vs Mach Number, $\theta = 0^\circ$	78
41	Burner Pressure Recovery vs Mach Number, $\theta = 30^\circ$	79

<u>Figure</u>		<u>Page</u>
42	Burner Pressure Recovery vs Inlet Mach Number, $\theta = 90^\circ$	80
43	Circumferential Burner Pressure Recovery, $M_3 = 0.5$	81
44	Effect of Burner Mach Number on Pressure Recovery, $f/a = 0.018$	82
45	Comparison of Experiment With Theoretical Constant Pressure Burner Recovery, $M_3 = 0.5$	84
46	Flameholder Stability Limits	93
47	Effect of Wall Temperature on Heat Flux	104
48	Effect of Heat Flux on Coolant- Side Wall Temperature	105
49	Effect of Heat Flux on JP-4 Coolant Fuel-Side Wall Temperature	107
50	Temperature of Combustor Wall	108
51	Effect of Heat Flux on Wall Temperature $\tau = 60$ seconds	109
52	Thermocouple Probe Correction Chart	113

LIST OF TABLES

<u>Table</u>		<u>Page</u>
I	Engine Parameters	2
II	Off-Design Conditions	4
III	Unmixed Air and Fuel Conditions	46
IV	Definition of Flow Quantities at the Igniter Station	47
V	Inlet Conditions for Army/GASL High- Speed Combustion Testing	69
VI	Summary of Blunt-Trailing-Edge Flame- holder Work	91
VII	Solutions to the Diffusion Equation	95
VIII	Reaction Mechanism	100
IX	Thermocouple Lead Wire Characteristics	112
X	Data Log: Altitude, 100 Percent Power Condition	114
XI	Data Log: Altitude, 60 Percent Power Condition	115
XII	Data Log: Sea Level, 100 Percent Power Condition	115
XIII	Data Log: Sea Level, 60 Percent Power Condition	116

LIST OF SYMBOLS

A	area, ft^2 or in^2
A_R	area ratio
a^*	critical speed, ft/sec
C_D	drag coefficient
C_j	molar concentration of the j^{th} specie
C_p	specific heat $\text{BTU}/\text{lbm}, ^\circ\text{R}$
D	flame holder depth, ft
D_T	turbulent diffusion coefficient, ft^2/sec
d_o	orifice diameter, ft
D_M	maximum droplet diameter, ft
D_{30}	volumetric mean droplet diameter, ft
E	activation energy, cal/mole
e	static enthalpy, BTU/lbm
F	parameter defined by Equation (28)
f/a	fuel-air, mass ratio
g	gravitational constant $32.2 \text{ lbm}, \text{ft}/\text{lbf}, \text{sec}^2$
H	total enthalpy, BTU/lbm
h	heat transfer coefficient, $\text{BTU}/\text{ft}^2, \text{sec}, ^\circ\text{R}$
I_o	modified Bessel function of the first kind, zero order
J_o	Bessel function, zero order
K	factor defined by Equation (76)
K_r	reaction rate constant
k	thermal conductivity, $\text{BTU}/\text{ft}, ^\circ\text{R}, \text{sec}$

L	diffuser length, ft
h	heat of vaporization, BTU/lbm
M	Mach number
M_a	mass flux of air, lbm/sec, ft ²
MW	molecular weight
\dot{m}	mass flow, lbm/sec
N_{Nu}	Nusselt number
N_{Pr}	Prandtl number
N_{Re}	Reynolds number
N_{We}	Weber number
P	stagnation pressure, psia
p	static pressure, psia
P	partial pressure, psia
q	dynamic pressure, psia
$q_{conv}, q_{rad}, q_{cond}$	= convection, radiation, conductive heat flux, respectively, BTU/sec
R	gas constant, 1544/MW
\bar{R}	duct radius, ft
r_{30}	mean droplet radius, ft
r	radial distance, ft
T	stagnation temperature, °R
T_R	probe temperature reading
t	static temperature, °R, °K

U	droplet velocity, ft/sec
U_L	fuel jet velocity, ft/sec
u	axial velocity in mixing region, ft/sec
V	air velocity, ft/sec
v	radial velocity, ft/sec
W	diffuser width, ft
x	axial distance, ft
Y	distance normal to the flow, ft
Y_F	total flow height, ft
y	mass fraction
y_m	penetration distance - normal to flow, ft
z	compressibility factor
α	thermal diffusivity, ft^2/sec
β	Poisson's ratio
γ	specific heat ratio
δ	coefficient of thermal expansion, $1/^\circ\text{R}$
ϵ	radiative emissivity
ζ	factor defined by Equation (229)
η	pressure recovery
θ	angle, deg
μ	viscosity coefficient, $\text{lbm-ft}^2/\text{sec}$
$\nu_{i,r}$	stoichiometric coefficient, i^{th} specie in r^{th} reaction
π	pressure ratio

- ρ density, lbm/ft^3
 σ surface tension (lbm/sec^2), Stephan Boltzmann constant,
 $\text{BTU/sec, } (^{\circ}\text{R})^4$
 τ time, sec
 ϕ defined by Equation (77)
 ψ defined by Equation (79)

Subscripts

- a air
 af adiabatic flame
 B burner
 c compressor
 e surface
 f fuel
 g coolant
 H heat-up
 i initial
 j incremental
 L liquid
 M maximum
 m mean or mixture
 S saturation
 V vaporization
 w wall

- 2 compressor rotor discharge station
- 3 burner inlet station
- 4 turbine inlet station
- α location upstream of dump diffuser
- β location downstream of dump diffuser

Superscripts

- * critical
- " conditions of the fuel-air streamtube
- averaged

I. INTRODUCTION

There are several current trends in modern gas turbine design, particularly in the small power range, that are creating difficulties for the combustion chamber designer. For instance, the trend toward higher cycle temperatures not only increases the required overall equivalence ratio for the burner but also increases the specific power of the machine. The resulting smaller dimensions of the rotating parts tend to make the combustion chamber dominate the engine packaging envelope when the conventional recirculating concept is used. In addition, the increased cycle temperature requires an increased cycle pressure to lower the specific fuel consumption. The foregoing considerations combined with the power requirements for Army applications constrain this engine configuration to include a centrifugal-type compressor. The outlet flow from such a compressor wheel has very high velocity; at the pressure ratios under consideration (10 to 12), the flow is supersonic. Thus the diffusing stator in this application is an extremely critical element, in particular since diffuser performance drops off drastically at higher Mach numbers.

One way to improve performance is to consider the diffuser and combustor as a system and to trade off reduced diffusion in the stator for increased burner inlet airspeed. However, the efficiency of the conventional recirculating primary-type burner is unacceptably low at airspeeds much above 200 ft/sec, so that a fundamental change in burner design philosophy is required for such a system.

The purpose of the present investigation is to utilize the philosophy and some of the computational technology developed for SCRAMJET (Supersonic-Combustion-Ram-Jet) engines to design this new type of turbo-engine burner. Accordingly, a GASL computer program, which analyzes flows with finite-rate combustion of hydrocarbon-type fuels plus turbulent mixing, was utilized to determine the design layout. No particular engine was specified, since this work was of fundamental nature; indeed, one of the tasks of the program was to determine the inlet conditions for best performance. However, some guiding parameters were set initially by the Army on mass flow range, pressure ratio, turbine inlet temperature, and overall size, so that the results would be applicable to their future engine needs. These engine parameters are listed in Table I.

TABLE I. ENGINE PARAMETERS		
	Sea Level Military Rated Power	Sea Level Idle*
Engine Airflow Rate, lb/sec	5.00	2.96
Compressor Pressure Ratio	12.5:1	5.08:1
Compressor Adiabatic Efficiency, %	80	78
Turbine Inlet Temperature, °F	2500	1587
Maximum Fuel Inlet Temperature, °F	300	300
Absolute Altitude Limit, 25,000 ft		
Ram Pressure Ratio = 1.0		
* 20% Power		

Although it was realized that the burner had to perform efficiently over the entire performance spectrum indicated in Table I, it was decided that the sea level 100 percent power condition would be most important. This case was called the design point, and all the major design calculations were performed at this condition.

The report is divided into sections as follows: Section II gives the analysis which determined the optimum burner inlet Mach number at the design point and thus fixed the inlet and exit flow areas. The performance variation is then computed over a range of power settings both at sea level and at altitude. Section III describes the burner design, which includes fuel injection, ignition, and the finite rate chemical reaction system. Section IV points out salient features of the experimental facility, while Section V presents and discusses the experimental results. Conclusions and recommendations are given in Section VI.

II. BURNER INLET CONDITIONS

In order to determine the optimum burner-inlet Mach number, the type and performance of the burner and also of the diffuser must be known. In this section, the performance of three candidate burner configurations is reviewed on the basis of one-dimensional, equilibrium flow. A dump-diffusion process is chosen for the diffusion model, and the overall diffuser-combustor performance is computed over a range of inlet Mach numbers. The optimum burner inlet Mach number is then defined when the overall pressure loss is minimum.

Before showing these analyses, definition of the off-design turbomachine flow is given so that physical flow quantities can be associated with each power setting.

OFF-DESIGN

The following assumptions are used in defining the off-design flow conditions:

1. Compressor operating line is synthesized from the "back-bone" type correlation detailed in Reference 1.
2. Combined diffuser-burner stagnation pressure loss equals 0.81.
3. The flow is choked in the first turbine nozzle stage.
4. Turbine adiabatic efficiency (both gas generator and power) equals 0.85.
5. Complete expansion occurs in the power turbine.

Table II lists the mass flow, burner and turbine inlet stagnation temperatures, and diffuser inlet (rotor discharge) stagnation pressure over a range of output power settings.

TABLE II. OFF-DESIGN CONDITIONS

	Percent Power	Altitude	
		Sea Level	25,000 ft
Mass Flow, \dot{m} (lbm/sec)	20	2.96	1.20
	60	4.37	1.65
	100	5.00	2.0
Burner Inlet Temperature, T_3 ($^{\circ}\text{R}$)	20	970	795
	60	1120	930
	100	1190	990
Turbine Inlet Temperature, T_4 ($^{\circ}\text{R}$)	20	2046	1690
	60	2640	2150
	100	2960	2440
Diffuser Inlet Total Pressure, P_2 (psia)	20	94	35
	60	150	52
	100	190	70

These cases are studied in the following section on the estimation of combustor performance.

ESTIMATION OF COMBUSTOR PERFORMANCE

The performance of three burner models is examined in this section to determine the performance of each, i.e., pressure recovery and outlet to inlet area ratio in terms of the inlet air Mach number. The models chosen were constant pressure, constant Mach number, and constant area burning. Equilibrium chemistry was assumed along with quasi one-dimensional flow, and no account was made of the fuel addition processes.

Constant Pressure Combustor

Conditions at the end of burning are determined for a constant pressure burning process. The calculations are made assuming a constant molecular weight and values of $\gamma = 1.4$ at the start of burning and $\gamma = 1.3$ at the end of burning. Experience at GASL has shown that these assumptions give very good results for an equilibrium combustion process in

the range of fuel-air ratio of interest in the present application.

Constant pressure burning is defined by

$$p_3 = p_4 \quad (1)$$

and

$$V_3 = V_4 \quad (2)$$

where

p = static pressure
V = air velocity
subscript 3 = before burning
subscript 4 = after burning

From the second condition,

$$(V/a^*)_4 = (V/a^*)_3 \quad a^*_3/a^*_4 \quad (3)$$

where a^* is the critical speed and (V/a^*) is a function of Mach number given by

$$V/a^* = M \sqrt{\frac{\gamma + 1}{2(1 + \frac{\gamma - 1}{2} M^2)}} \quad (4)$$

where

M = Mach number
 γ = ratio of specific heat

Now

$$a^* = \sqrt{\gamma g R T^*} \quad (5)$$

and

$$T^* = \frac{2}{1 + \gamma} T \quad (6)$$

so that

$$a^* = \sqrt{\frac{2\gamma}{1 + \gamma} g R T} \quad (7)$$

where

T^* = critical temperature
T = total temperature
g = acceleration of gravity
R = gas constant = 1544/MW

Hence, Equation (3) may be written

$$(V/a^*)_4 = (V/a^*)_3 \cdot \frac{\gamma_3(1+\gamma_4)T_3}{\gamma_4(1+\gamma_3)T_4} \quad (8)$$

For given values of T_4 and T_3 , this equation gives the variation of M_3 with M_4 as shown in Figure 1. Since the ratio T_3/T_4 is more or less independent of altitude, all of the present results (except the amount of heat added) are only functions of power setting.

Equations (2) and (3) applied to the continuity equation give

$$\frac{A_4}{A_3} = \frac{t_4}{t_3} \quad (9)$$

where

A = area
t = static temperature

This may be written

$$\frac{A_4}{A_3} = \frac{T_4}{T_3} \frac{(t/T)_4}{(t/T)_3} \quad (10)$$

where t/T is the Mach number function given by

$$t/T = 1 / (1 + \left[\frac{\gamma-1}{2} \right] M^2) \quad (11)$$

It is clear that with M_4 determined from Equation (8), Equation (10) gives the burner area ratios shown in Figure 2.

The burner recovery is defined by

$$\eta_B = \frac{P_4}{P_3}$$

where P is total pressure.

Since $p_4 = p_3$, this may be written

$$\eta_B = \frac{(p/P)_3}{(p/P)_4} \quad (12)$$

where p/P is the Mach number function given by

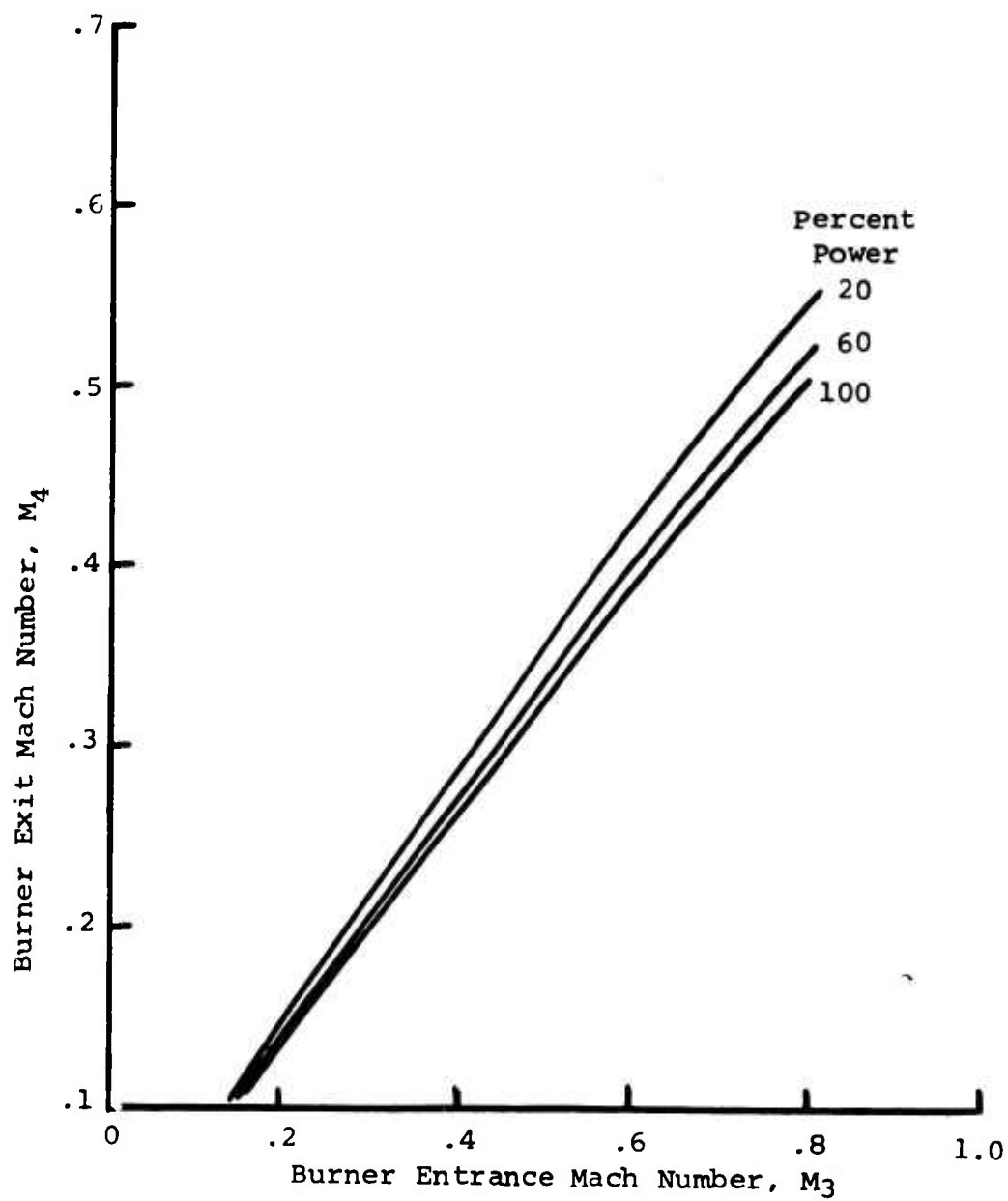


Figure 1. Burner Exit Mach Number - Constant Pressure Burning.

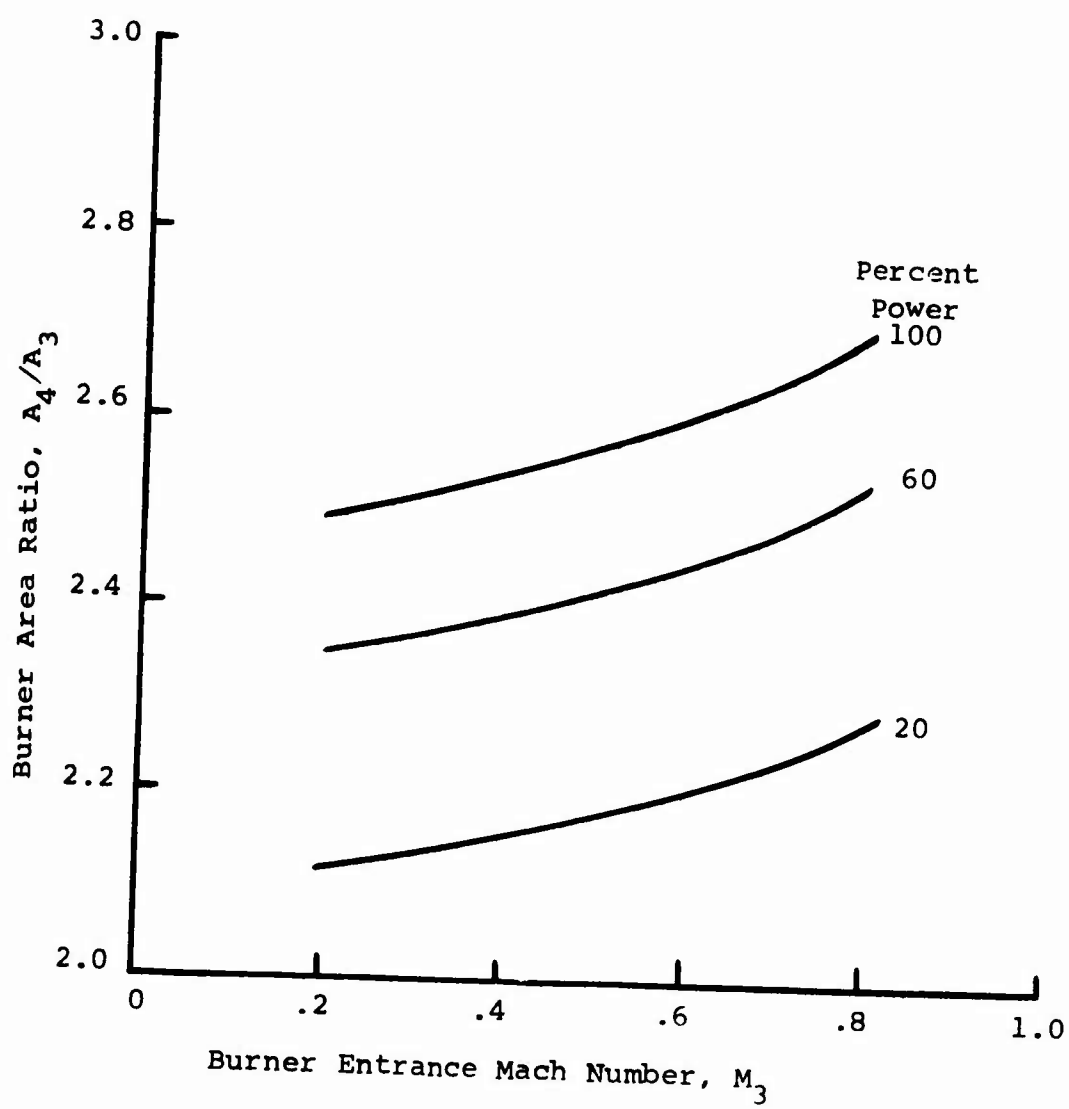


Figure 2. Burner Area Ratio - Constant Pressure Burning.

$$p/P = \left(\frac{1}{1 + \frac{\gamma-1}{2} M^2} \right)^{-\frac{\gamma}{\gamma-1}} \quad (13)$$

With M_4 determined from Equation (8), Equation (12) gives the burner recoveries shown in Figure 3.

The determination of the curves of fuel-air ratio in Figure 4 was made using the data in Reference 3. These data are for the general hydrocarbon C_nH_{2n} , but the results apply to JP-4 as well.

Constant Mach Number Burner

The constant Mach number burning process is treated by considering the general relationship between total pressure and total temperature, which for a one-dimensional process is expressed by

$$\frac{dp}{p} = - \frac{\gamma M^2}{2} \frac{dT}{T} \quad (14)$$

In the present application, M is constant but γ varies. However, since the change in γ is small, it is reasonable to treat γ as constant at an average $\bar{\gamma}$:

$$\bar{\gamma} = \frac{\gamma_3 + \gamma_4}{2} \quad (15)$$

Then Equation (14) gives

$$\eta_B = \left(\frac{T_3}{T_4} \right)^{\frac{\bar{\gamma} M_3^2}{2}} \quad (16)$$

The static pressure ratio across the burner is determined from

$$\frac{p_4}{p_3} = \eta_B \frac{(p/P)_4}{(p/P)_3} \quad (17)$$

(Note that although M_4 is equal to M_3 , $(p/P)_4$ is not equal to $(p/P)_3$ because of the difference between γ_4 and γ_3 .)

The temperature ratio and velocity ratio are given by the general relationships

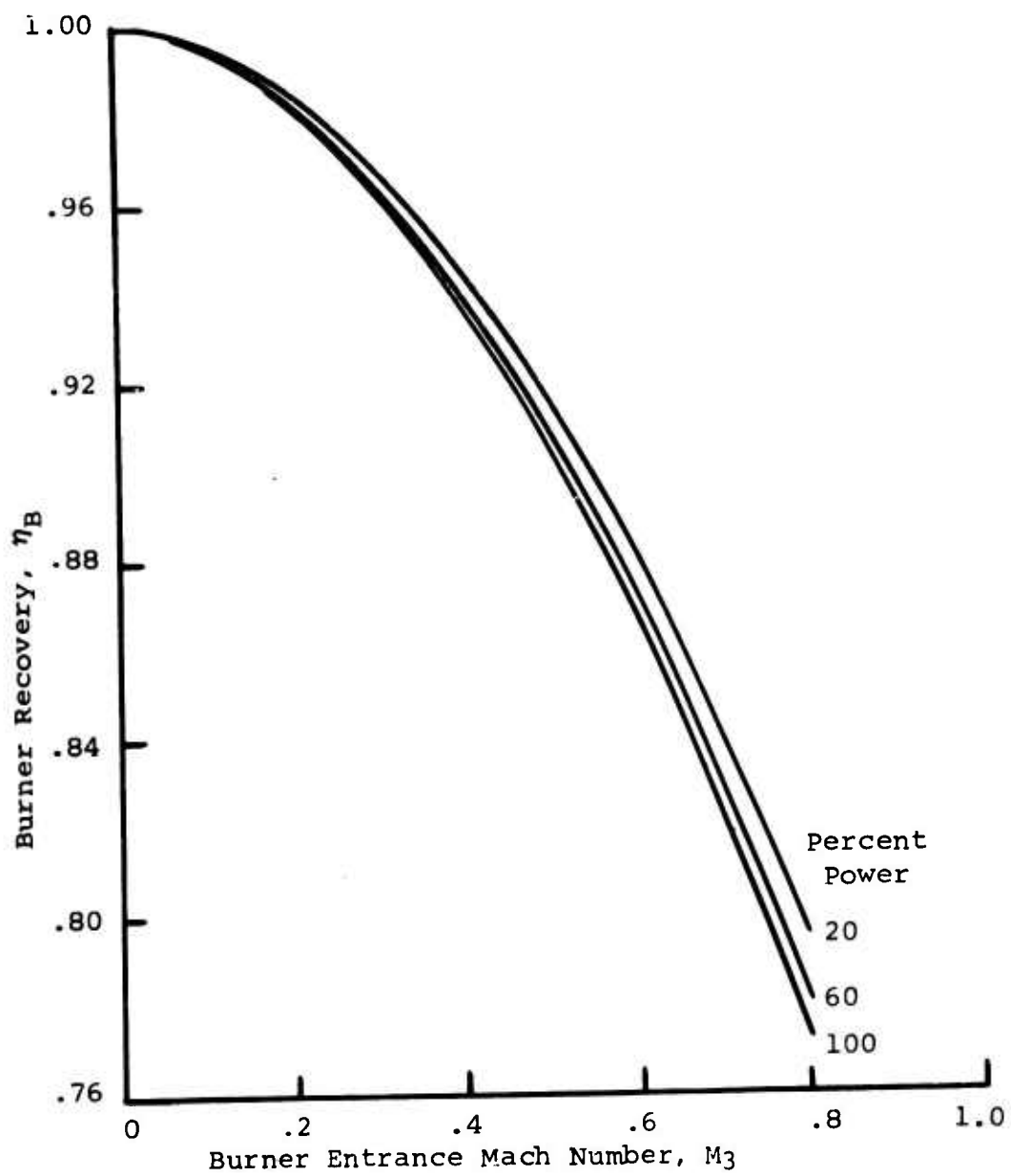


Figure 3. Burner Recovery - Constant Pressure Burning.

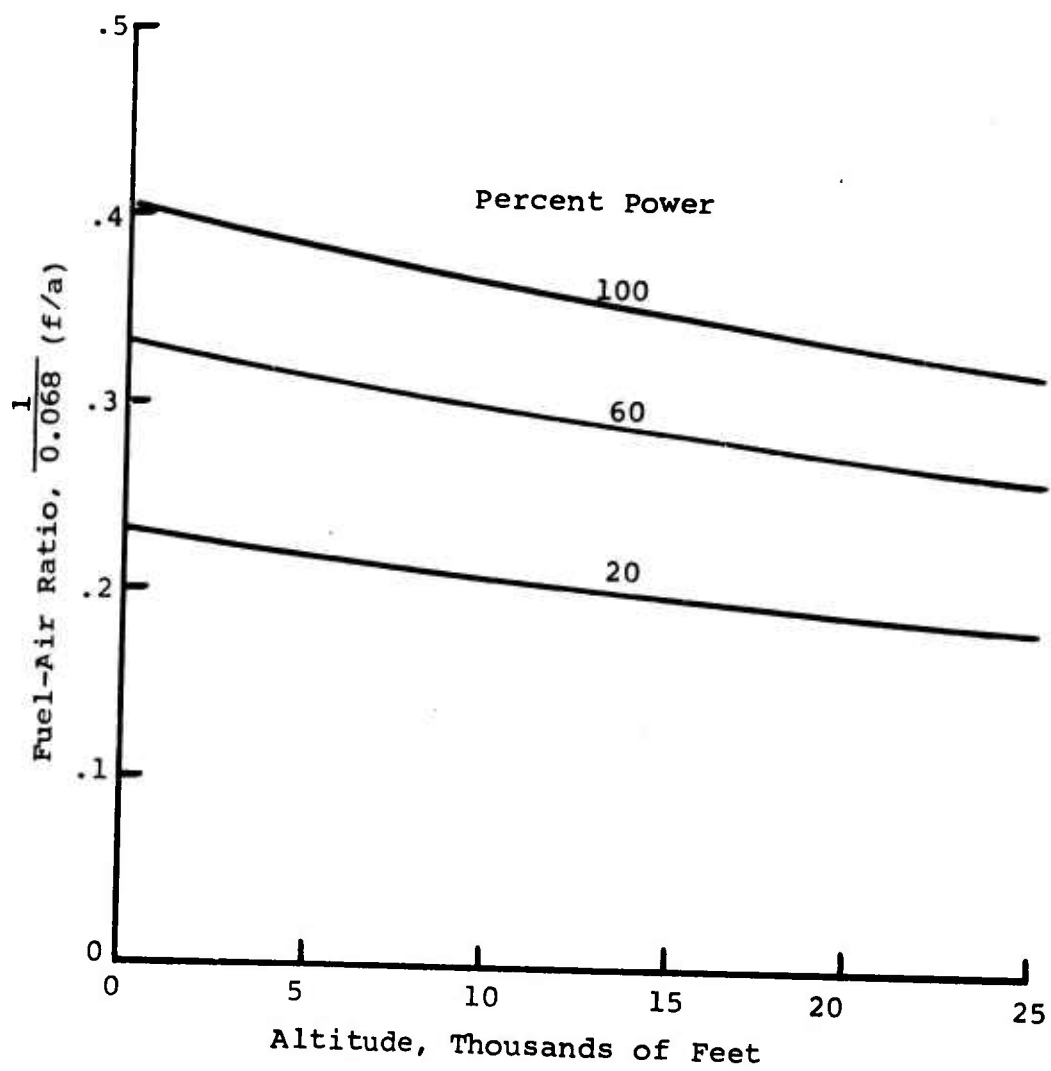


Figure 4. Fuel-Air Ratio vs Altitude at Various Power Levels.

$$\frac{t_4}{t_3} = \frac{(1 + (\frac{\gamma_3 - 1}{2}) M_3^2)}{(1 + (\frac{\gamma_4 - 1}{2}) M_4^2)} \left(\frac{T_4}{T_3} \right) \quad (18)$$

$$\frac{V_4}{V_3} = \frac{M_4}{M_3} \sqrt{\frac{\gamma_4}{\gamma_3} \frac{t_4}{t_3}} \quad (19)$$

The area ratio may then be found from

$$\frac{A_4}{A_3} = \left(\frac{p_3}{p_4} \right) \left(\frac{V_3}{V_4} \right) \left(\frac{t_4}{t_3} \right) \quad (20)$$

For the constant-Mach-number burning process, the results presented are the burner recovery (Figure 5), the area ratio (Figure 6), and the pressure ratio (Figure 7).

Constant-Area Combustor

The constant-area burning process is defined by the conservation of total momentum as

$$p_4 A + \frac{\dot{m}}{g} V_4 = p_3 A + \frac{\dot{m}}{g} V_3 \quad (21)$$

where

A = area

\dot{m} = mass flow

g = acceleration of gravity

From the continuity conditions,

$$pA = \frac{\dot{m}Rt}{V} \quad (22)$$

and the molecular weight is assumed to be the same before and after burning.

Using Equation (22) in Equation (21),

$$\frac{\dot{m}Rt_4}{V_4} + \frac{\dot{m}}{g} V_4 = \frac{\dot{m}Rt_3}{V_3} + \frac{\dot{m}}{g} V_3 \quad (23)$$

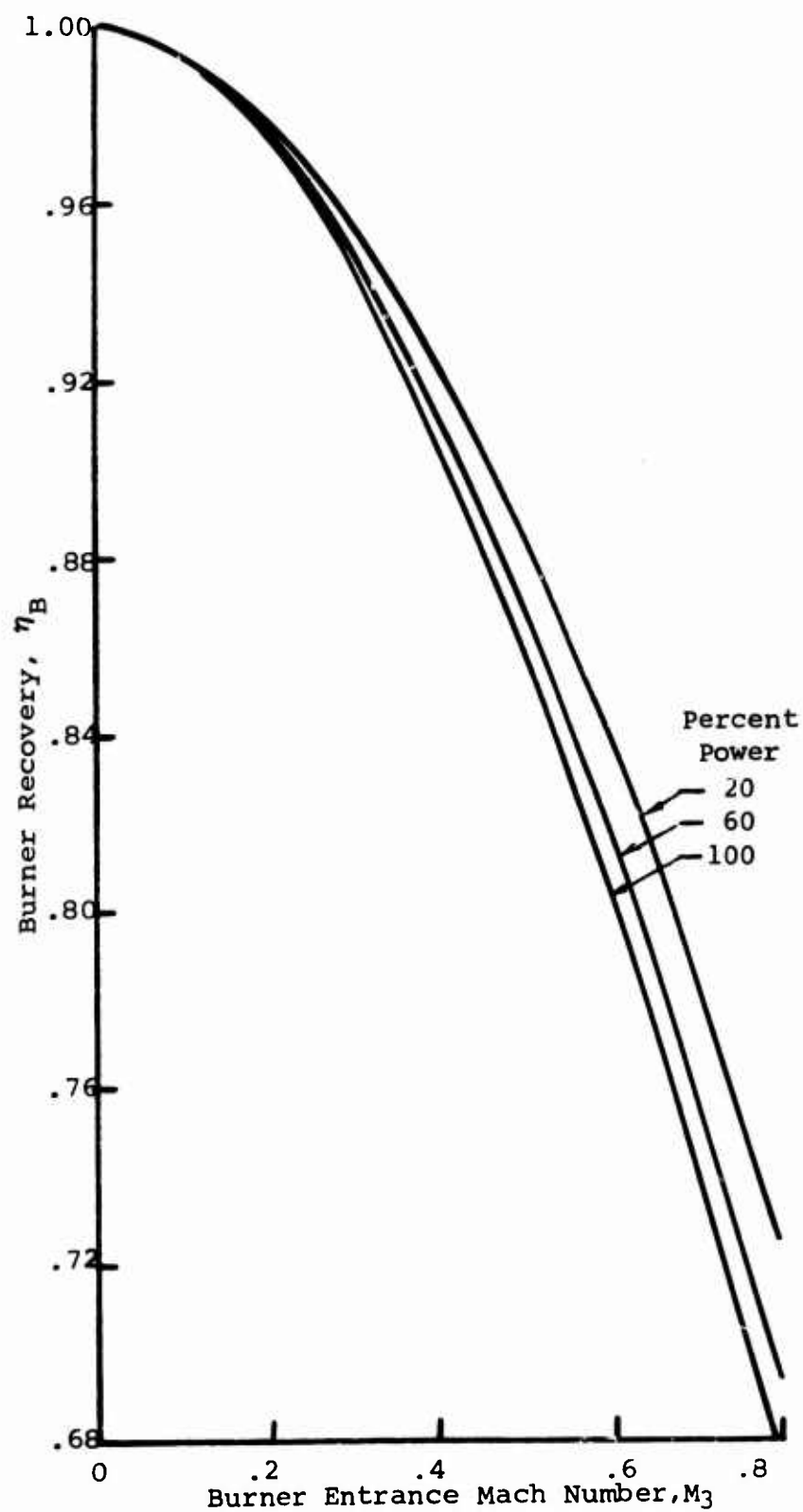


Figure 5. Burner Recovery - Constant-Mach-Number Burning.

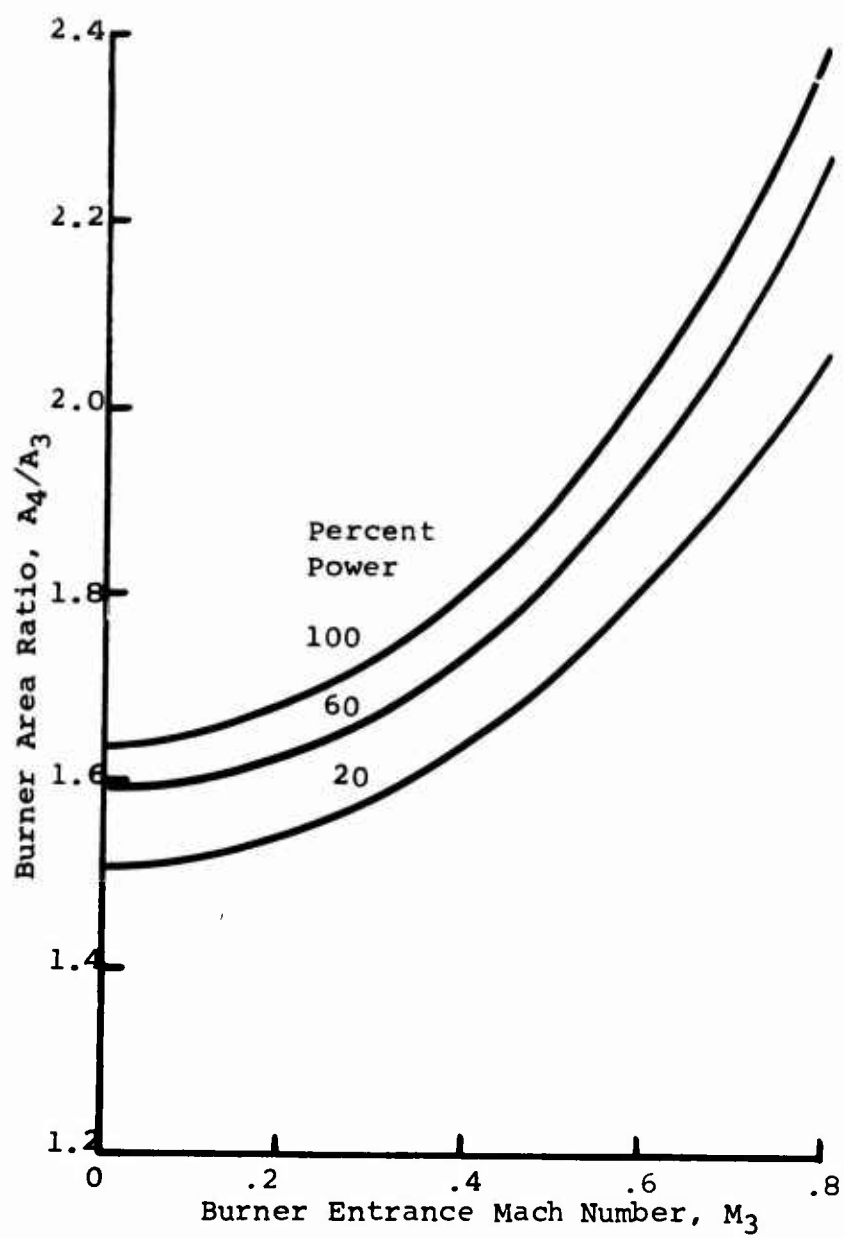


Figure 6. Burner Area Ratio - Constant-Mach-Number Burning.

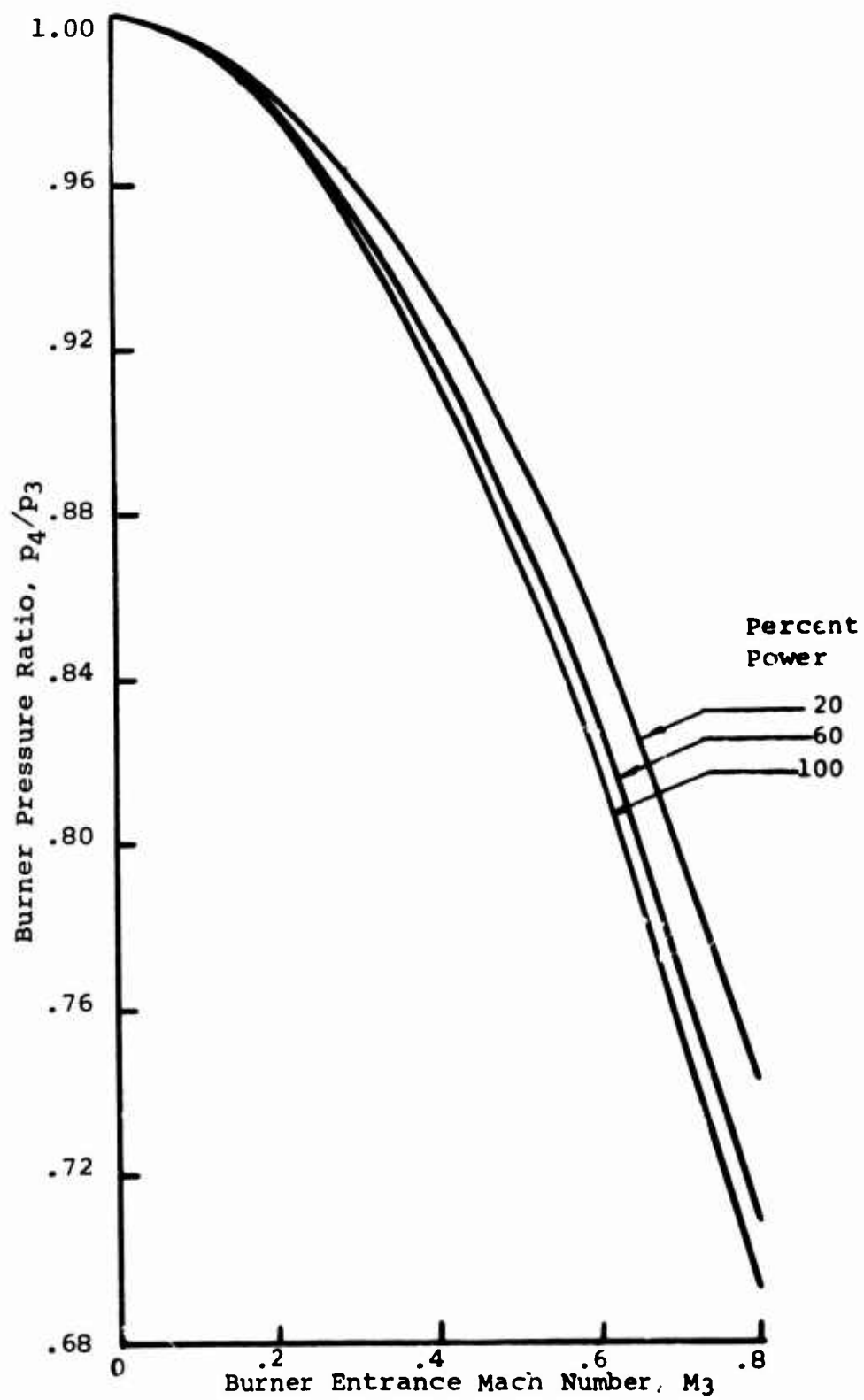


Figure 7. Burner Pressure Ratio - Constant-Mach-Number Burning.

or

$$V_4 \left(\frac{gRt_4}{V_4^2} + 1 \right) = V_3 \left(\frac{gRt_3}{V_3^2} + 1 \right) \quad (24)$$

Using Equation (11), the velocity is written

$$V = \frac{M}{\sqrt{1 + \frac{\gamma-1}{2} M^2}} \sqrt{\gamma g R t} \quad (25)$$

From the definition of Mach number,

$$\frac{gRt}{V^2} = \frac{1}{\gamma M^2} \quad (26)$$

and Equations (24) and (25), the equation defining constant-area burning is written

$$F_4 = F_3 \sqrt{\frac{\gamma_3 T_4}{\gamma_4 T_3}} \quad (27)$$

where

$$F = \frac{\sqrt{(1 + \frac{\gamma-1}{2} M^2) M^2}}{1 + \gamma M^2} \quad (28)$$

It is apparent that with M_3 , T_3 and T_4 known, Equation (27) gives M_4 .

With M_4 determined, the pressure after burning is found from the condition of conservation of total momentum, which is now written

$$p_4 A_4 (1 + \gamma_4 M_4^2) = p_3 A_3 (1 + \gamma_3 M_3^2) \quad (29)$$

or

$$\frac{p_4}{p_3} = \frac{1 + \gamma_3 M_3^2}{1 + \gamma_4 M_4^2} \quad (30)$$

The burner recovery (ratio of total pressure after and before burning) is determined from

$$\eta_B = \frac{\left(\frac{p}{P}\right)_3}{\left(\frac{p}{P}\right)_4} \left(\frac{p_4}{p_3}\right) \quad (31)$$

where (p/P) is the Mach number function, Equation (13).

The results of calculations for the constant-area burning process are given as the burner recovery (Figure 8), the Mach number after burning (Figure 9), and the pressure ratio (Figure 10).

Comparison of the constant-Mach-number and constant-area burner with those for the constant-pressure burning indicates the superiority of the constant-pressure burning process; namely, the burner recovery is higher. A quantitative comparison of the burner recovery, at 100 percent power, is shown in Figure 11. The results also show that the higher performance requires a larger burner exit area and results in lower burner exit Mach number.

DIFFUSER - TURNING LOSS MODEL AND EVALUATION OF OPTIMUM BURNER ENTRANCE CONDITIONS

The optimum burner entrance conditions are defined when the pressure recovery from compressor outlet to turbine inlet is maximized. In order to calculate this, the efficiencies of each element included in the system must be determined. For the combustor, the pressure recovery has already been defined as a function of inlet (to the burner) Mach number in the constant-pressure burner. The associated loss picture for the diffuser model and turning duct, since we are considering a radial compressor, is now required.

This section describes such a model and its resulting pressure recovery. From the combination of burning and diffuser-turning pressure loss as a function of burner inlet Mach number, the optimum operating condition is determined.

Diffuser Model

There are two extreme examples of a diffuser model: first, it can be perfectly efficient so that the optimum burner

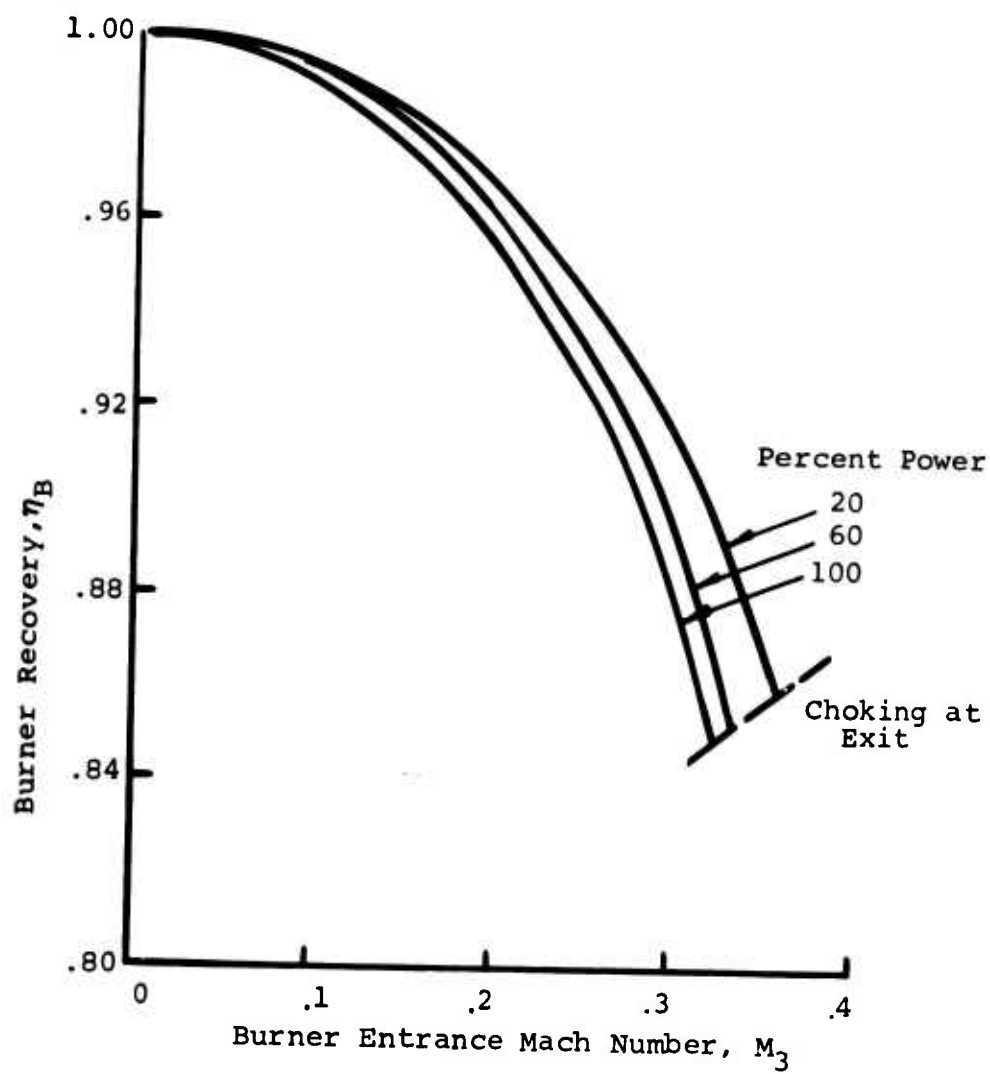


Figure 8. Burner Recovery - Constant Area Burning.

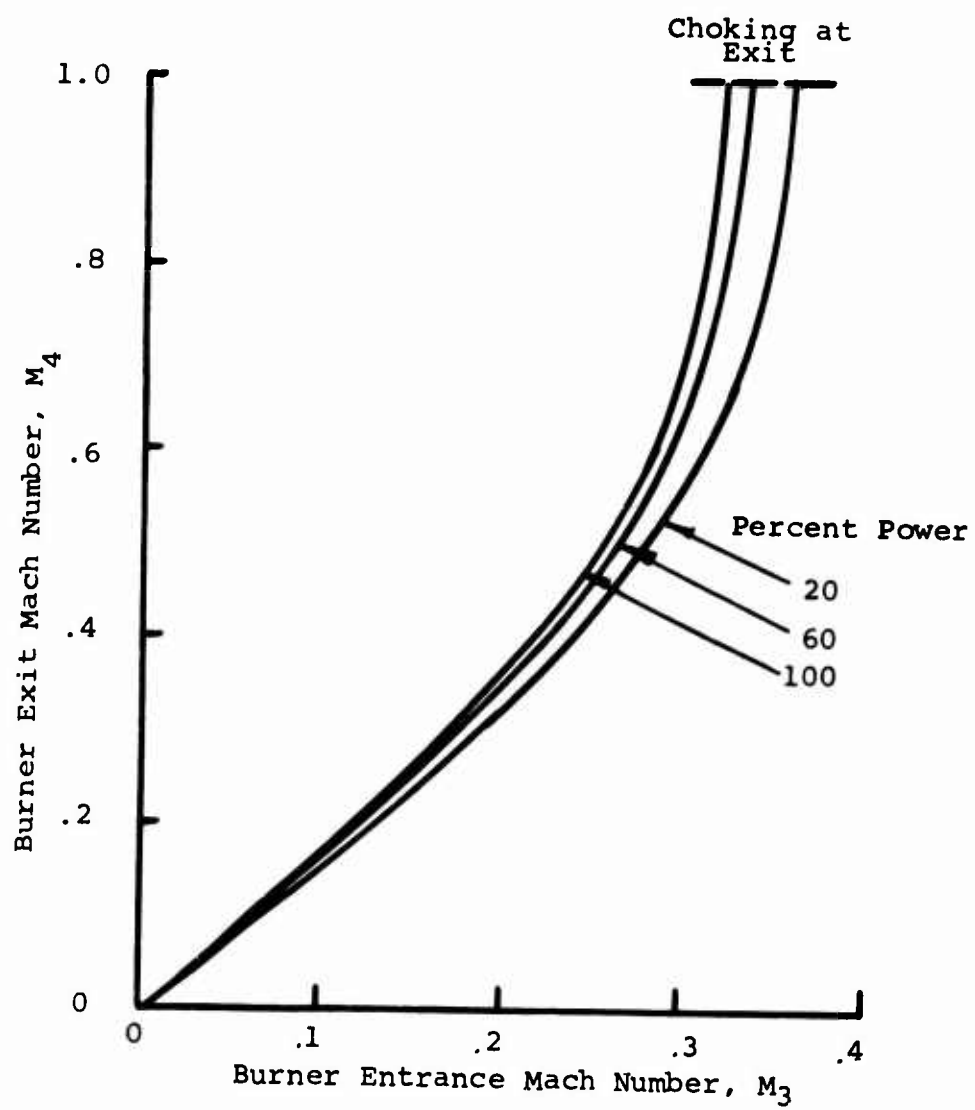


Figure 9. Burner Exit Mach Number - Constant-Area Burning.

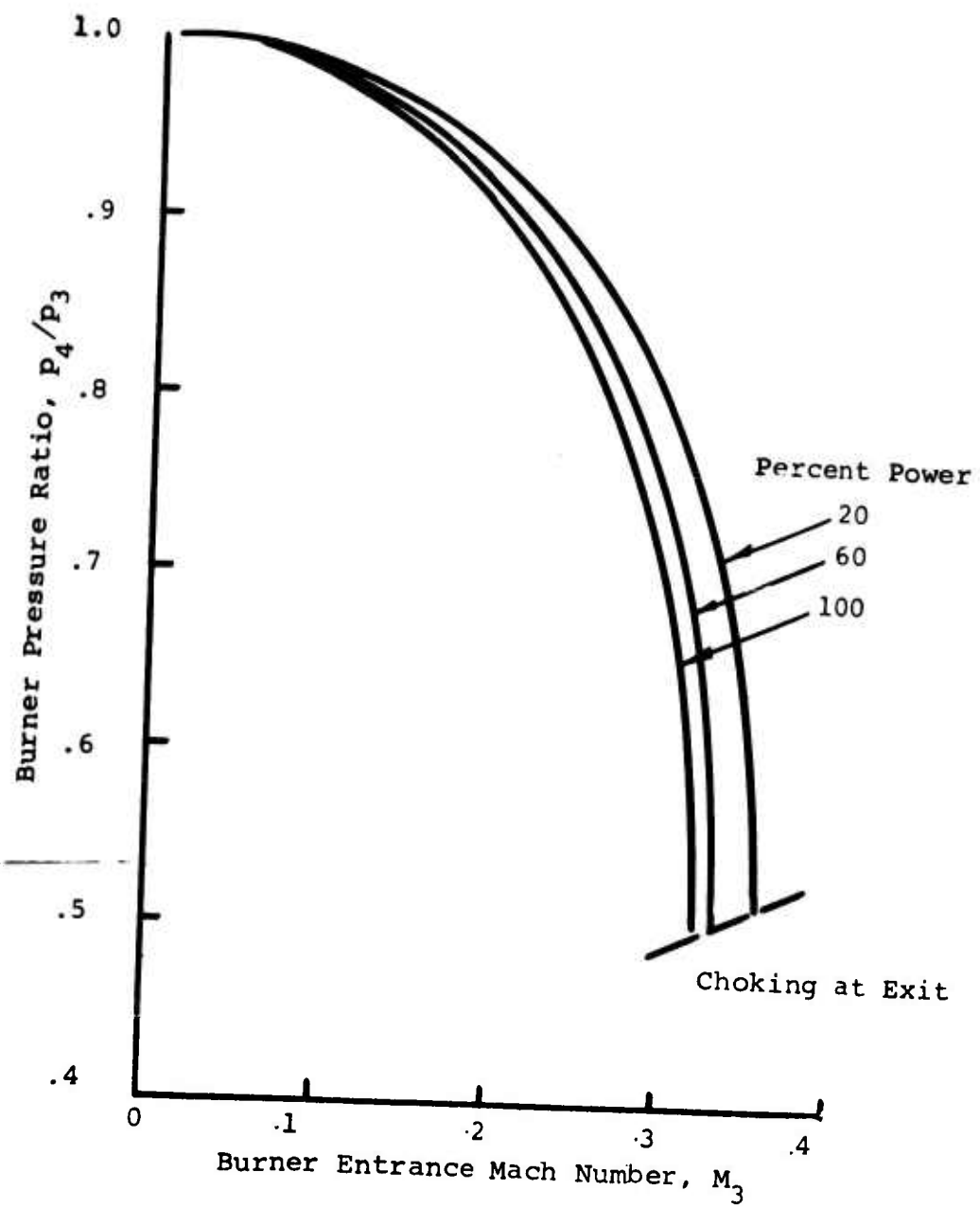


Figure 10. Burner Static Pressure Ratio - Constant-Area Burning.

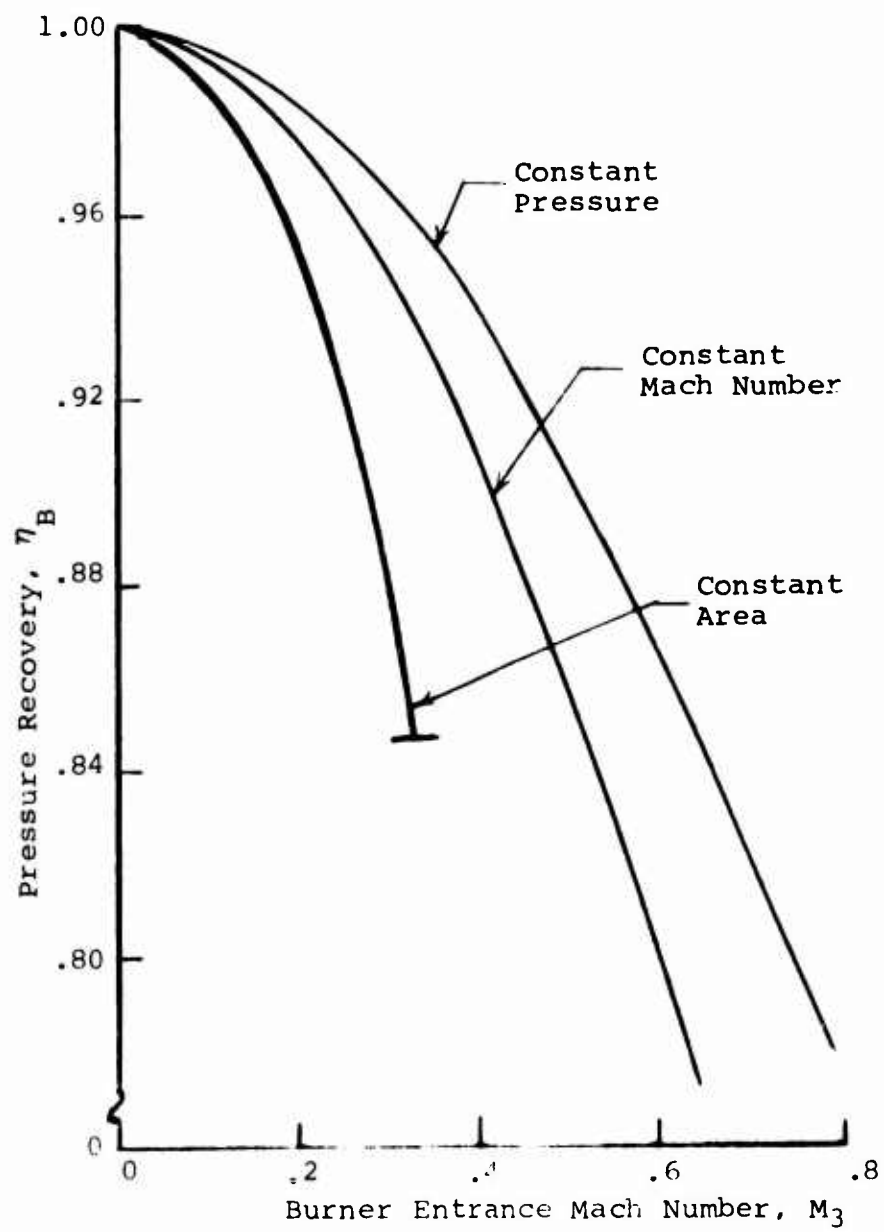
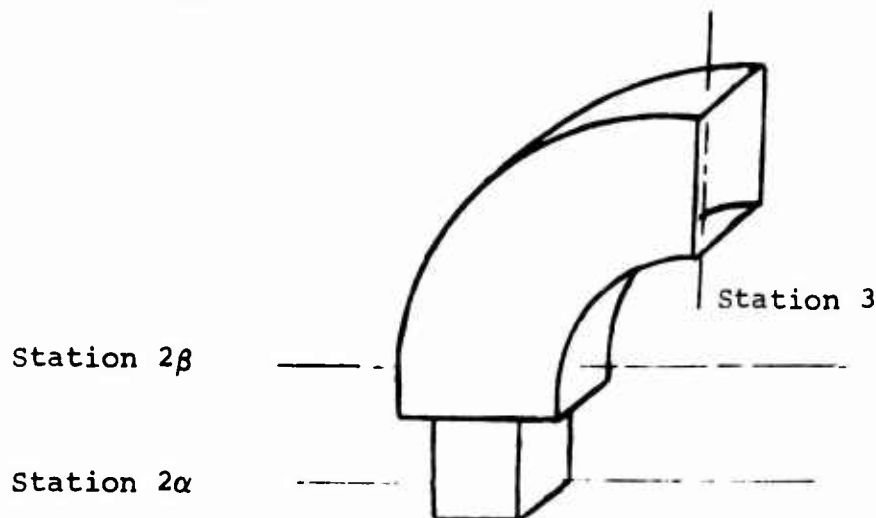


Figure 11. Comparison of Pressure Recovery Generated by Each Burner Model.

inlet Mach number is zero; or second, the diffuser can be completely inefficient (so that all the kinetic energy in the flow from the compressor is lost) and the optimum burner Mach number equals the compressor outlet value. Of course, the actual diffuser is neither of these, but the prediction of its performance is still one of the most difficult fluid dynamic problems yet to be resolved.

Nevertheless, in order to analyze a simple but representative diffuser system, the following items are considered: (1) the Army's requirement of low weight and volume; (2) the fact that separated flow exists in most diffusers; and (3) any simple model should be length or angle independent. These items lead one to choose a dump-diffuser as shown schematically in the sketch below:



Rectangular Diffuser and Elbow

Rectangular piping is indicated because it is representative of a centrifugal compressor application.

To define conditions at station (2α) (i.e., just upstream of the dump diffuser), we must describe the process whereby the supersonic outflow from the compressor is diffused below Mach 1. The most efficient actual diffusion is to assume that the flow experiences a normal shock. This would correspond to a long pipe frictional type diffuser. From the normal shock relations, c_f , Reference 4, for $M_2 = 1.27$, we find $M_{2α} = 0.8$ and $P_{2α}/P_2 = 0.987$. From dump loss data shown in Reference 5, conditions at station (2β) are defined. The turning losses are determined by using the data shown in

Reference 6 and assuming no area change in the turning duct. Thus, the conditions at the burner inlet are defined.

Analysis

To find the dump-diffusion pressure loss from Reference 5,

$$\frac{P_{2\beta} - P_{2\alpha}}{q_{2\alpha}} = z \left[\frac{A_R - 1}{A_R} \right]^2 \quad (32)$$

where

$$q = \frac{1}{2} \gamma M^2 p, \text{ the dynamic head} \quad (33)$$

$$A_R = A_{2\beta} / A_{2\alpha}, \text{ the area ratio} \quad (34)$$

and z is a compressibility factor.

Equation (32) can be rewritten, substituting Equations (33) and (13) as

$$\frac{P_{2\beta}}{P_{2\alpha}} = 1 - \frac{\gamma}{2} M_{2\alpha}^2 \left[1 + \left(\frac{\gamma-1}{2} \right) M_{2\alpha}^2 \right]^{-\frac{\gamma}{\gamma-1}} z \left[\frac{A_R - 1}{A_R} \right]^2 \quad (35)$$

and for $M_2 = 0.8$

$$\frac{P_{2\beta}}{P_{2\alpha}} = 1 - 0.304 z \left(\frac{A_R - 1}{A_R} \right)^2 \quad (36)$$

The value of z for a rectangular diffuser at this Mach number (0.8) is 2.6.

To find the Mach number after the dump (at station (2β)), we note, since the stagnation temperature of the air is constant, that

$$M_{2\beta} = M_{2\alpha} \left(\frac{P_{2\alpha}}{P_{2\beta}} \right)^{\frac{1}{\gamma}} \left(\frac{1}{A_R} \right) \left[\frac{p/P}{\sqrt{(t/T)}} \right]_{2\alpha} \left[\frac{\sqrt{t/T}}{p/P} \right]_{2\beta} \quad (37)$$

where t/T and p/P are defined by the Mach number functions, Equations (11) and (13) respectively.

Comparison of the pressure recovery $P_{2\beta}/P_{2\alpha}$ for the dump diffuser with some diffuser experiments, Reference 7, is shown in Figure 12. The experimental data are for two length-to-width ratios (L/W) diffusing from Mach 1 to $M_{2\beta}$. These data show the rather typical increase and then decrease which is due to flow separation and skin friction. As L/W decreases toward 0 (a dump diffuser), it is seen that the experimental curves trend toward the dump value.

To determine the pressure loss in the turn, from Reference 6,

$$\frac{P_{2\beta} - P_3}{q_{2\beta}} = \zeta \quad (38)$$

or

$$\frac{P_3}{P_{2\beta}} = 1 - \zeta \frac{\gamma}{2} M_{2\beta}^2 \left[1 + \frac{\gamma-1}{2} M_{2\beta}^2 \right]^{-\frac{\gamma}{\gamma-1}} \quad (39)$$

For a rectangular duct whose inlet perimeter has a width twice its depth and a radius of curvature equal to the width, the value of $\zeta = 0.2$.

The pressure loss for the entire diffuser-combustor system is

$$\eta = \frac{P_4}{P_2} = \left(\frac{P_{2\alpha}}{P_2} \right) \left(\frac{P_{2\beta}}{P_{2\alpha}} \right) \left(\frac{P_3}{P_{2\beta}} \right) (\eta_B) \quad (40)$$

where η_B is the combustion chamber pressure loss shown in Figure 3 as a function of Mach number and power setting. By denoting M_3 as the design Mach number defined as the sea level 100-percent military power condition, the value of η_B is determined. A plot of Equation (40) as a function of burner inlet Mach number is shown in Figure 13, where it is seen that η first increases and then decreases with increasing M_3 . Therefore, the Mach number where η is maximum is the optimum burner inlet condition and is approximately 0.5.

The dotted portion of the curve shows the recovery when the

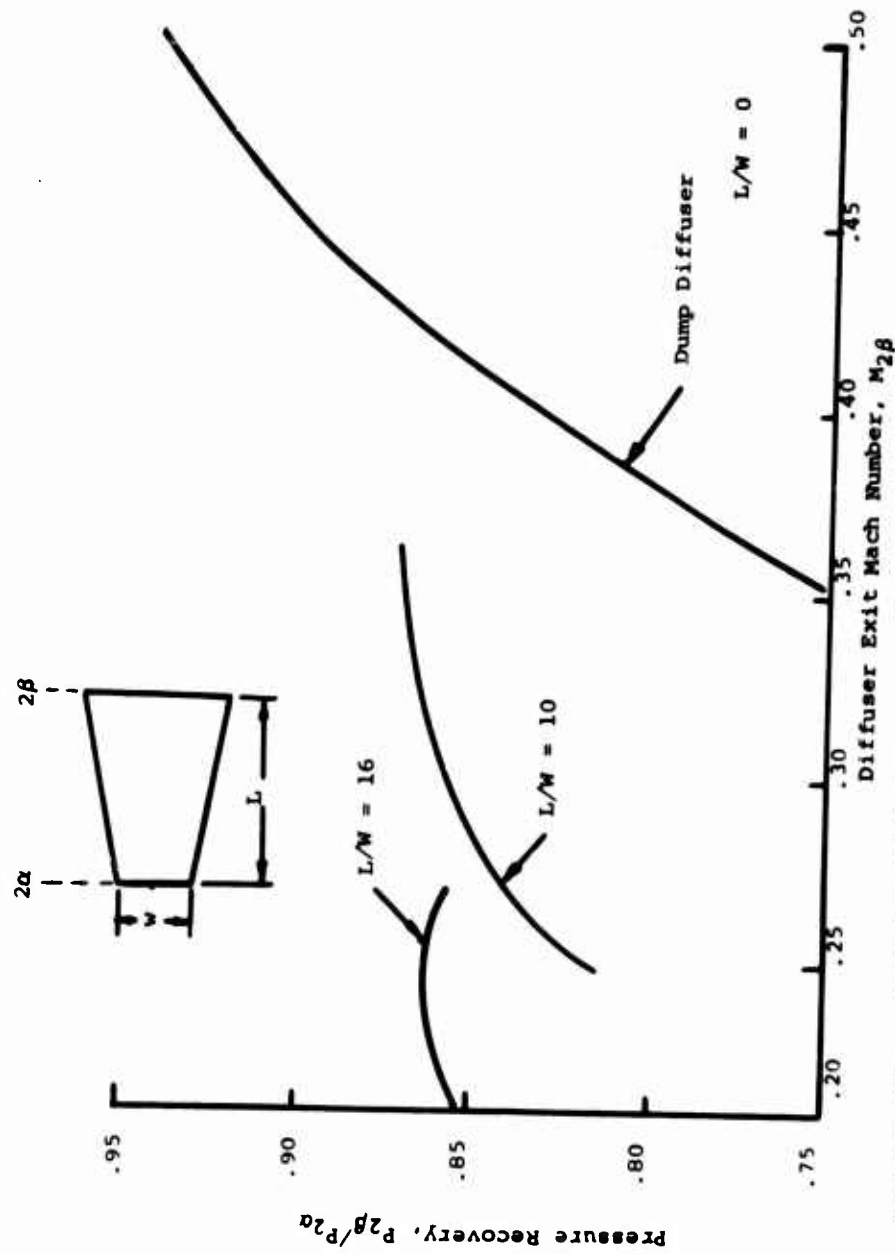


Figure 12. Diffuser Recovery - For an Expansion From $M_{2\alpha} = 0.8$ to $M_{2\beta}$

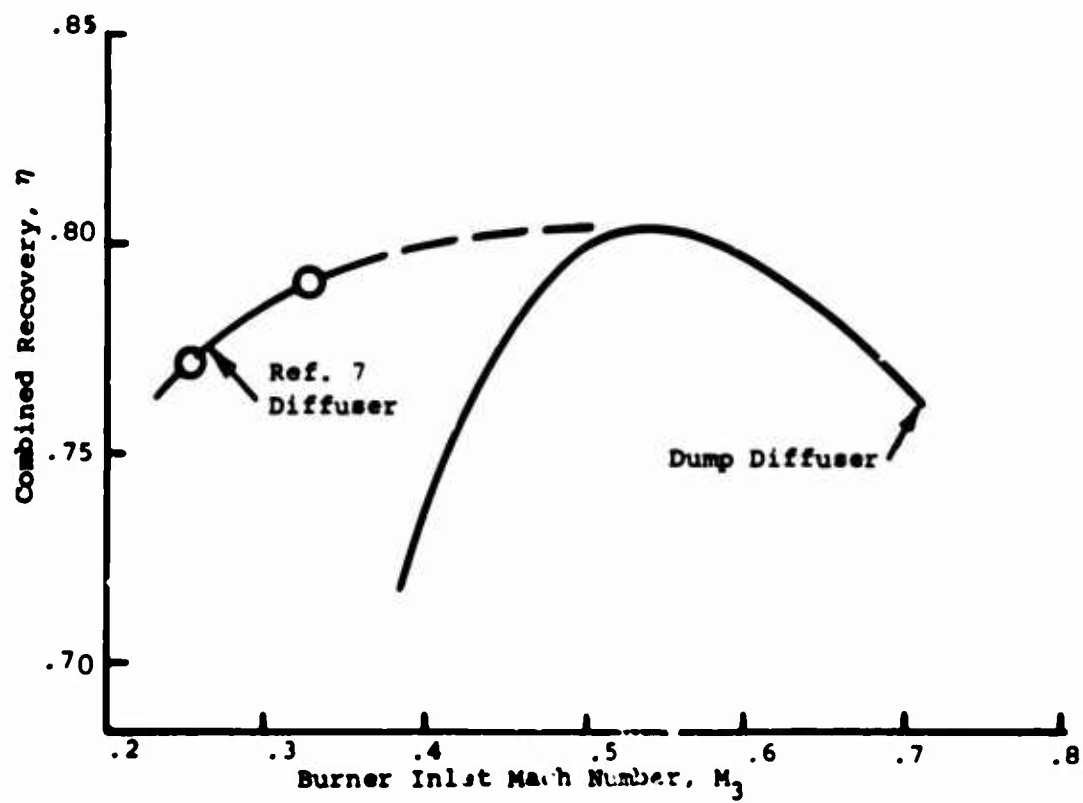


Figure 13. Combined Diffuser and Combustor Pressure Recovery vs Burner Inlet Mach Number.

experimental diffuser (Reference 7, $L/W = 10$) values are used instead of the dump diffuser values. The recovery of the system in this range of experimental data, although greater than with the dump diffuser, is still less than the maximum recovery with the dump. This means that if experimental data were available for this high value of M_{2g} , it would show that the optimum Mach number is between 0.53 and 0.33 (the better the diffuser, the lower the burner inlet Mach number). Therefore, it still appears reasonable to choose the design Mach number equal to 0.5.

METHOD OF COMPUTING BURNER OFF-DESIGN PERFORMANCE

The combustor loss curves are essentially design point values. That is, a given combustor inlet Mach number not only defines the burner outlet to inlet area ratio (A_4/A_3) but also specifies the combustor inlet conditions, i.e., area, velocity, static temperature, etc.

To determine the performance of the design Mach number combustor over the power spectrum, the following model for the off-design combustion process is postulated:

1. Burning occurs at constant pressures at all power settings. The associated burner recovery and requisite flow area ratio are thus defined.
2. Burning is initiated at the combustor inlet station.
3. Isentropic compression occurs from the end of burning to the actual exit station.

The reasons for choosing such a burning model are as follows:

1. It is fairly representative of the physical situation in the combustor.
2. Pressure losses can be defined easily.
3. Determined pressure loss is conservative.

To clarify this last point, if combustion would take place within the entire chamber, then the average Mach number at

which burning occurs would be less than the one in the present model. Since losses are directly proportional to Mach number, the burning losses are therefore less.

As the burner off-design mass flow and stagnation values have already been established, the off-design conditions, i.e., burner inlet Mach number and recovery, can be computed once the diffuser recovery and variation of compressor rotor outlet Mach number M_2 , with pressure ratio π_c , are known. Using the dump diffuser model and the variation of M_2 with π_c shown in Figure 14, the overall diffuser recovery is defined. The results are shown in Figure 15 in terms of burner entrance Mach number M_3 versus percentage of power. By using the assumed combustion model, the burner recovery is evaluated from Figure 5 at this value of M_3 and the percentage of power. The individual diffuser and burner recovery along with the combined recovery versus percentage of power are shown in Figure 16.

The altitude performance was determined in the same manner, with the assumption that M_2 versus π_c is invariant with altitude. When comparing sea level to altitude performance at the same value of π_c , there is found no variation in M_3 or η . However, there is some difference in M_3 on the basis of percentage of power as shown in Figure 15.

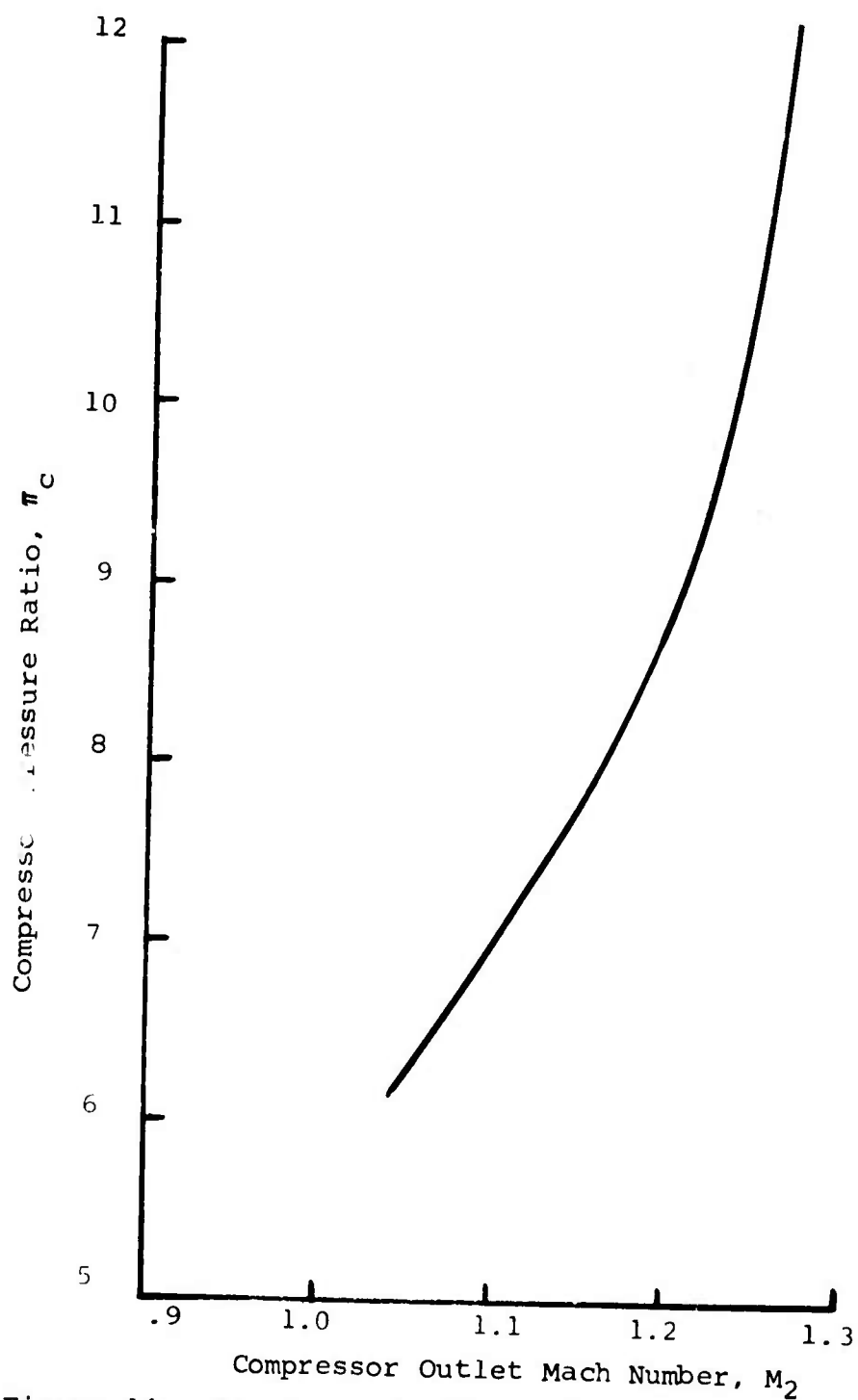


Figure 14. Compressor Rotor Outlet Mach Number vs Pressure Ratio.

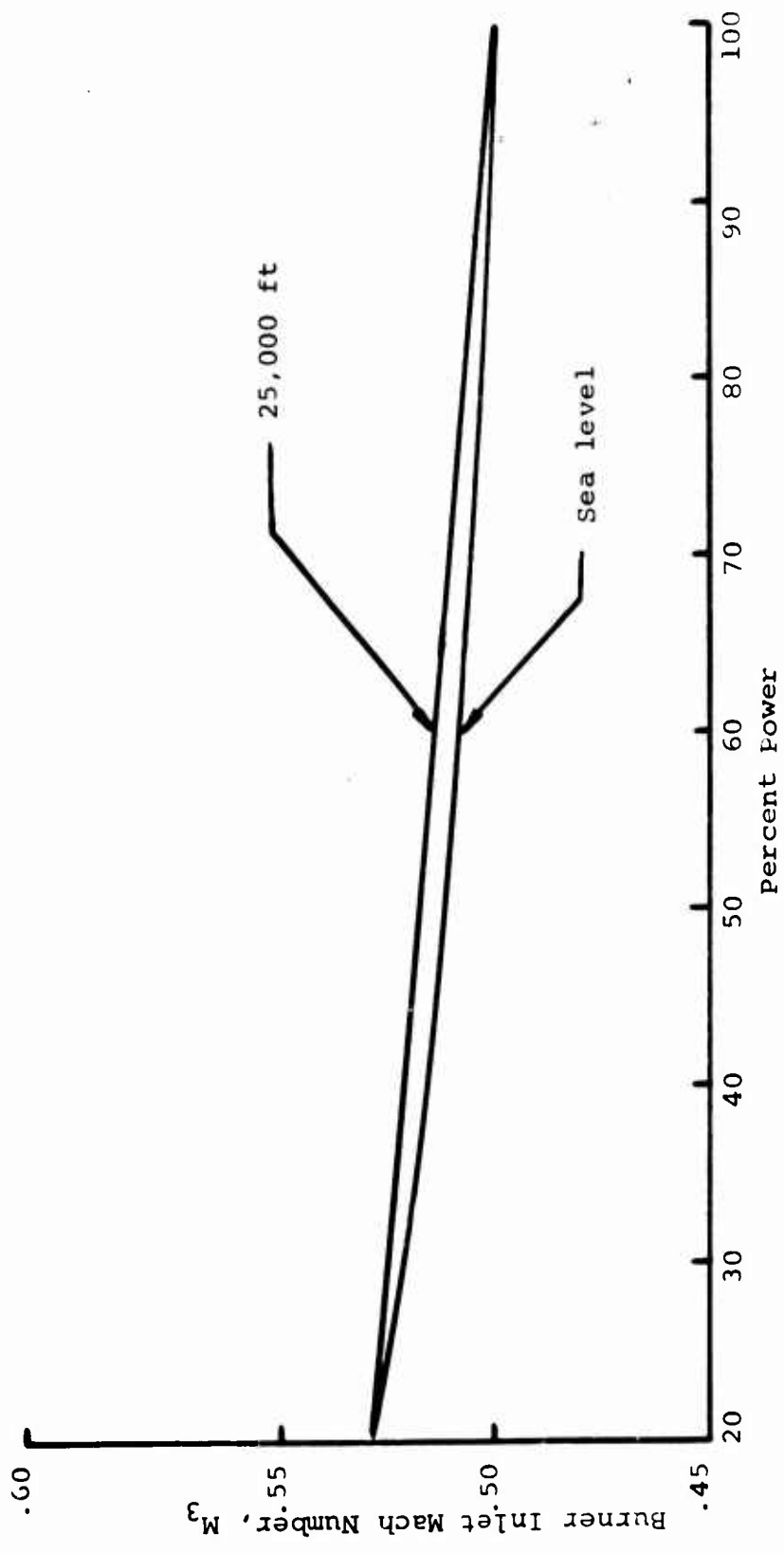


Figure 15. Burner Inlet Mach Number vs Percentage of Power, Mach Number = 0.5 at Maximum Power.

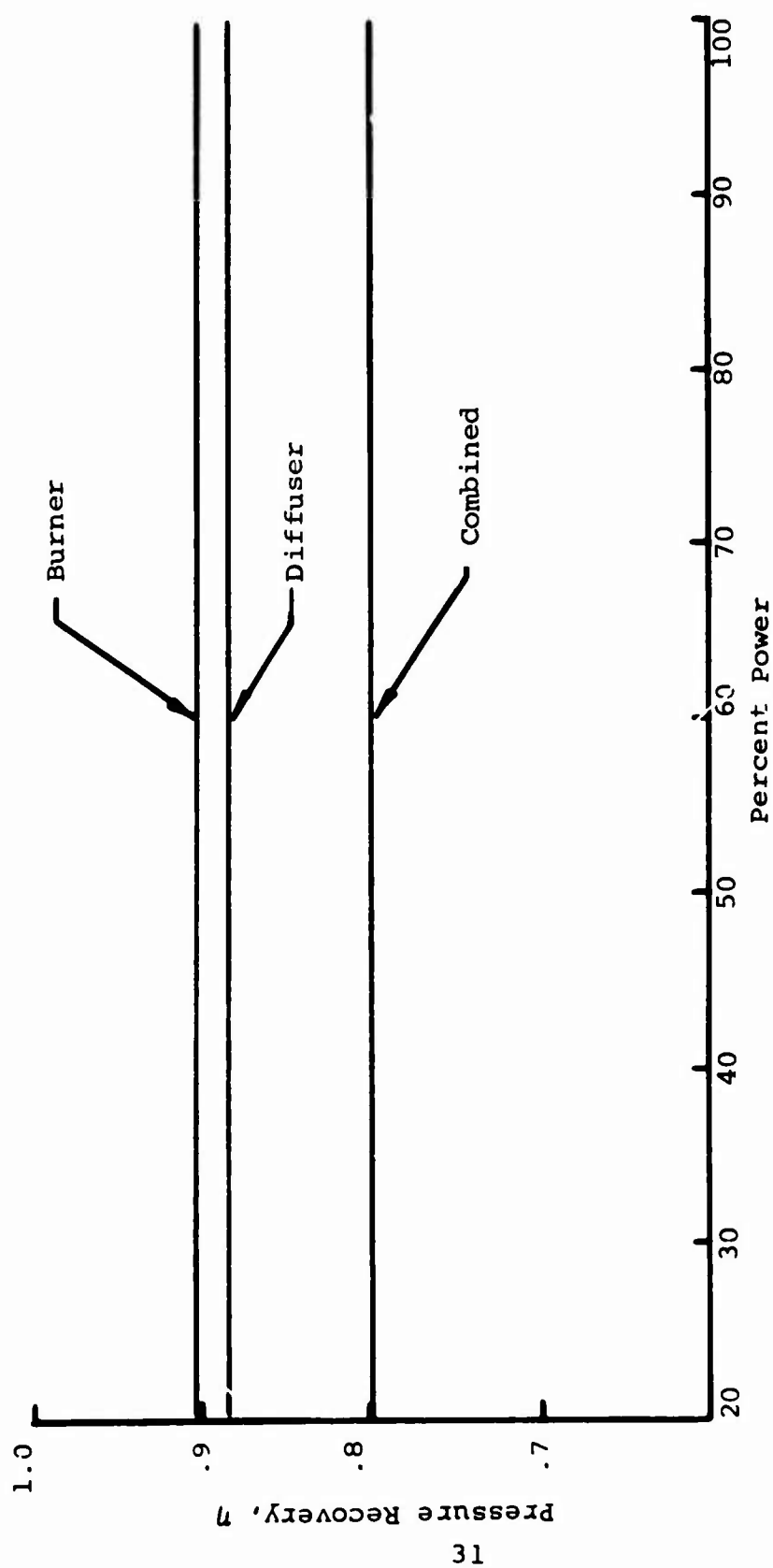


Figure 16. Diffuser, Burner, and Combined Recovery vs Percentage of power, Design Mach Number = 0.5.

III. BURNER DESIGN

This section describes first the basic concept of the high-speed burner in broad, general terms. The interrelations between fuel injection, mixing, burning, pressure, and flow area distributions are discussed so that the factors leading to the chosen configuration may be understood. After this, the three fundamental phenomena associated with combustion chambers, i.e., fuel injection, ignition, and combustion, are discussed in detail.

Only liquid JP-4 fuel was considered for the following reasons: first, to eliminate thermal decomposition and deposition problems accompanying fuel boilers; and second, in order that the high-speed burner concept not be vitiated by the consequence of specifying only a fuel in the vapor phase. As with most combustion chambers, the present design is complicated by the necessity of providing local fuel-air mixture ratios that are near stoichiometric. Whereas, in conventional designs, the incoming airflow is divided to form a primary combustor zone and then force-mixed by metering holes; in the new concept, stoichiometric zones are generated spatially by the proper injection of fuel. Creating the zone in this manner eliminates the enormous total pressure loss which accompanies the force-mixing of high-speed airflows. The method and analysis used to produce this fuel injection pattern, along with other problems such as liquid jet breakup and droplet heating and vaporization, are discussed under the heading Fuel Injection.

The combustion and mixing processes, besides propagating in the spatially varying concentration field, must also be constrained so as to occur at constant pressure.* In order to satisfy these combustion criteria, the GASL finite-rate combustion with turbulent mixing computer program was used to determine the requisite burner flow area distribution. A number of computer "experiments" were performed in the

* It will be recalled that constant pressure combustion was shown, in Section II, to be the most efficient of the three types of burning processes examined.

course of laying out a satisfactory burner configuration. These calculations and a brief description of the computer program are given under the heading Combustion. The calculations showed that mixing of the high-temperature-reacted products with the cold air proceeded very slowly and was the limiting process. This phenomenon necessitated that the characteristic mixing distance be the smallest dimension - the burner flow channel height. Thus the spatial variation was in the radial direction, with the flow considered to be uniform in the circumferential coordinate.

IGNITION

Imposing axial symmetry on the flow necessitates that the burner feature circumferential ignition. Therefore, the burner design included a combination of a circumferential slot flameholder and blunt-trailing-edge, spark-plug-driven strut-type igniters (called primary igniters). Fuel injected into the airflow from the side walls of each primary igniter is induced into the vortex region aft of the blunt trailing edge. It was supposed that flame established initially in the wake of these primary igniters would subsequently spread throughout the circumferential slot. In this way, the main fuel, arriving from an upstream injection station, is ignited. A schematic drawing of the fuel injection and ignition configuration is given in Figure 17. It can be noted in the figure that the main fuel addition is at station (F_1), the igniter fuel is at station (F_2), the primary igniter is at station (P), and the slot flame-holder is at station (S).

A review of the blunt-trailing-edge flameholder concept, given in Appendix I, shows that the experimental stability limits of this igniter can be correlated in terms of a so-called loading parameter

$$K(f/a) = \frac{V}{(p)^{.95} (D)^{.85}} \quad (41)$$

It is also shown in Appendix I that the slot flameholder stability data can also be correlated by the same expression. Therefore, both the slot depth and the trailing edge of the primary igniter are sized according to Equation (41).

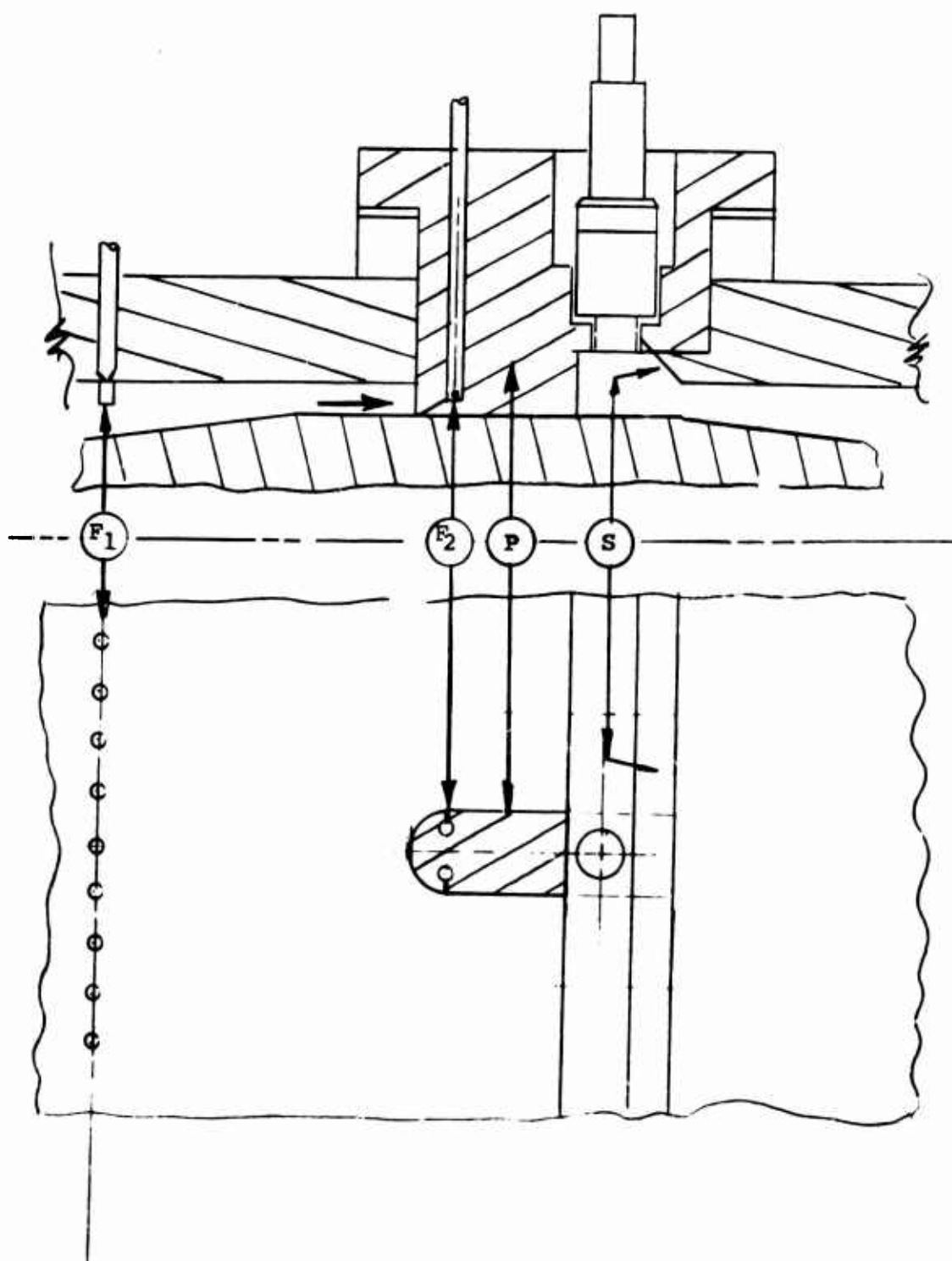


Figure 17. Ignition and Fuel Injection Systems

FUEL INJECTION

The problem at hand is to inject the main fuel into the burner in such fashion that by the time the fuel has reached the slot flameholder, it is vaporized and has the desired concentration level and distribution. These criteria form two distinct problems: the first requires knowledge of heating and vaporization rates of the fuel droplets so that the location of the main fuel injector relative to the slot can be fixed; the second requires the choice of the proper initial injection pattern and the knowledge of the mixing rates. Only normal injection is considered, primarily for ease of manufacture and installation.

In fixing the main fuel injector location, there are three distances which must be determined. These are (listed in order from the injection orifice):

1. liquid jet breakup length, x_b
2. length required to heat droplets to boiling temperature, x_H
3. length to vaporize droplets, x_v

The distance between injector station and slot is then taken as the sum of x_b , x_H , and x_v . In order to calculate items 2 and 3, the average droplet size and penetration distance, in addition to the forces on the droplets and their trajectories, are determined in a simple manner.

JET BREAKUP

When a liquid jet flows out of an orifice, it becomes unstable due to effects such as surface tension, and breaks up into small droplets. If the liquid is injected contracurrent or normal to a high-speed airstream, as is the case in the present burner, high shearing stresses are set up on the liquid surface and cause the jet to shatter. The distance to breakup is a function of these stresses, and as shown by the data compilation listed in Figure 2, Reference 8, the determining parameters are the Reynolds number and Weber number.

In the present case, the Reynolds number is

$$N_{Re} = \frac{\rho_L U_L d_o}{\mu_L} = 4750 \quad (42)$$

and the Weber number is

$$N_{We} = \frac{\rho_a V^2 d_o}{\sigma_L} = 8600 \quad (43)$$

where

U_L = the fuel jet velocity, 10 ft/sec

V = air velocity, 800 ft/sec

ρ_L = fuel density, 48 lbm/ft³

ρ_a = air density, 0.32 lbm/ft³

μ_L = fuel viscosity, $2.7 \cdot 10^{-4}$ lbm ft²/sec

σ_L = fuel-air surface tension, $4.65 \cdot 10^{-4}$ lbm/sec²

d_o = orifice diameter, $\frac{.032}{12}$ ft

so that from the aforementioned data compilation chart, this fuel jet corresponds to the regime called immediate jet breakup; thus, $x_b = 0$.

Penetration Distance and Droplet Size

The distance that the fuel penetrates into the airstream, along with the maximum and volumetric mean diameter of the resulting fuel droplet, can be computed with the above values of Reynolds and Weber numbers. Using the analysis of Ingebo in Reference 9, it is found that the penetration distance y_m equals

$$y_m = d_o (1.8) \left[\frac{N_{Re}}{N_{We}} \right]^{0.7} = 0.03 \text{ in.} \quad (44)$$

the maximum drop diameter is

$$D_M = d_o (22.3) \left[N_{Re} (N_{We}) \frac{V}{U_L} \right]^{-0.29} \\ = 5 \cdot 10^{-5} \text{ ft;} \quad (45)$$

and the volume-mean drop diameter is

$$D_{30} = d_o (3.9) \left[N_{Re} (N_{We}) \frac{V}{U_L} \right] \quad (46)$$

$$= 2.5 \cdot 10^{-5} \text{ ft}; r_{30} = 1.25 \cdot 10^{-5} \text{ ft}$$

Droplet Trajectory

The following simple analysis determines the distance necessary to accelerate the fuel droplets. It is assumed that the normal velocity components can be ignored (note the negligible penetration distance), that all droplets are the same size and that the properties of the oncoming air-flow are constant.

The force on the droplet is set equal to the drag on a sphere so that from Newton's law,

$$\frac{1}{2} \rho_a (V-U)^2 C_D \pi r_{30}^2 = \frac{4}{3} \pi r_{30}^2 \rho_L U \frac{dU}{dx} \quad (47)$$

where U is the droplet velocity, C_D is the drag coefficient, and x is the axial distance. The value of C_D is a function of the droplet Reynolds number, where this Reynolds number is defined as

$$N_{Re,D} = \frac{\rho_a (V-U) D_{30}}{\mu_a} \quad (48)$$

During the acceleration period, C_D varies (c.f., Reference 10) from 0.9 at U equal 0 to 6.0 at U equal $0.9V$. By integrating Equation (47) in a step-by-step fashion, assuming C_D constant at its average value during each x step, gives for the incremental distance x_j ,

$$x_j = \frac{1}{200 \overline{C_{Dj}}} \left\{ \log \left[\frac{V-U}{V-U_i} \right] + V \left[\frac{1}{V-U} - \frac{1}{V-U_i} \right] \right\} \quad (49)$$

where

- $\overline{C_{Dj}}$ = the average value of the drag coefficient in step j
- x_j = the incremental distance
- U_i = droplet velocity at the beginning of the step

At $U=0.9V$, the total distance traversed by the droplets is

$$x = \sum_j x_j = 0.18 \text{ in.} \quad (50)$$

It will be seen later that this distance is an order of magnitude less than the heat-up or vaporization distance, so that the droplet may be assumed to start impulsively at velocity $U = 800 \text{ fps}$.

HEAT-UP

To calculate the distance required to vaporize the fuel droplets, the heating processes are imagined to be separable into two distinct entities: a heat-up length and a subsequent vaporization length. To decouple these two phenomena, it is assumed that the thermal conductivity of the liquid is large. Therefore, to find the heat-up time and associated droplet travel distance, only the thermal boundary condition is solved, or

$$\frac{4}{3} \pi r_{30}^3 (\rho C_p)_L \frac{\partial T}{\partial \tau} = hA(T_3 - T_L) \quad (51)$$

thus ignoring the droplet's spatial temperature variation, $\partial T / \partial r$. This concept is not quite true during the latter part of the heat-up period, when the droplet surface has reached the boiling point (with attendant vaporization), since the droplet core is cooler because of the finite rate of heat conduction. The error introduced by this approximation is shown to be quite small and conservative.

In these calculations it is again assumed that the droplets are spherical and are all the same size, $r_{30} = 1.25 \cdot 10^{-5} \text{ ft}$. Also, the initial fuel temperature is $T_{Li} = 520^\circ\text{R}$; the ambient air temperature is $T_3 = 1200^\circ\text{R}$; the ambient pressure is 10 atmospheres; and the fuel's boiling point is taken as its initial saturation temperature at the ambient pressure, or $T_3 = 900^\circ\text{R}$.

Since it has been shown that the relative droplet velocity $(V-U)$ is small, the Stokes-flow result can be used to determine the heat transfer coefficient. In this flow regime, the Nusselt number is

$$N_{Nu} = \frac{hD_{30}}{k_a} = 2.0 \quad (52)$$

or

$$h = \frac{k_a}{r_{30}} \quad (53)$$

Substituting this value of h into Equation (51) gives

$$\frac{4}{3} \pi r_{30}^3 (\rho C_p)_L \frac{dT}{d\tau} = \frac{k_a}{r_{30}} 4\pi r_{30}^2 (T_3 - T_L) \quad (54)$$

and integrating gives

$$5.73 \cdot 10^3 \tau = \log \frac{T_3 - T_{Li}}{T_3 - T_L} \quad (55)$$

where the thermal conductivity of the air is taken as

$$k_a = 0.72 \cdot 10^{-5} \text{ BTU/sec, ft, } ^\circ\text{R}$$

The heat-up time is found by setting

$$T_L = T_S = 900^\circ\text{R}$$

or

$$\tau_H = \frac{0.8}{5.73 \cdot 10^3} = 1.45 \cdot 10^{-4} \text{ sec} \quad (56)$$

and during this time the fuel droplet travels a distance

$$x_H = V(\tau_H) = 807 (1.45 \cdot 10^{-4}) 12 = 1.4 \text{ in.} \quad (57)$$

To ascertain the error associated with the assumption of high thermal conductivity, the time for the surface temperature of a spherical droplet to reach 900°R was determined from the graphical solutions in Reference 11. With the aforementioned flow conditions, droplet size, etc., it is found that the time required for the droplet surface to reach 900°R is

$$\tau_H = 1.38 \cdot 10^{-4} \text{ sec}$$

Comparing this value to the approximate time, previously determined as $1.45 \cdot 10^{-4}$ seconds, reveals the difference to be negligibly small.

Vaporization

After the droplet has reached boiling temperature, further convective heating vaporizes the liquid, with the fluid temperature remaining constant. The rate at which a single droplet evaporates is

$$-\dot{m} \rho_L 4\pi r^2 \frac{dr}{d\tau} = h 4\pi r^2 (T_3 - T_S) \quad (58)$$

where \dot{m} is the heat of evaporation and equals 150 BTU/lb. Substituting the Stokes-flow relation for h gives the following vaporization time as a function of droplet size:

$$\tau_V = - \frac{\dot{m} L}{2k_a (T_3 - T_S)} \int_{r_{30}}^r d(r)^2 = 3 \cdot 10^{-4} \left(1 - \frac{r^2}{r_{30}^2}\right) \quad (59)$$

The time for complete vaporization, i.e., when $r = 0$, is by inspection:

$$\tau_V = 3 \cdot 10^{-4} \text{ sec} \quad (60)$$

and the vaporization distance is

$$x_V = V(\tau_V) = 2.4 \text{ in.} \quad (61)$$

The total distance traveled by the droplet during heat-up and vaporization is $x = x_h + x_V = 3.85$ inches; therefore, the main fuel injector is located 4.0 inches from the slot flameholder.

Mixing

The second part of the fuel injection problem is to obtain a specified fuel-air distribution in the vicinity of the slot flameholder. It was desired that the fuel-air ratio be maintained axisymmetric with a stoichiometric condition adjacent to the slot, zero f/a at the opposite wall; in addition the distribution should have a step-like variation. The analysis used to determine the mixing of the injected fuel with the oncoming airflow is shown in Appendix II.

By assuming that the fuel injectors act like point sources, the fuel-air ratio downstream of each orifice can be expressed as

$$f/a = \frac{\dot{m}_f}{4\pi M_a} \frac{V}{D_T x} \exp \left[-\frac{Vr^2}{4D_T x} \right] \quad (62)$$

No distinction was made between the liquid and vaporized fuel; however, the value of D_T/V was taken constant at 0.0004 ft and was thus more representative of the liquid. The axial location (x) was 4 inches - the distance computed for complete vaporization. As indicated in Appendix II, because of the linearity of the basic diffusion equation, the superposition principle allows the determination of the fuel concentration when there is more than one contributing injector. Finally, the effect of the bounding annulus walls is accounted for by the assumption of mirror-like fuel reflection. Thus, the fuel concentration at any point can be written as

$$f/a = \sum_i (f/a)_i \quad (63)$$

and expanding to include the effect of the bounding walls,

$$f/a = \sum_i \underset{\text{Direct}}{(f/a)_i} + \sum_i \underset{\text{Reflected}}{(f/a)_i} \quad (64)$$

The results of the fuel-air mixing computations are shown in Figure 18, which is a representative segment of the slot plane. The listed numerical values are the calculated fuel-air ratios and the phantom lines indicate the upstream main fuel injector configuration. (This injector design is discussed in detail in the next section.)

It is seen from the figure that the desired concentration features are grossly obtained with the chosen fuel injector configuration. This distribution could have been improved if another row of injector tubes had been inserted; however, the added complexity and drag of such a system decided against its inclusion.

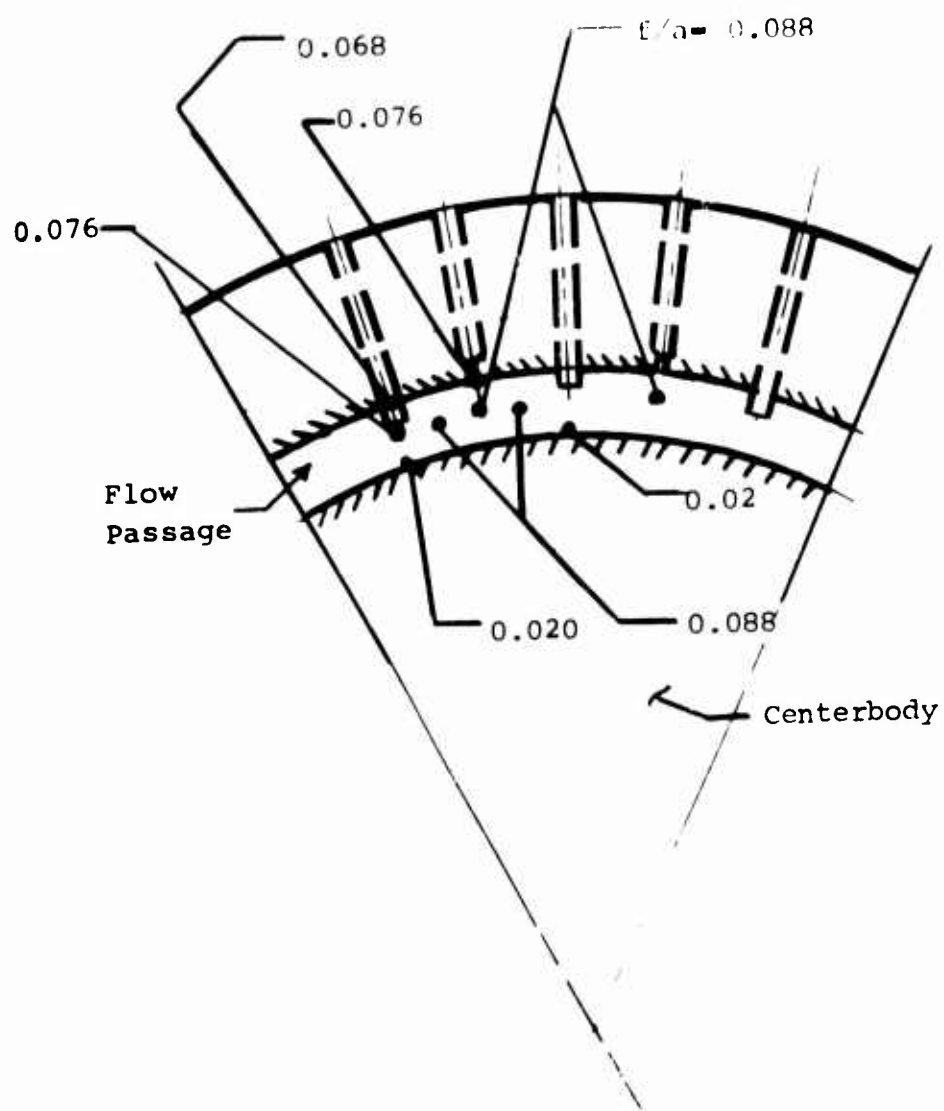


Figure 18. Calculated Fuel-Air Ratio at Slot Region.

COMBUSTION

The GASL finite-rate reaction and turbulent-mixing computer program was used to define the flow processes and thus the burner area variation in order to provide the desired constant-pressure burner flow. This program is reviewed in some detail in Appendix III. As the flow channel in the present burner was an annular passage with a height to radius ratio over 10, the 2-D analysis was utilized. A series of computer "experiments" was performed in order to lay out the burner design. Some of these experiments will be pointed out below. First discussed, however, are the initial conditions and the method whereby they are computed - a necessary prerequisite for the computer program. Next, a flow model is postulated for the slot flameholder flow followed by a discussion of computed isotherms, burner flow area distribution, and effect of pilot temperature.

Initial Conditions

Since the overall fuel-air ratio is much less than stoichiometric, the fuel must be mixed with only a portion of the incoming air. This zone type of fuel distribution is schematized in Figure 19, and three initial zones are seen: a pure air region, a mixed fuel-air region, and the slot flameholder region. The latter two zones are discussed next.

1. Slot Flameholder

To define the hot, recirculating flow in the slot, the following assumptions are made:

- a. Pilot gas axial velocity is taken as 10 percent of the free-stream value (see discussion below).
- b. There are no circumferential or radial pressure gradients or velocity components.
- c. Thermodynamic properties correspond to those resulting from JP-4 combustion at $f/a = 0.0405$ or $f/a = 0.0676$ (stoichiometric).
- d. One-half of the slot depth is considered in order to account for the recirculating flow.

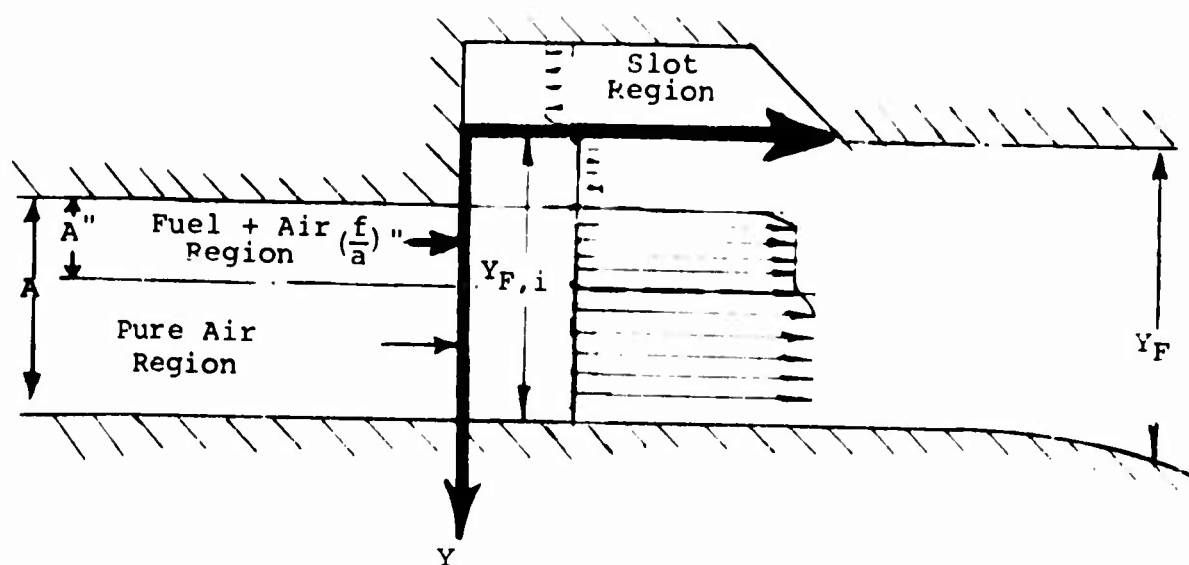


Figure 19. Definitions Of Coordinate System.

These assumptions coupled with the slot dimension determine the pilot mass flow. Previous computational experience at GASL has shown that when the level of pilot to free-stream mass flows is small (1/50) changes in this ratio have little effect on combustion characteristics. Thus the above procedure can be used to define the initial pilot flow data to study mainstream flame initiation and propagation.

2. Fuel-Air Region

Since the fuel is injected into the burner in the liquid phase and at a lower temperature than the airstream, the following analysis was used to determine the state of the fuel-air mixture. It was assumed that the flow was one-dimensional and of constant area and that only the streamtube containing the fuel had contributed to its vaporization or sensible enthalpy increase. As the fuel was injected normal to the airflow, its momentum flux was ignored. Therefore, from conservation of momentum,

$$pA_a'' + \frac{\dot{m}_a}{g} V = p_m A_a'' + \frac{\dot{m}_f}{g} V_m \quad (65)$$

energy,

$$H_m = \frac{1}{1 + (\frac{f}{a})''} H_a + \frac{(\frac{f}{a})''}{1 + (\frac{f}{a})''} [H_f + \epsilon] = e_m + \frac{V_m^2}{2} \quad (66)$$

and mass,

$$\dot{m}_m = \dot{m}_a + \dot{m}_f = \dot{m}_a \left[1 + \frac{f}{a} \right] \quad (67)$$

along with the perfect gas equation of state,

$$p_m = \rho_m \frac{R}{mw_m} t_m = \bar{p}_a + \bar{p}_f \quad (68)$$

and the identity concerning the flow areas,

$$\frac{A_a''}{A} = \frac{\dot{m}_a''}{\dot{m}_a} = \frac{f/a}{(\frac{f}{a})''} \quad (69)$$

the flow parameters adjacent to the pilot slot are found. In the above equations

\bar{p} = partial pressure

A'' = flow area containing fuel

H = stagnation enthalpy

e = static enthalpy

$(f/a)''$ = fuel air ratio in the region A''

The design point unmixed conditions which are necessary for these calculations are listed in Table III.

TABLE III. UNMIXED AIR AND FUEL CONDITIONS		
Item	Air	JP-4 Fuel
Velocity, fps	800	10
Stagnation Temp., °R	1200	500
Static Pressure, psia	139	139
Molecular Weight	28.9	128

Besides the stoichiometric fuel-air layer, a saturated fuel layer and a fuel-air ratio of 0.405 layer were also evaluated. The saturated condition was the extreme case where the amount of fuel just necessary to saturate a given stream tube of air was determined. The smaller f/a case showed the effect of lower flame temperature on burner design. The mixture conditions at the slot-pilot for these fuel layers are given in Table IV.

TABLE IV. DEFINITION OF FLOW QUANTITIES AT THE IGNITER STATION									
Definition	Stoichiometric Layer		Saturated Layer		f/a = 0.0405 Layer				
	Pilot	Fuel/Air	Pilot	Fuel/Air	Pilot	Fuel/Air	Pilot	Fuel/Air	Air
Temperature, °R	4500	1075	1200	4500	666	1200	3500	1075	1200
Velocity, fps	80	570	800	80	259	800	80	641	800
Pressure, psia	140	140	140	140	140	140	140	140	140
Height, in.	0.125	0.10	0.132	0.125	0.03	0.202	0.125	0.139	0.093
Fuel-Air Ratio	0.067	0.067	0	0.067	0.5	0	0.0405	0.0405	0

Results of Computations

The calculations are begun at the entrance plane of the slot. The radial distance Y , see Figure 19, is initially at $x = 0$, measured from one-half the depth of the slot, and the distance Y_F represents the entire flow dimensions and is thus a function of axial distance. In subsequent paragraphs, the isotherms generated by the stoichiometric fuel-air layer and the saturated fuel-air layer will be described in detail, but first some of the combustion phenomena are briefly outlined to make clear the meaning of the various isotherm distributions.

When a combustible mixture is ignited, two basic phenomena occur. First, there is an incubation period during which no sensible heat is released but which creates the free radicals necessary for the reaction. This is called the ignition-delay time. The second phenomenon features the large heat release associated with flames and is called the reaction time. In the present burner configuration, there is a third phenomenon due to the fuel and air distribution: this is the mixing which occurs subsequent to the combustion.

In Figure 20, the isotherms produced by the saturated fuel-air case are portrayed. A very long ignition delay distance is indicated, approximately 3 inches, which is due to the time taken for the diffusion of external oxygen and reaction with the high-temperature fuel. After ignition, the flame spreads rather rapidly in a very intense zone for an axial distance of about 6 inches. At this point the slope of the isotherms decreases indicating that most of the fuel is burned and that only the mixing with the unburned air is continuing. Here the flame has filled only one-half the flow passage and was thus deemed to be unacceptable.

The stoichiometric fuel-air layer generated isotherms are shown next in Figure 21. The ignition, combustion, and mixing zones are seen again; but now at an axial distance of 6 inches, the flame has filled three-quarters of the flow channel. The turbulent mixing process completes the flow homogenization by $x = 1.1$ ft. This latter point can be seen from the temperature profiles computed at various axial stations and shown in Figure 22; by $x = 1.07$ ft., the pattern factor is 12 percent.

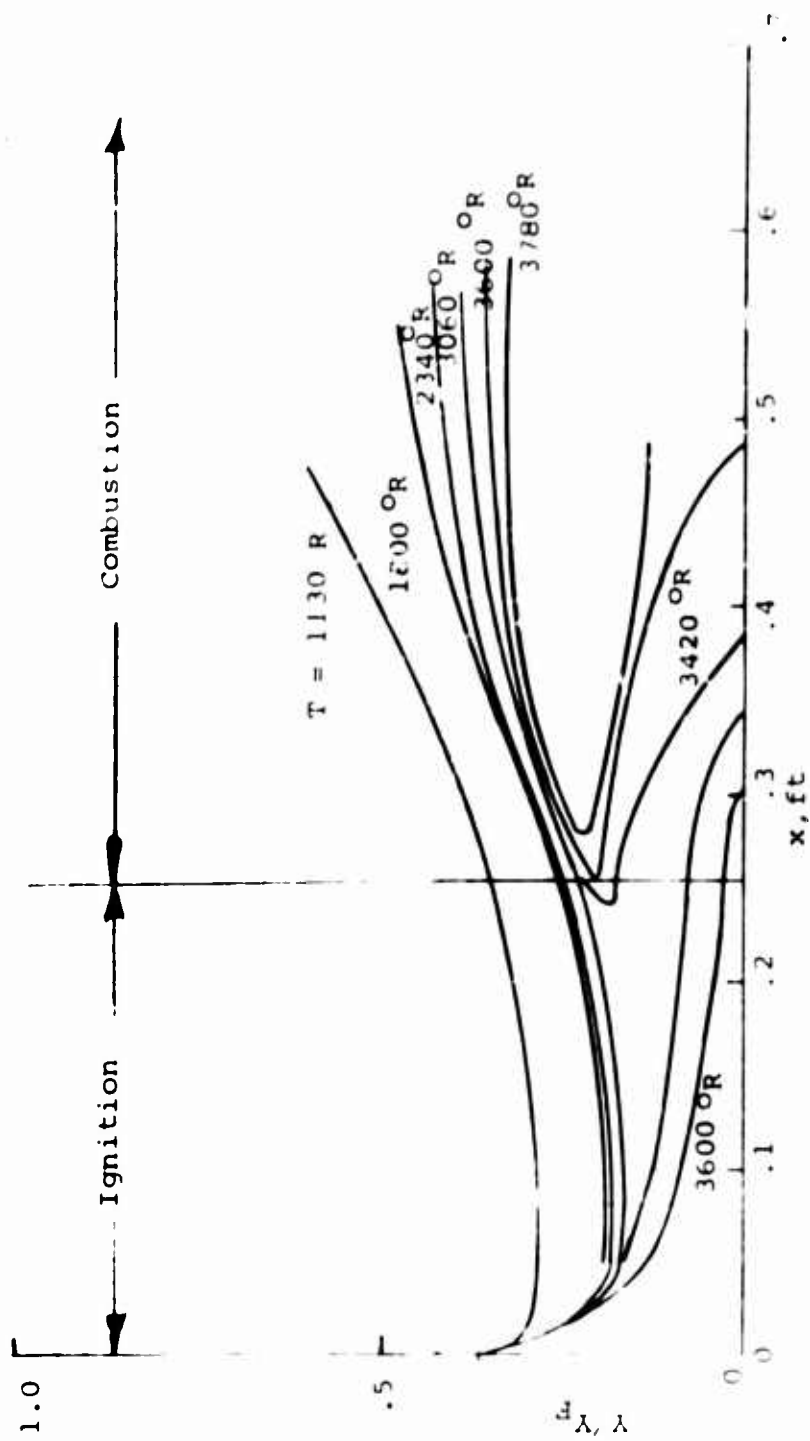


Figure 20. Isotherms Produced by Saturated Fuel-Air Layer.

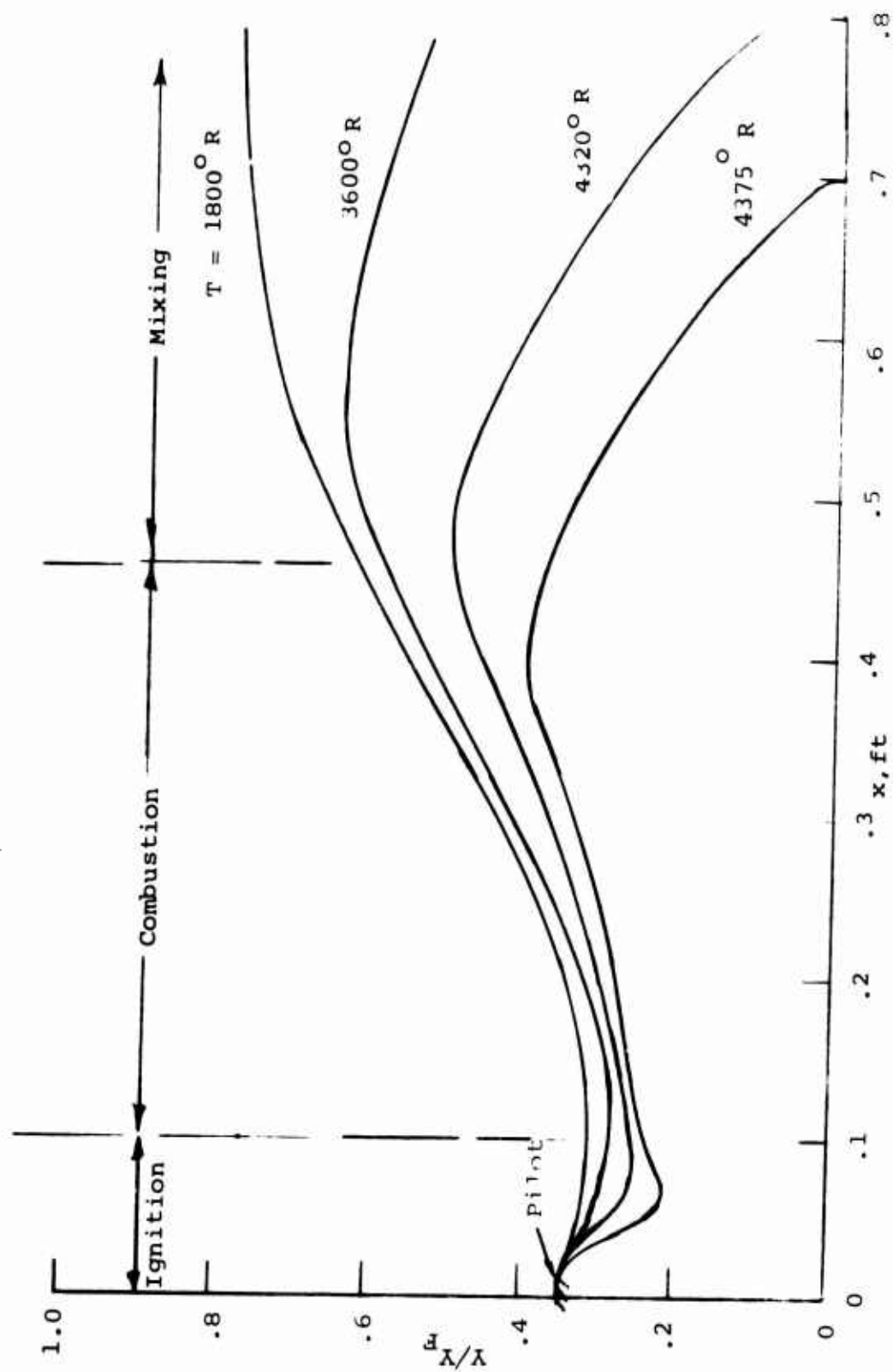


Figure 21. Flame Propagation With Stoichiometric Fuel Layer

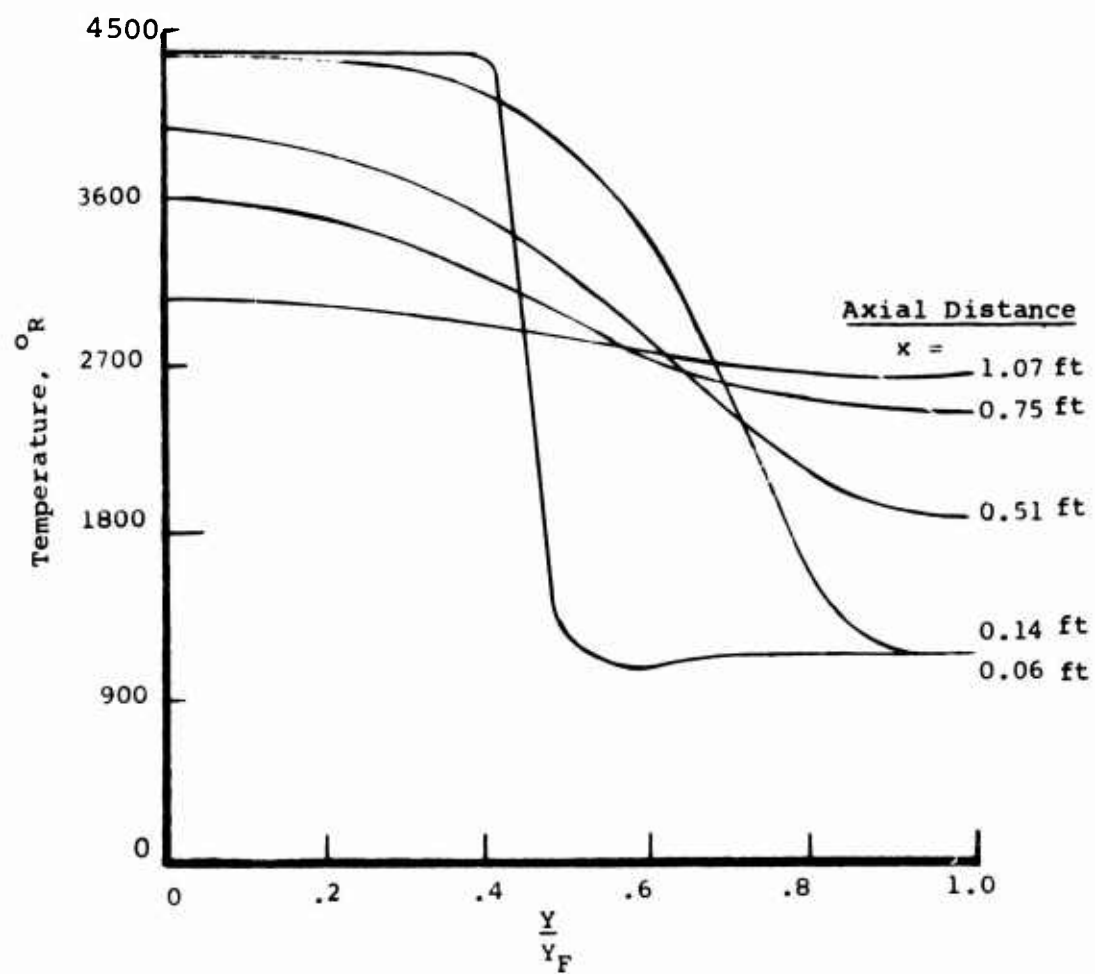


Figure 22. Temperature Profiles at Various Axial Stations.

To examine the sensitivity of the piloting and flame speed due to pilot temperature and initial fuel-air ratio, the case of $f/a = 0.0405$ (the lean flammability limit) and 3000°F pilot was examined. Results are shown in Figure 23 in terms of the isotherm spread. It should be noted that this figure shows only the initial portion of the combustion zone. These results show that ignition and combustion were possible at a low pilot temperature and that the ignition delay time is of the same order as the stoichiometric layer. Flow area variation is shown in Figure 24, which also portrays the difference in the two types of fuel layers. It may be seen that in both cases extensive flow area variation is predicted downstream of the flameholder slot. Since the stoichiometric fuel-air layer provided the smaller burner length, this configuration was adopted for the burner design.

Thus, from the analysis of liquid droplet breakup and organization, fuel-air mixing, flame stability, and the chemical kinetics and turbulent mixing processes, the basic layout of the burner was defined. The following section discusses the burner and test facility design.

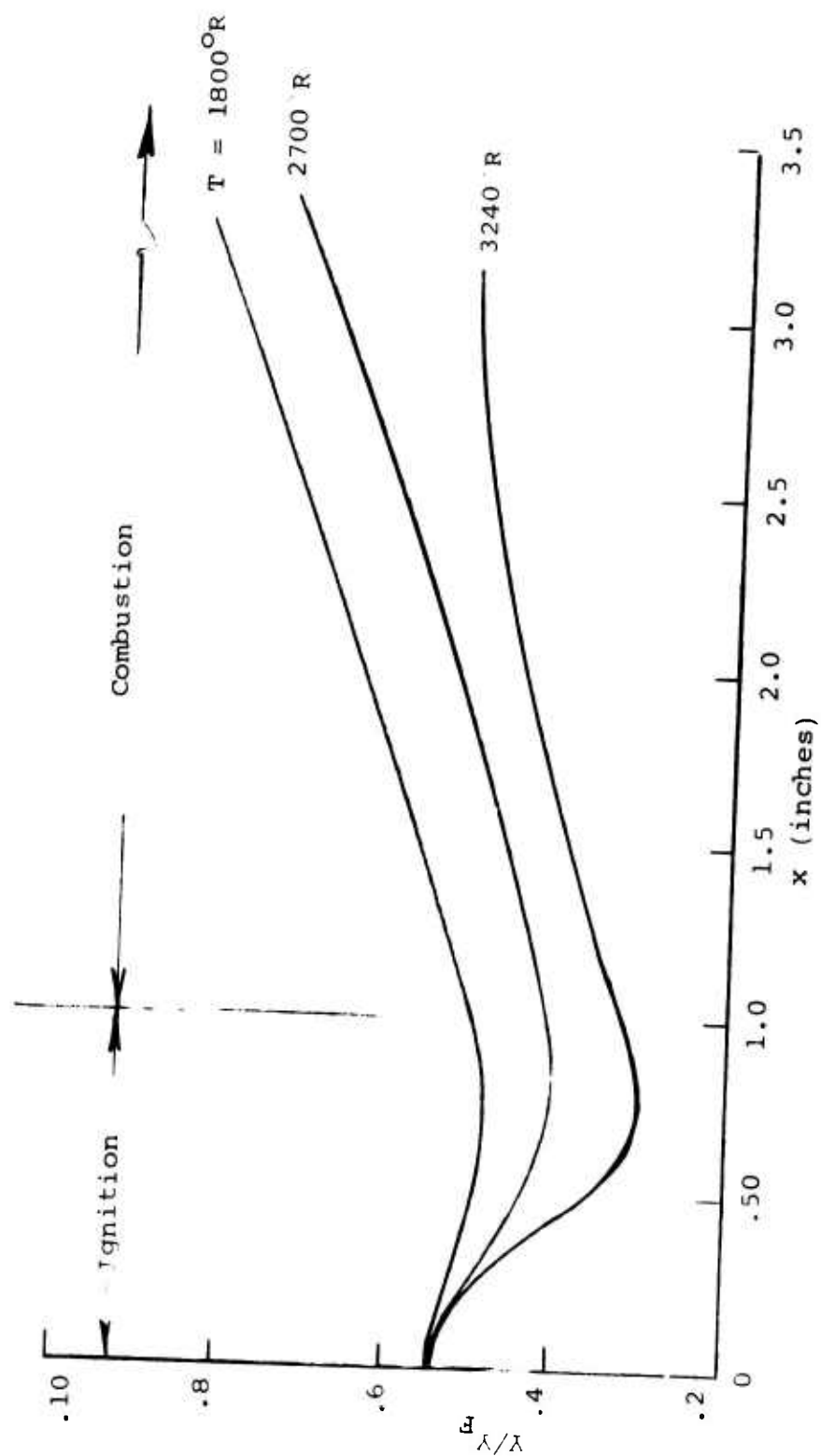


Figure 23. Isotherms Produced By "Low" Temperature Pilot
 $f/a = 0.0405$ Fuel-Air Layer.

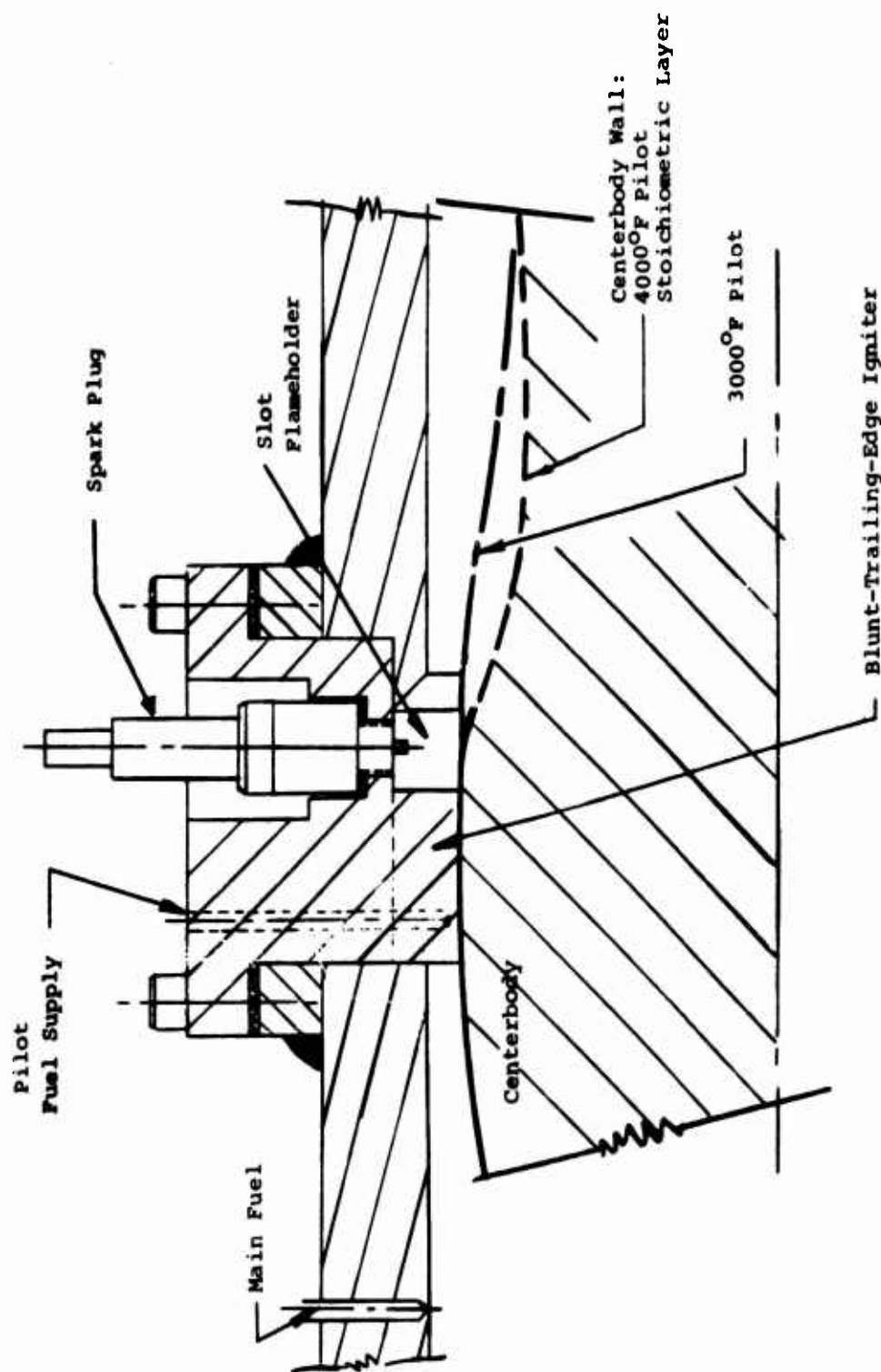


Figure 24. Drawing of Typical Igniter and Flameholder Slot

IV. DESCRIPTION OF FACILITY

Along with the high-speed burner, this section describes the test facility, the associated fuel pumping and metering system, and the burner instrumentation. Since the burner entrance conditions had to be varied over a rather wide range in order to duplicate the altitude-power spectrum shown in Section II, the test facility featured variable mass flow, stagnation temperature, and pressure. The technique used to control the burner entrance flow is described.

A schematic of the test facility is shown in Figure 25.

TEST SETUP

The burner model is direct-connected to the GASL vertical pebble bed heater. This heater consists of a 1500 psia maximum pressure vessel containing alumina pebbles heated by "Globar" electrical resistance heaters. This facility is capable of providing complete simulation of the actual engine mass flow, temperature, and pressure.

The outlet of this heater is a sonic orifice, and therefore the airflow sustains subsequent diffusion to subsonic conditions by a shock system. The level of stagnation pressure behind the shock is dependent upon the shock location so that pressure levels from the heater stagnation value to almost ambient can be obtained.

From the pebble bed heater, the flow enters a settling chamber, which consists of a constant-area duct about 14 inches long with a converging section at the downstream end to match the combustor diameter. Because of the length of the settling chamber and other piping upstream of the burner and the relatively narrow burner annulus height, the boundary layer was calculated to be too large and would mask the high-speed combustion phenomena. A boundary layer ram scoop is located at the leading tip of the converging section. The height of the ram scoop, .070 inch, is equal to the calculated local boundary layer displacement thickness. The flow rate of air removed from the facility is continuously measured with choked venturis so that the burner inlet airflow is precisely known.

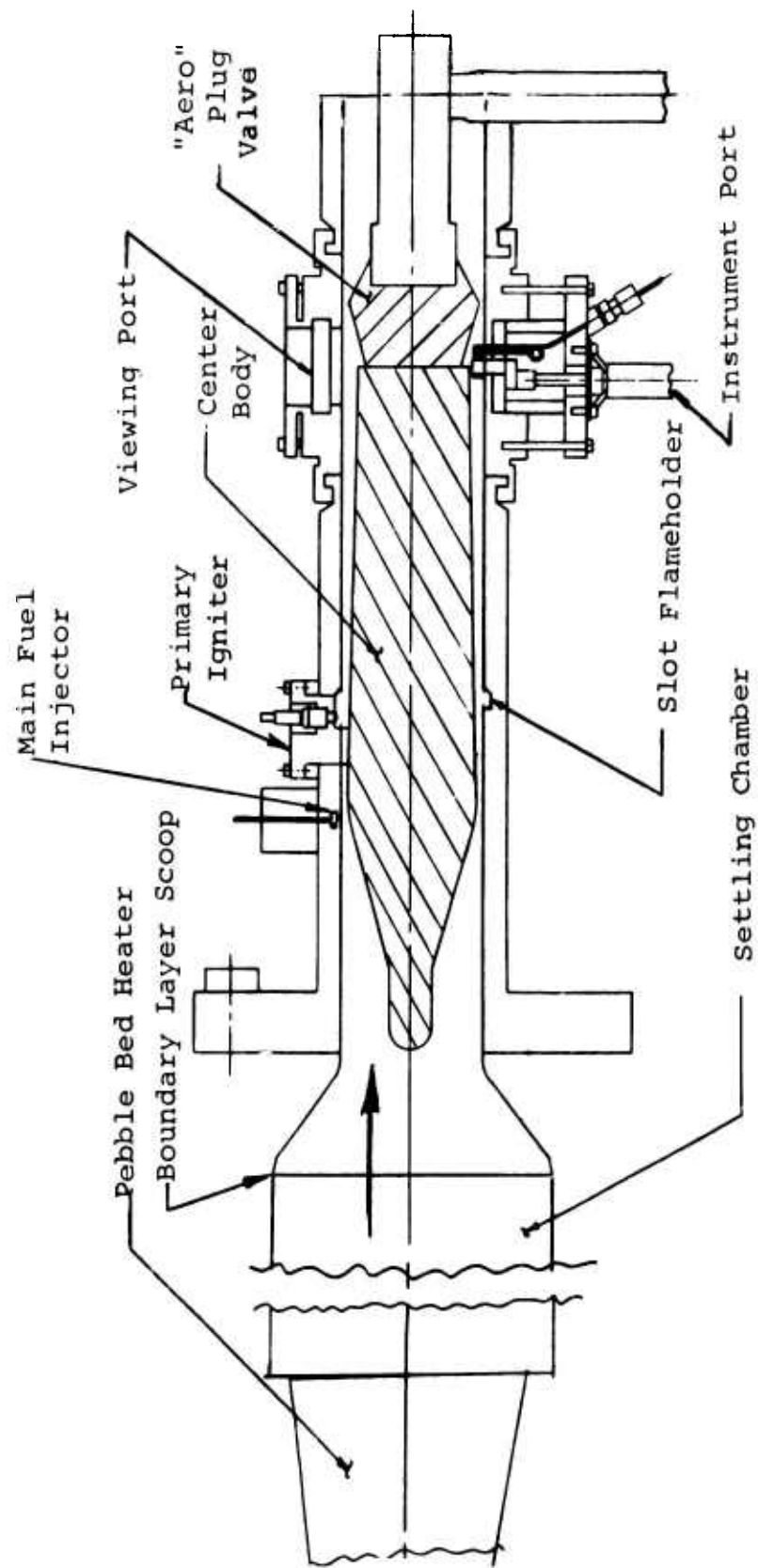


Figure 25. Schematic of Test Facility.

The burner is formed by the annulus composed of a cylindrical outer shell and a conical centerbody. The outer diameter of the burner flow section is 5.05 inches and the annular height is 0.232 inch at the igniter plane. The burner measures 12 inches from the slot to the exit and the cone half angle is $1^{\circ} 29'$. The resulting flow area distribution is different from the one prescribed by the computer analysis because it was believed to be more prudent to test first a simply shaped body having the design length and inlet to exit flow area ratio.

The burner centerbody which is shown in the photograph, Figure 26, is supported at three axial locations for structural rigidity and concentricity. These locations are at the model leading edge, at the primary igniters and at the "Aero"-plug exit. The photograph also shows the boundary layer scoop exhaust tubes as well as the burner attachment flanges. The burner section was designed so that it could easily be disassembled for modification and repair. Figure 27 shows the outer shell of the burner mounted to the attachment flange. The blunt-body-pilot attachment bosses and the rear instrumentation and view housing are seen in the figure.

A drawing of the ignition region is shown in Figure 28, where the primary igniters and the circumferential slot are detailed. To be noted are the fuel galleries and the spark plug located in the blunt-trailing-edge igniter.

The main fuel injector configuration that was chosen is shown in Figure 29. There are 40 co-planar injection orifices, 20 each of the flush and the off-wall types, emanating from a common plenum. Each orifice has the same outlet flow diameter: 0.032 inch. The off-wall injector protrudes approximately 0.10 inch into the airflow.

The downstream portion of the test burner's outer shell is capable of rotating 360° . This arrangement facilitates circumferential surveying of the annular flow field. Two diametrically opposed Pyrex windows may be installed in this section. Each window provides a 2.25-inch viewing port and is used for observation and photography. In addition, the ports are designed to be used as mounts for instrumentation rakes. Because of the high temperatures prevailing in the

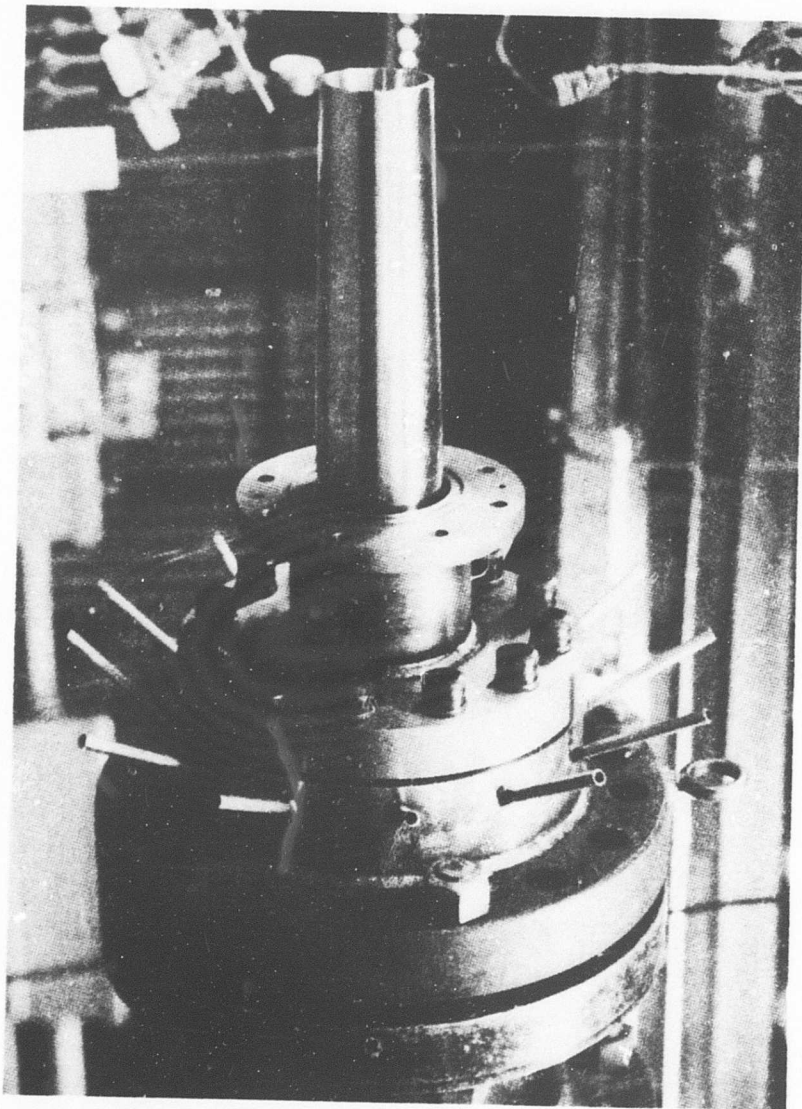


Figure 26. Burner Centerbody.

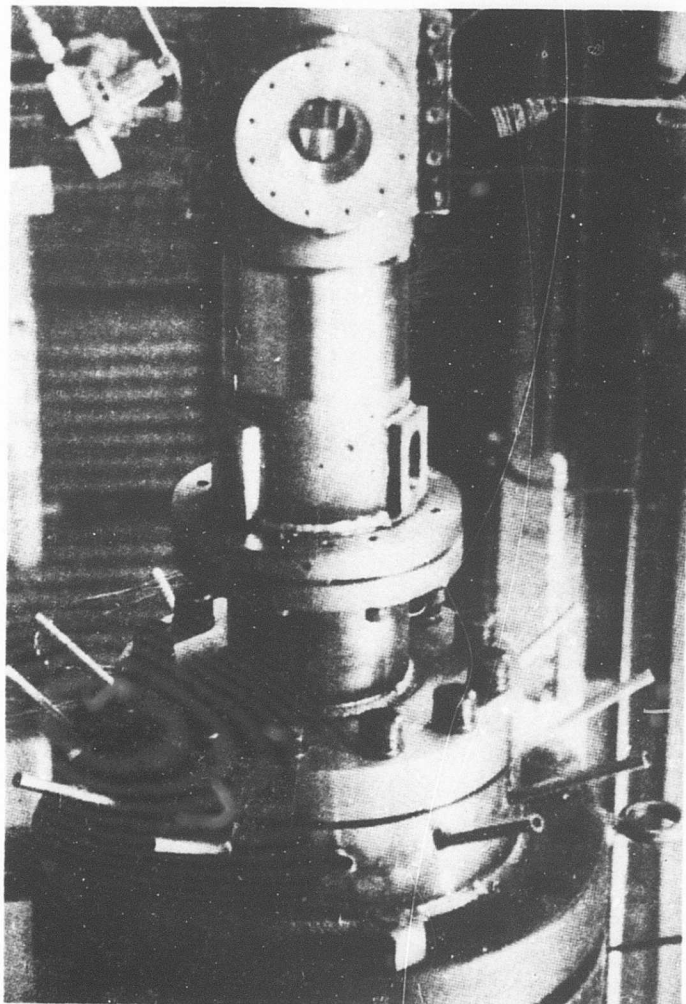


Figure 27. Viewing Port and Instrument Port Housing.

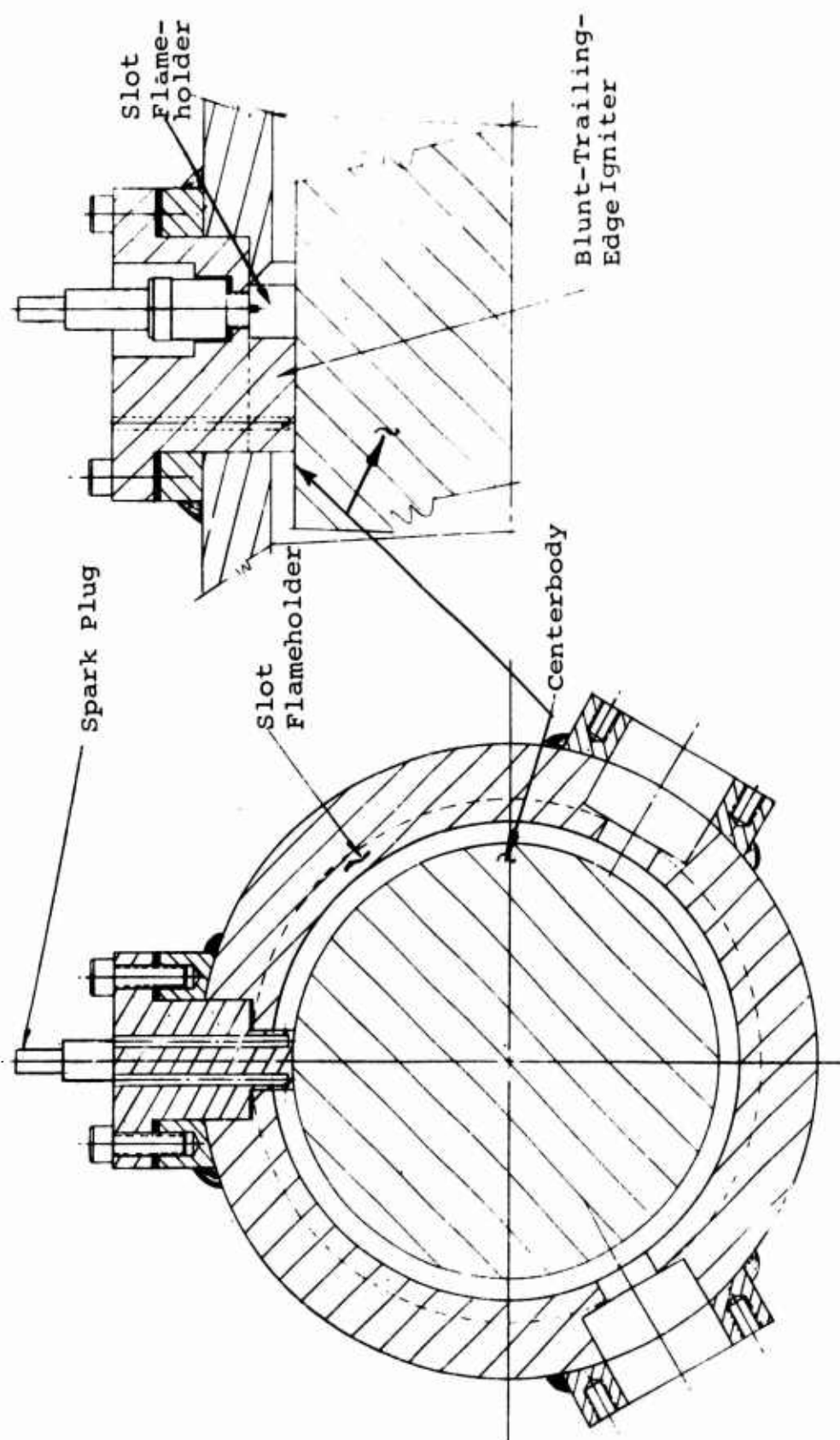


Figure 28. Detail Drawing of Igniter Region.

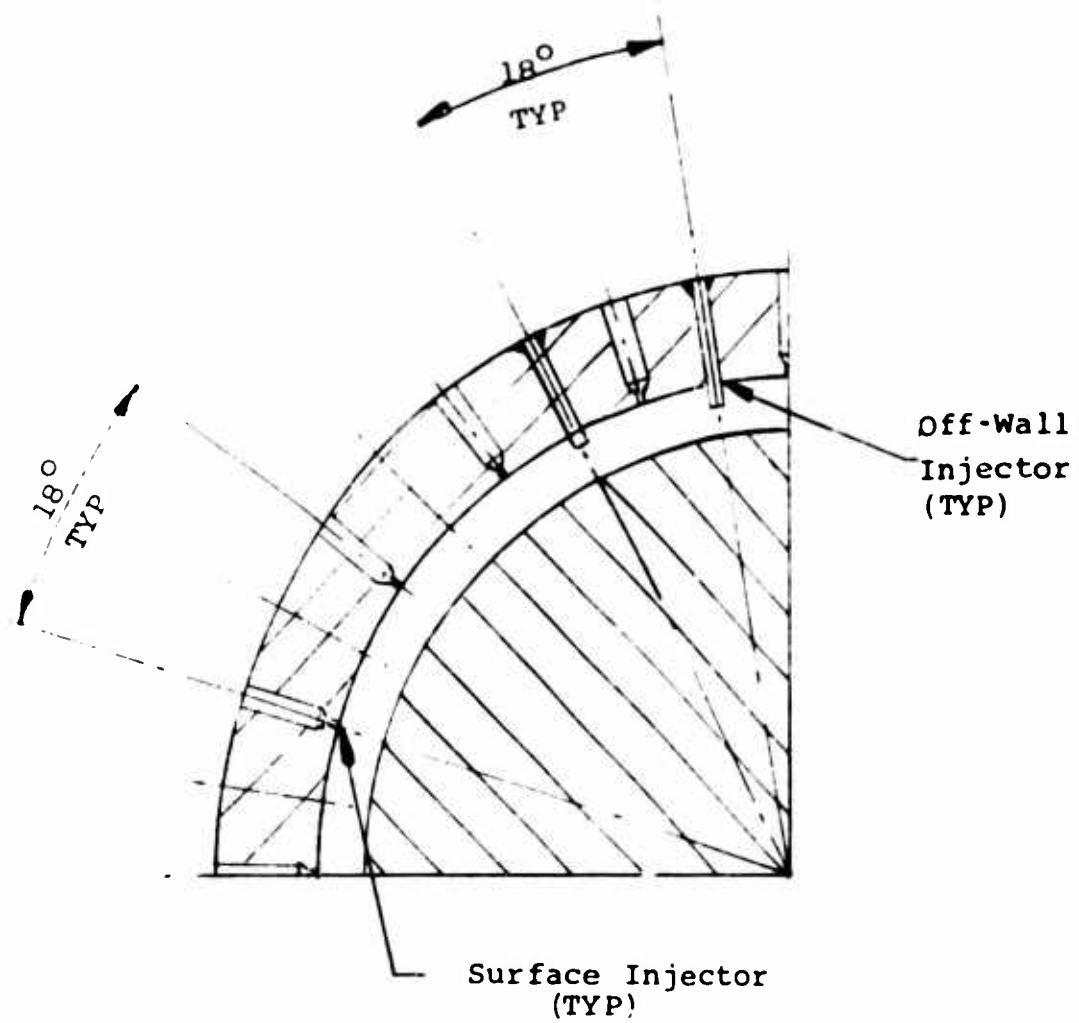


Figure 29. Layout Of Main Fuel Injector Configuration.

combustor flow field, the rakes are recessed in a cavity and kept out of the flow until needed. On signal, a pneumatic actuator inserts and withdraws the multiprobe rakes.

To obtain the desired pressure level, an aerodynamic plug valve was located downstream of the test burner. This plug valve consisted of a geometric constriction and varying amounts of cold air injected to create a sonic condition at the plug. Thus, at a given burner mass flow, the entrance pressure level is varied by the rate at which cold "plug" air is added. The plug airflow required for this control system is shown in Figure 30 as a function of fuel-air ratio for burner inlet air conditions corresponding to the 100 percent and 60 percent power levels.

The design of a combustion test model included a heat transfer and stress analysis and the evaluation of a number of thermal protection schemes. These are detailed in Appendix IV, where it is shown that sufficient heat sink cooling is available for relatively long experimental tests.

INSTRUMENTATION

The instrumentation rake had three stagnation pressure and three stagnation temperature probes, fixed side by side, 1/8 inch apart. The pitch between each probe was 1/8 inch. The stagnation temperature probes were miniature unshielded/ceramo-type platinum-platinum, 10 percent rhodium thermocouples. In addition to the rake measurements, wall static pressure and wall temperatures were measured. A Scanivalve pressure distributor was used to monitor the many pressure taps; however, continuously-reading transducers were used to monitor the more important pressures, such as the burner stagnation pressure and fuel pressure.

Fuel System

A schematic diagram of the fuel system is shown in Figure 31. Three independent fuel supplies were included in the system. One of these was used for the pilot fuel and the others supplied the main fuel. The indicated venturis measured the liquid flow rates, and since they were a cavitating type, they also uncoupled the flow rates from any downstream pressure variations thus divorcing the fuel system from oscillations in the combustion chamber.

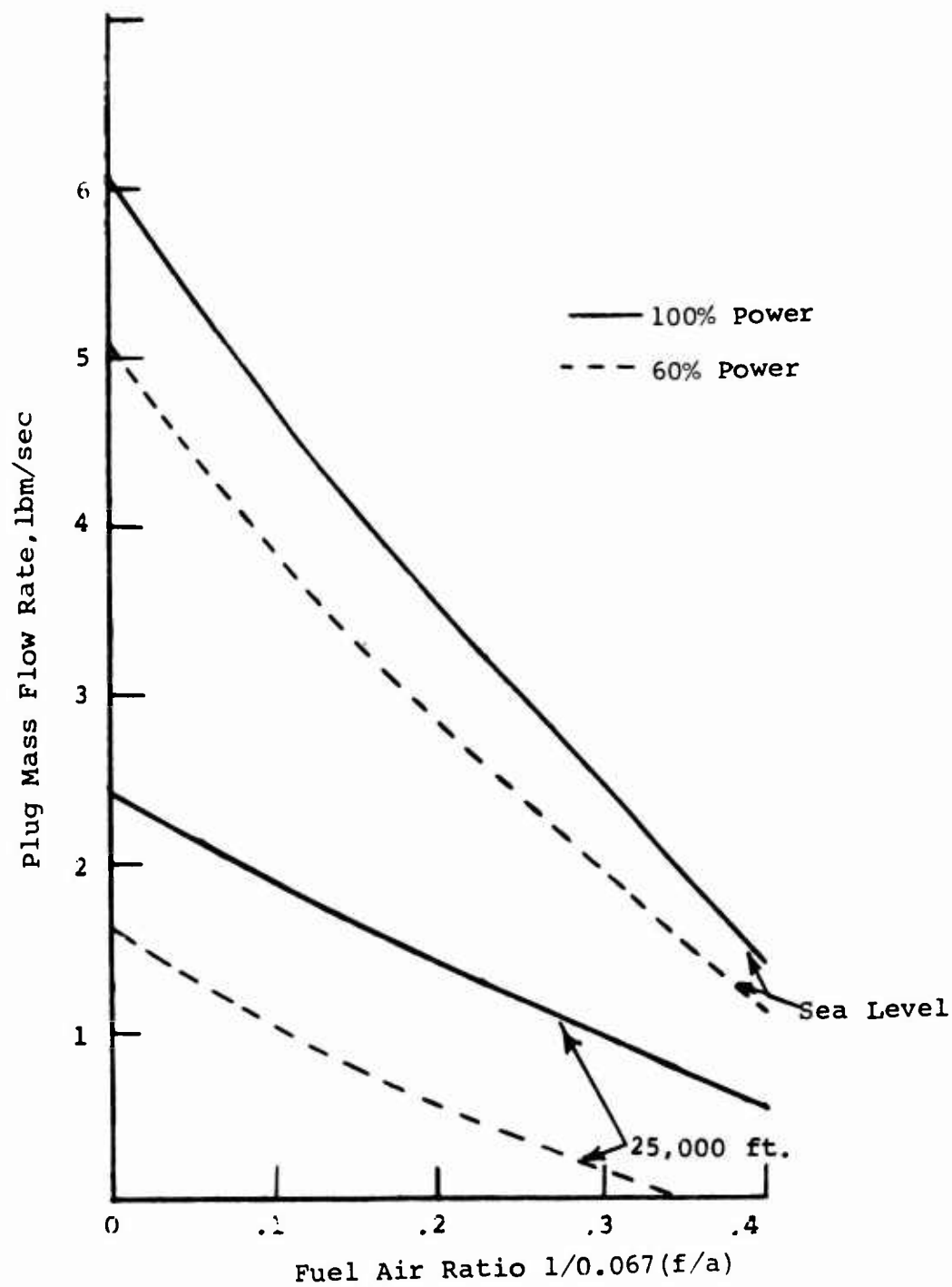


Figure 30. Typical Plug Mass Flow Rates.

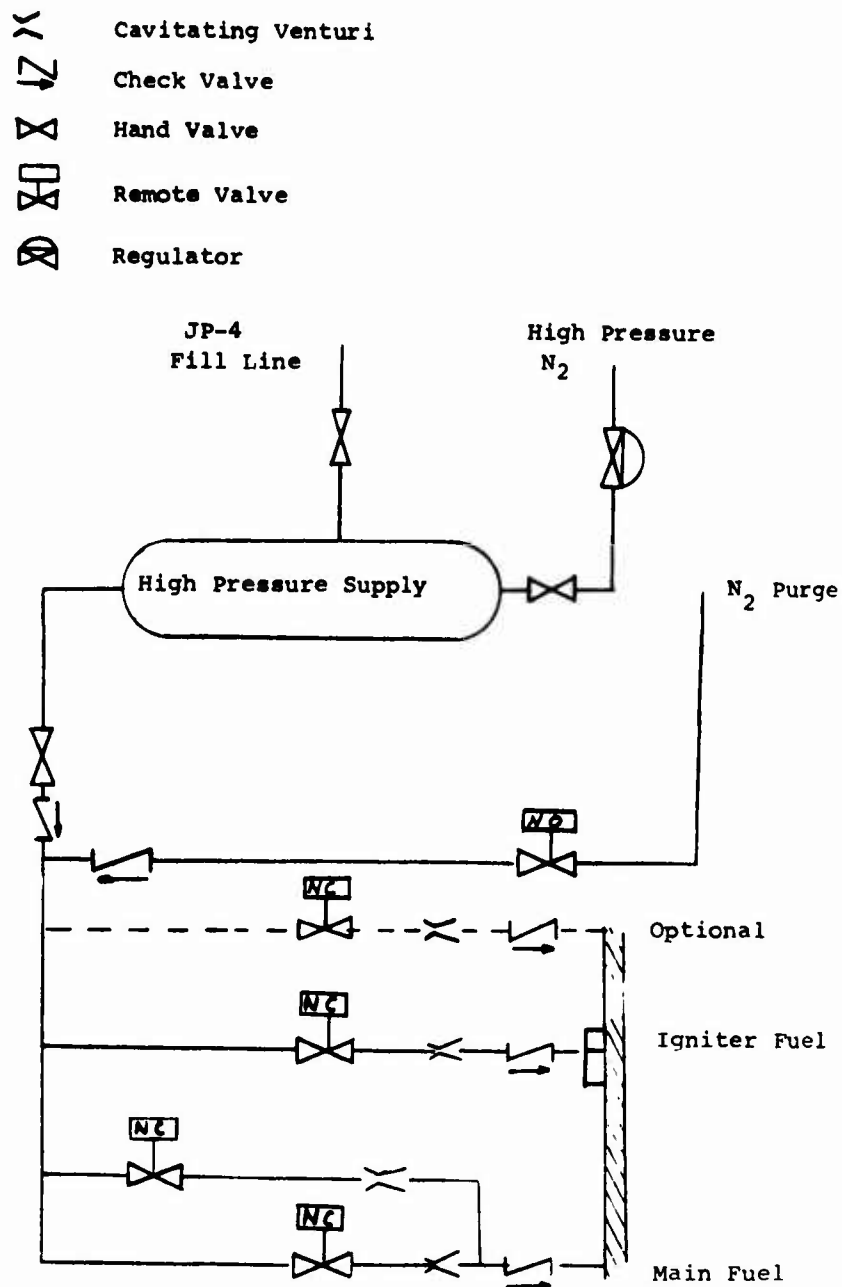


Figure 31. Fuel Piping Schematic for Army/GASL Combustor.

The fuel system was calibrated prior to testing since the cavitating phenomenon precludes absolute knowledge of the orifice coefficients, recoveries, and range over which the venturis provided cavitating-type performance. The results of the calibration tests are shown in Figure 32 for two different venturis.

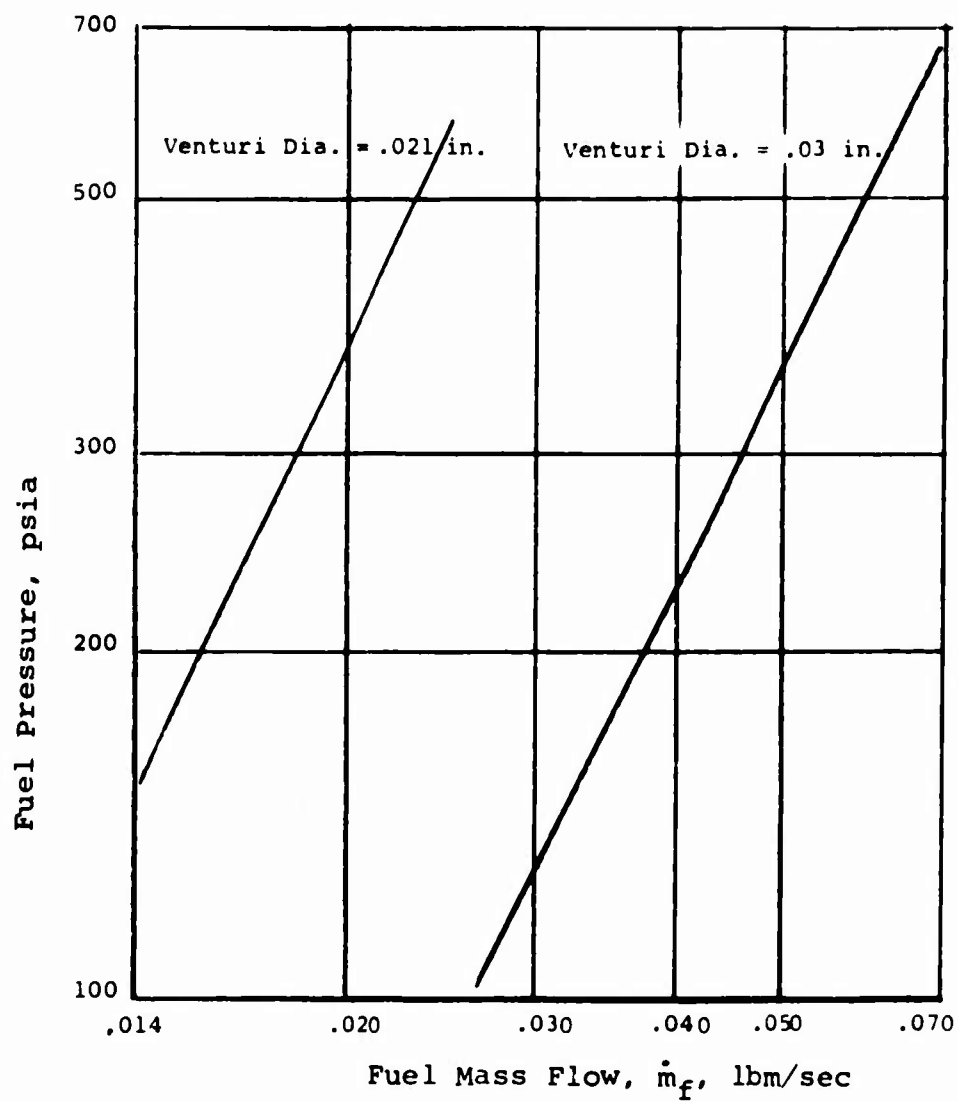


Figure 32. Calibration Results of Cavitating Venturis.

V. PRESENTATION AND DISCUSSION OF THE EXPERIMENTAL DATA

It was desired to accomplish the following tasks in the experimental portion of the program: first, to demonstrate ignition and combustion over the wide range of operating conditions with the small, annular, high-speed burner configuration; second, to obtain predicted performance and thus prove the viability of the burner concept; and finally to improve burner performance, e.g., by eliminating the primary igniters. Only the first item was unequivocally demonstrated.

No difficulty was experienced in lighting-off even at burner inlet Mach numbers as high as 1. Circumferentially, uniform stagnation pressure and temperature distributions could not be achieved, with the result that approximately 25 percent of the total volumetric flow was devoid of combustion. As these unburnt regions are located centrally, i.e., between primary igniter stations, it is postulated that the slot pilot did not properly initiate combustion throughout the entire circumferential length.

The testing procedure called for mapping the entire operating range at each circumferential station before proceeding to the next station. Since the test conditions of inlet Mach number, total temperature, and fuel-to-air ratio could not be kept constant from run to run, a normalization procedure was adopted to portray the circumferential distributions of the significant quantities. With respect to the temperature measurements, the normalizing procedure was to divide the measured temperature by the value of the adiabatic flame temperature, T_{af} , where T_{af} was determined from the measured mass flows of air and liquid JP-4 and the GE tables (Reference 3). This normalization procedure introduced other problems, which are discussed under the heading Temperature Distribution. With regard to pressure, the recovery is plotted which effectively normalizes the measured pressure by the upstream stagnation value. Figure 33 defines the circumferential stations where data were taken.

The nominal flow conditions for each power setting are listed in Table V. A light-off case is also listed which demonstrated the capability of the test burner to initiate combustion under simulated startup conditions.

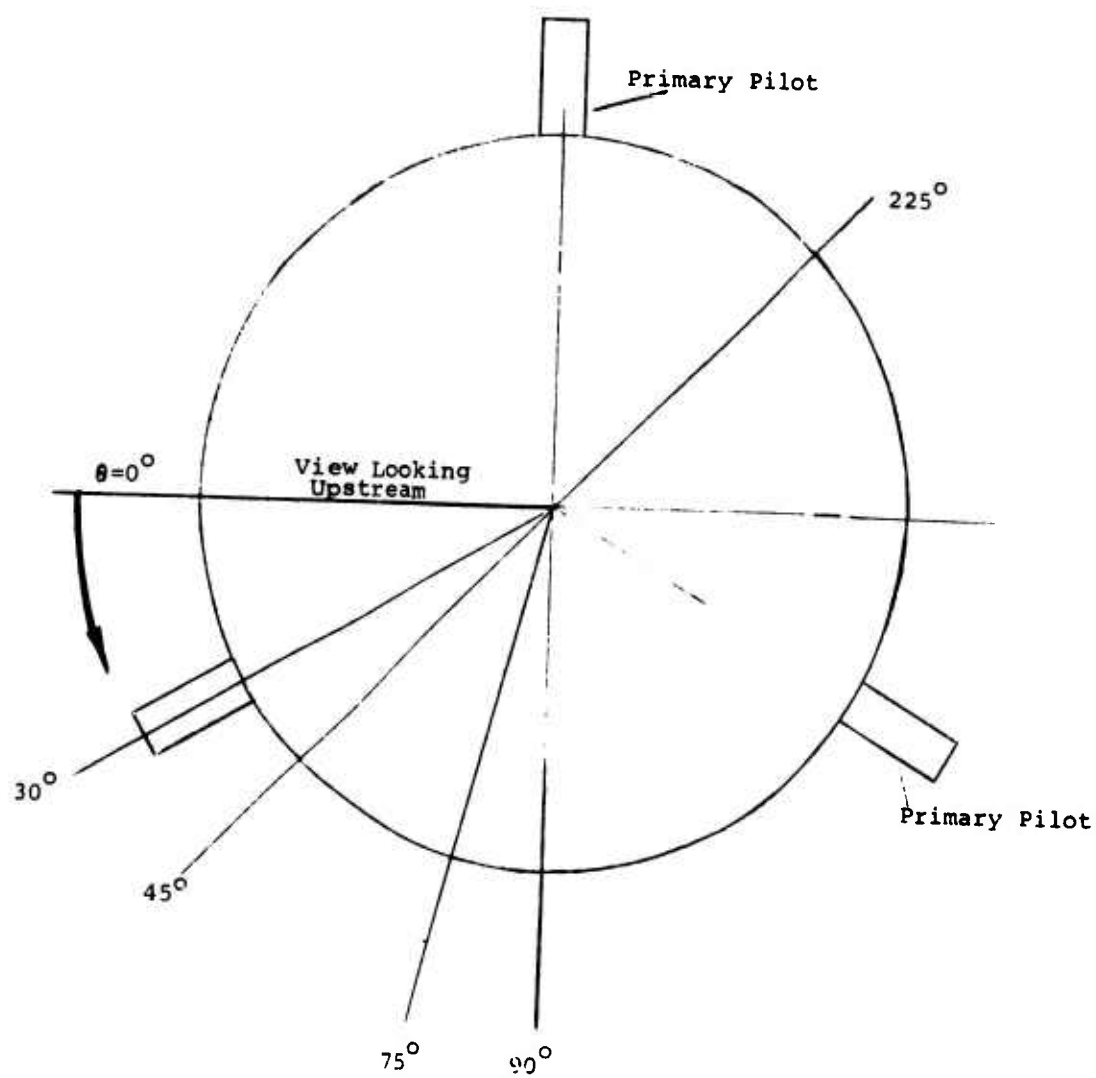


Figure 33. Definition of Circumferential Stations.

TABLE V. INLET CONDITIONS FOR ARMY/GASL HIGH-SPEED COMBUSTION TESTING					
Altitude (ft)	Power Setting (percent)	\dot{m} (lbm/sec)	T_3 ($^{\circ}$ R)	P_3 (psia)	f/a
Sea Level	100	5.0	1190	165	.032
25,000	100	2.0	900	61	.024
Sea Level	60	4.37	1120	131	.025
25,000	60	1.65	930	45	.02
Sea Level	20	2.96	970	82	.016
25,000	20	1.20	795	31	.015
Sea Level	Light-Off	0.7	520	15.2	.021

The data are portrayed as a function of the two main correlating parameters: fuel-to-air ratio and burner inlet Mach number. These two parameters are determined from the experimentally measured values as follows:

1. The fuel flow rate is fixed by the venturi orifice dimension and the measured nitrogen driving pressure. The airflow rate is the difference between the measured airflow at the exit of the pebble bed heater and the measured boundary layer bleed flow.
2. The burner Mach number is computed from the measured inlet air stagnation pressure and the average of seven static pressure taps located in the plane of the primary igniters just upstream of the blunt trailing edge.

TEMPERATURE DISTRIBUTION

The thermocouples used to measure the total temperature had a relatively small sensing bead diameter compared to their lead-in wire dimensions. Because this gives rise to large conduction errors, an analysis was undertaken to

determine the necessary correction and is given in Appendix V. Using this analysis, a temperature correction chart is shown in Figure 51 with which the true gas temperature is determined from the measured junction temperature.

The measured temperatures, corrected according to Figure 51, are shown in Figures 34 through 37 as a function of circumferential angle θ . The flow conditions associated with each graph are given in Tables X through XIII in Appendix VI. No data are shown for the 20-percent power condition because their distribution is similar to Figure 36. The burner inlet total pressure was used as the basic flow property to define the relevant power setting. No attempt was made to correlate the total temperature distributions according to burner inlet Mach number because of the lack of sufficient data. The measured circumferential temperature distributions reveal the following pattern: (1) downstream of the igniters, temperature is higher than adiabatic flame; (2) moving away in the θ direction, the temperature drops below adiabatic and remains constant at a value between 75 and 85 percent of T_{af} , depending upon power setting; and finally, (3) midway between igniter stations, combustion terminates very rapidly.

The problems of associating an overall fuel-air ratio with these measurements are now made apparent. The addition of primary igniter fuel causes the fuel distribution to be circumferentially nonuniform; and because of the low mixing rates, the temperature directly downstream of the igniter reflects this greater f/a and thus is higher than the adiabatic flame temperature computed with the average fuel-air ratio. If the actual fuel-air ratio were known at each point, the temperature could be normalized by its proper value so that the combustion efficiency might be indicated. Consider the following proposed fuel-air distribution which accounts for the fuel injected from the primary igniters (about 20 percent of the total): assume that one-half this fuel is diffused out by $\theta = 45^\circ$ and all by $\theta = 75^\circ$. Associating values of T_{af} to these equivalence ratios and normalizing the observed temperatures gives the dotted line marked "varying f/a " in Figure 34. If this circumferential fuel distribution is as postulated, then indicated combustion efficiency would be higher than that implied by the normalization based on a global T_{af} value.

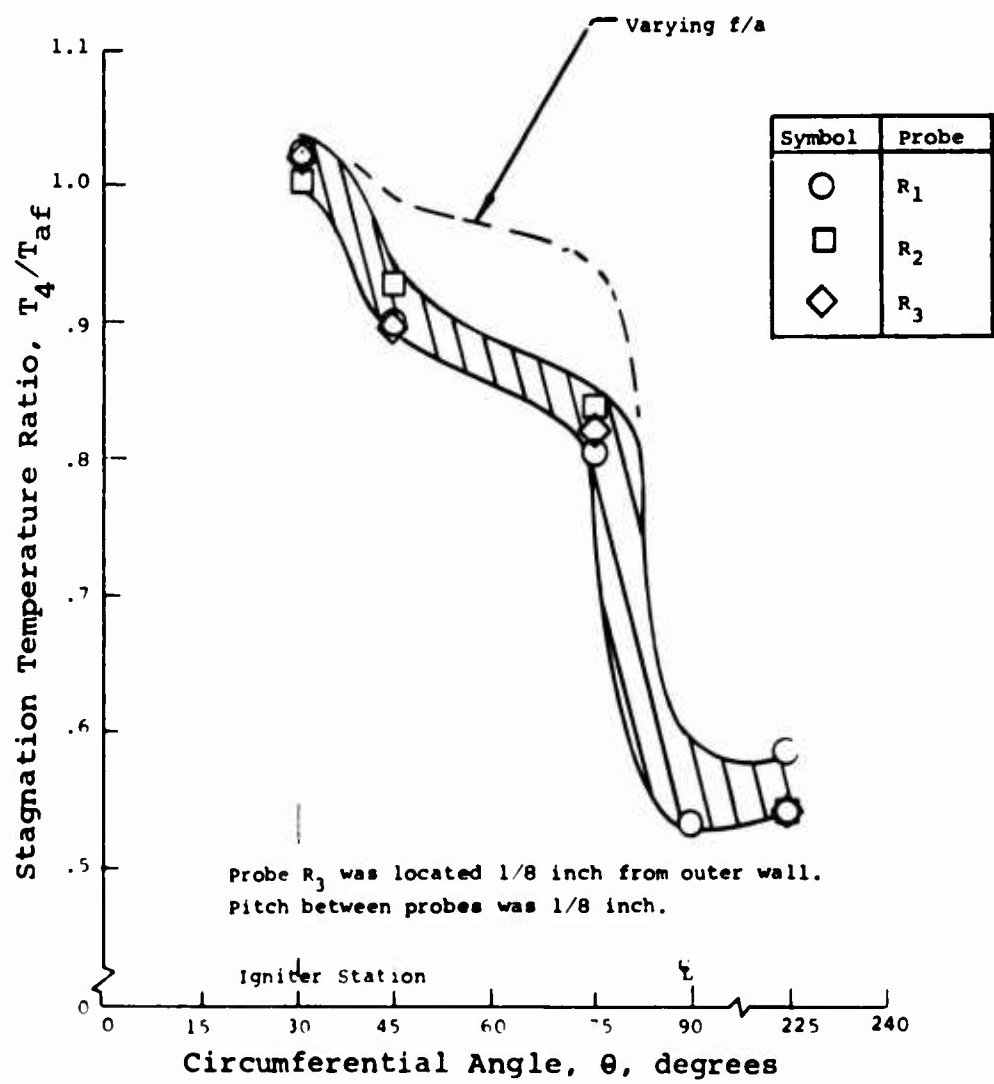


Figure 34. Circumferential Temperature Distribution, 25,000 ft, 100 Percent Power.

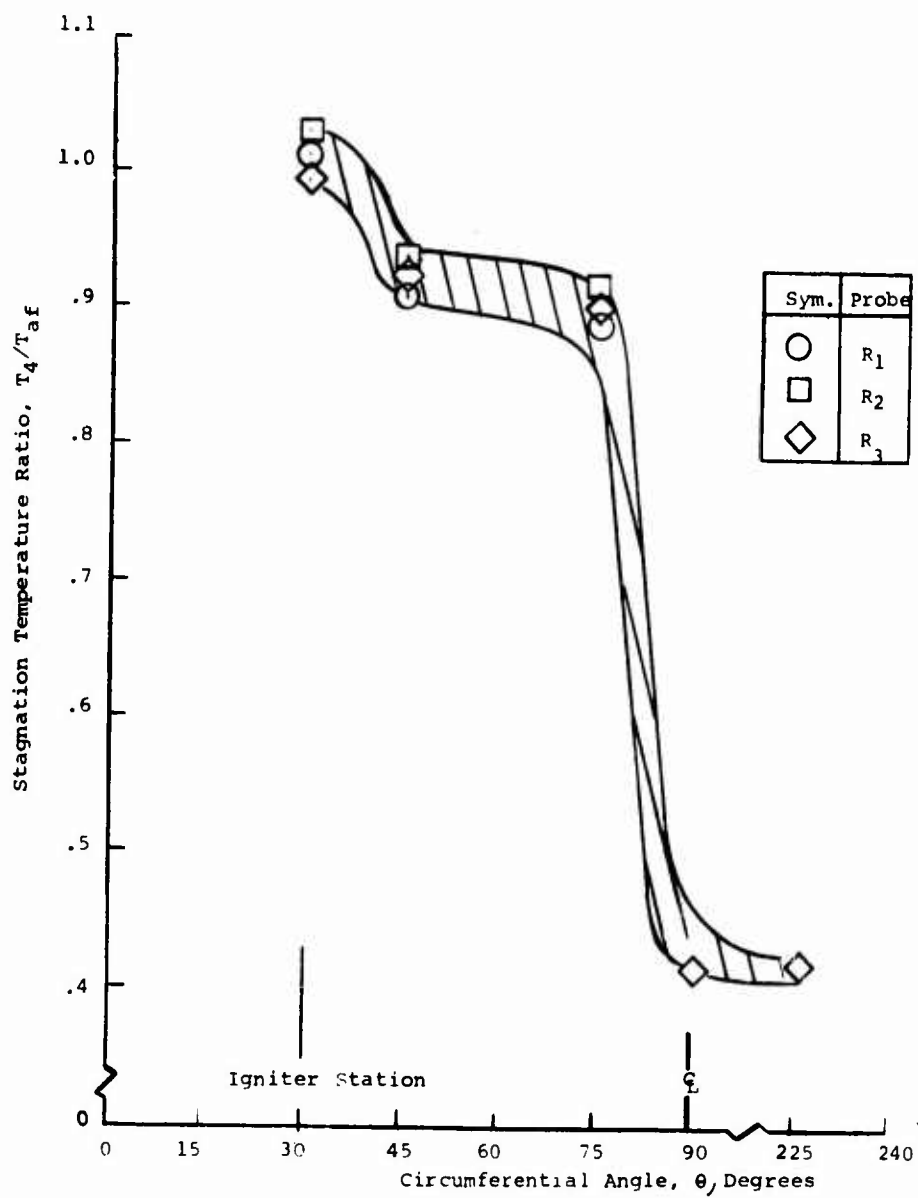


Figure 35. Circumferential Temperature Distribution, 25,000 ft, 60 Percent Power.

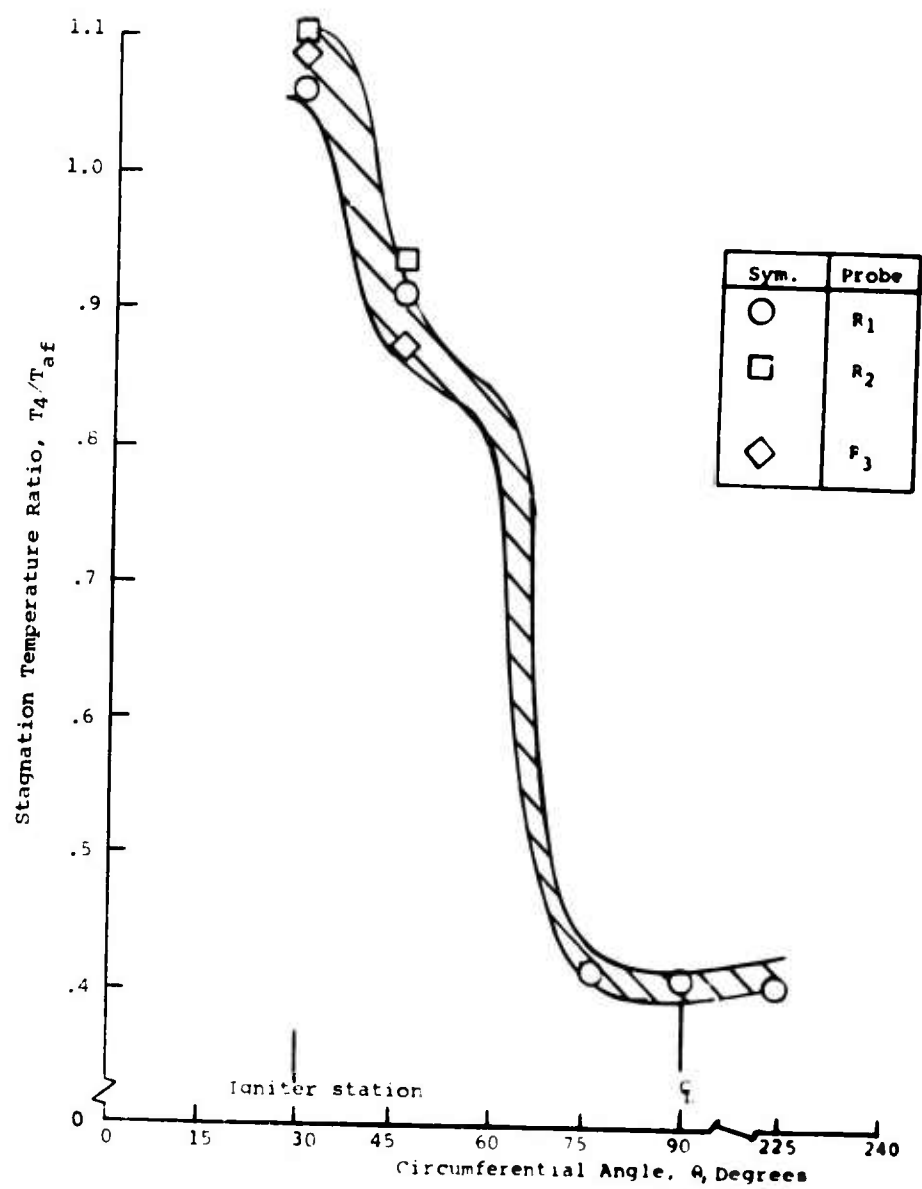


Figure 36. Circumferential Temperature Distribution, Sea Level, 100 Percent Power.

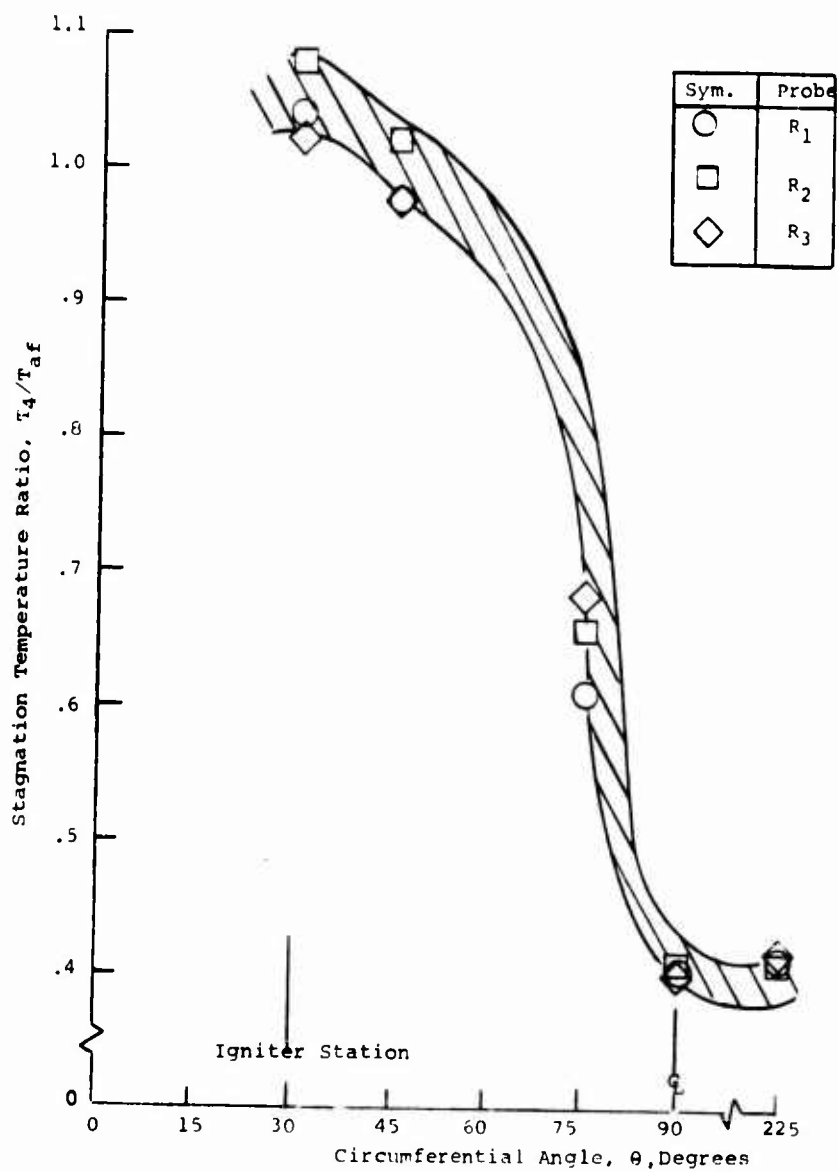


Figure 37. Circumferential Temperature Distribution, Sea Level, 60 Percent Power.

STATIC PRESSURE DISTRIBUTION

A typical example of the axial distribution of static pressure is shown in Figure 38 where the pressure is normalized by the burner inlet stagnation pressure. The line through the data bars represents the no-burning distribution, while the data points indicate the pressures during combustion. These data are from two different runs, both with identical burner inlet conditions. It is seen that without burning, the static pressure increases with axial distance because of the increasing burner flow area; heat addition accelerates the flow towards Mach 1 so that these two effects cause the resulting static pressure distribution to be fairly flat. In addition, there is practically no circumferential variation in the static pressure. Another axial distribution of static pressure without burning is shown in Figure 39 for the case of an inlet Mach number of 0.58. If it is assumed that all the total pressure loss occurs at the igniter plane and the pressure recovery is then one-dimensional, pressure distributions for various recoveries may be computed; these are also shown in Figure 39. It is seen that a recovery between 0.900 and 0.915 just brackets the data and serves to indicate the average loss due to the dump diffusion process.

TOTAL PRESSURE

It was found that the pressure recovery was a function of the burner inlet Mach number, fuel-to-air ratio and circumferential location. The pressure recoveries at three circumferential stations (0° , 30° and 90°) at various fuel-air ratios are shown in Figures 40, 41, and 42 respectively. It may be seen that there is little or no change in the results due to variation in pressure level. The circumferential pressure recovery distributions are obtained from the foregoing charts and from other data at 45° , 75° , and 225° . At the design Mach number, this distribution is shown in Figure 43. Because of geometrical symmetry about the primary igniter centerline, it was assumed that the 0° data point could be reflected to $\theta = 60^\circ$. Note that reflecting the $\theta = 225^\circ$ data point to $\theta = 75^\circ$ shows fairly good agreement with the actual measurement taken. The effect of Mach number on the circumferential pressure distribution is shown in Figure 44 at a constant fuel-air

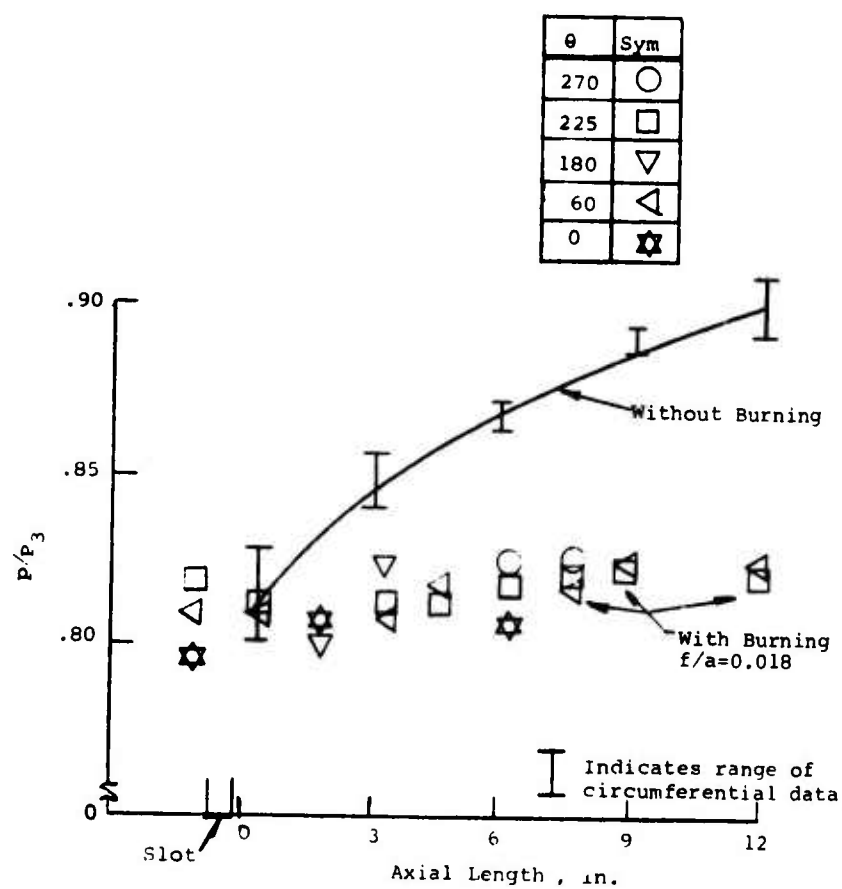


Figure 38. Axial Static Pressure Distribution With and Without Burning, $M_3=0.48$, $P_3=128$ psia.

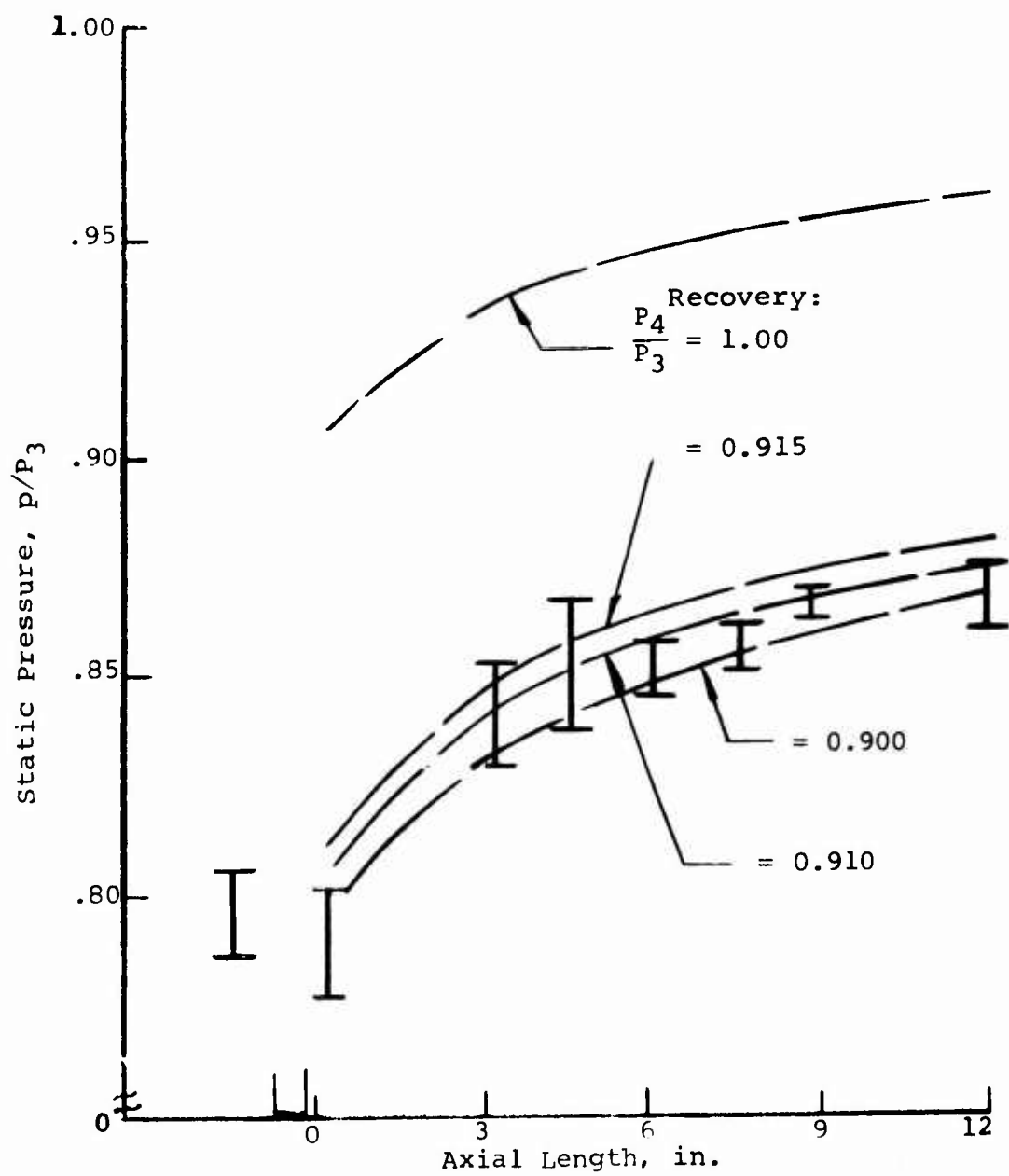


Figure 39. Axial Distribution of Static Pressure,
 $M = 0.58$, No Burning.

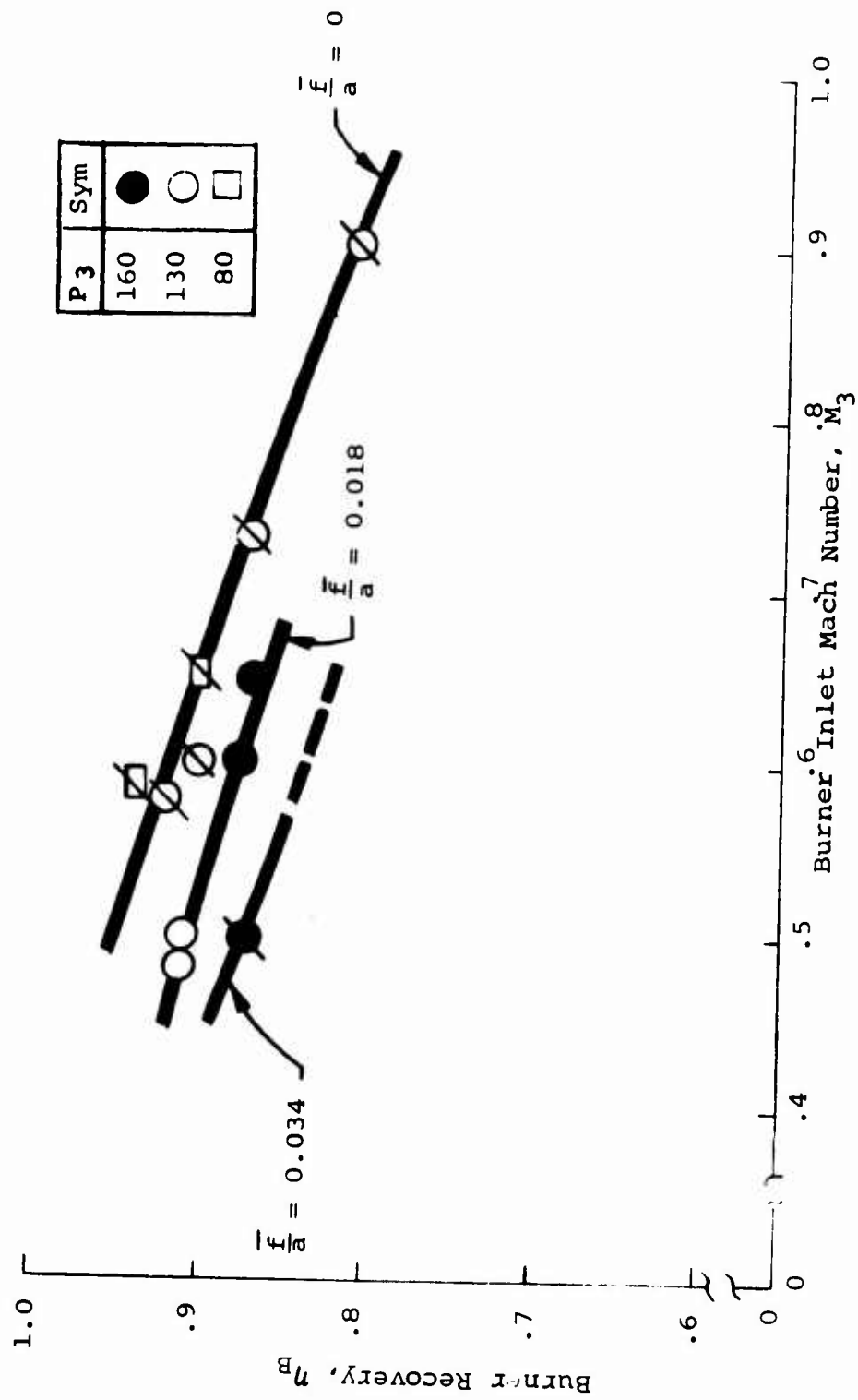


Figure 40. Burner Pressure Recovery vs Mach Number, $\theta=0^\circ$.

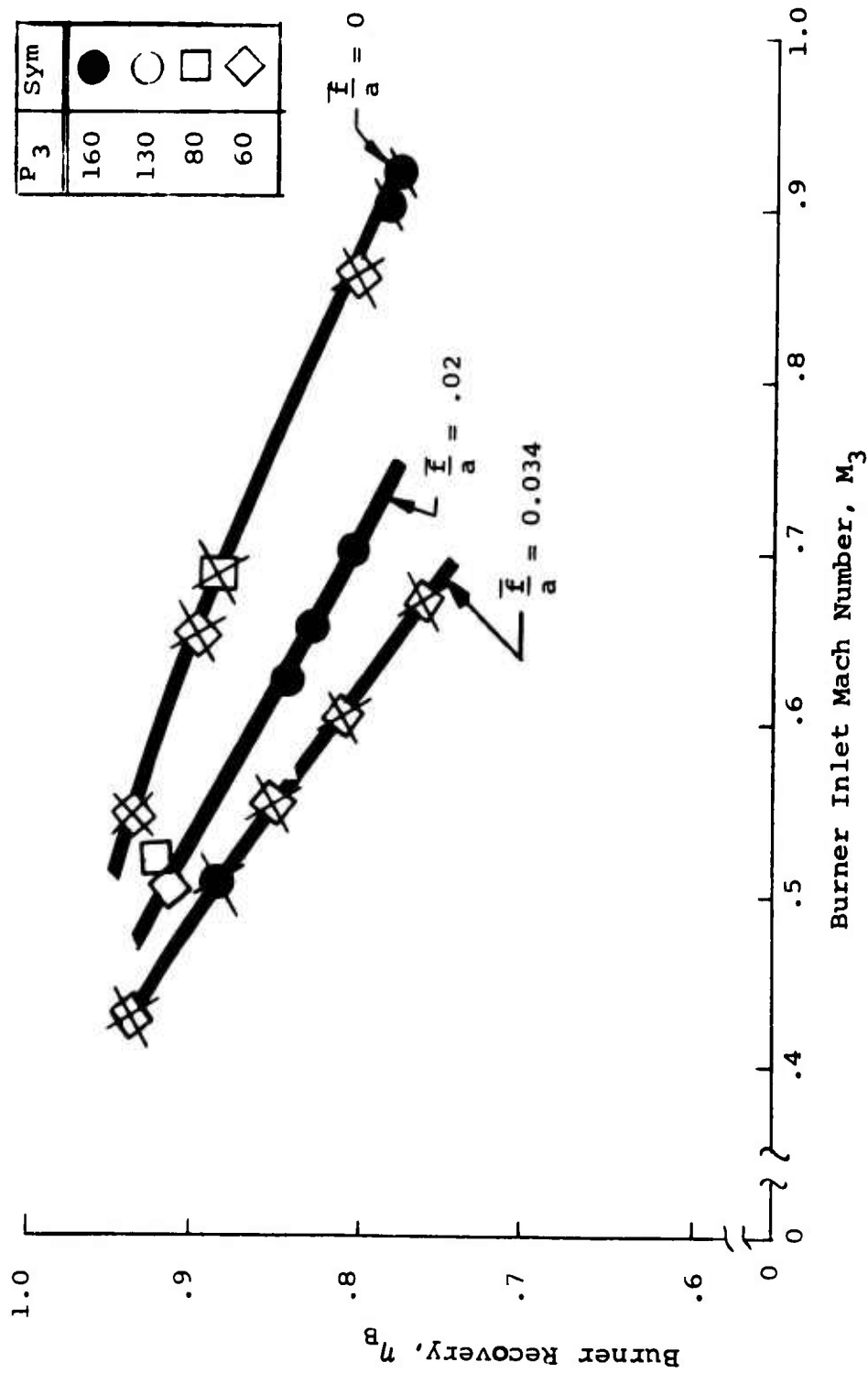


Figure 41. Burner Pressure Recovery vs Mach Number, $\theta = 30^\circ$.

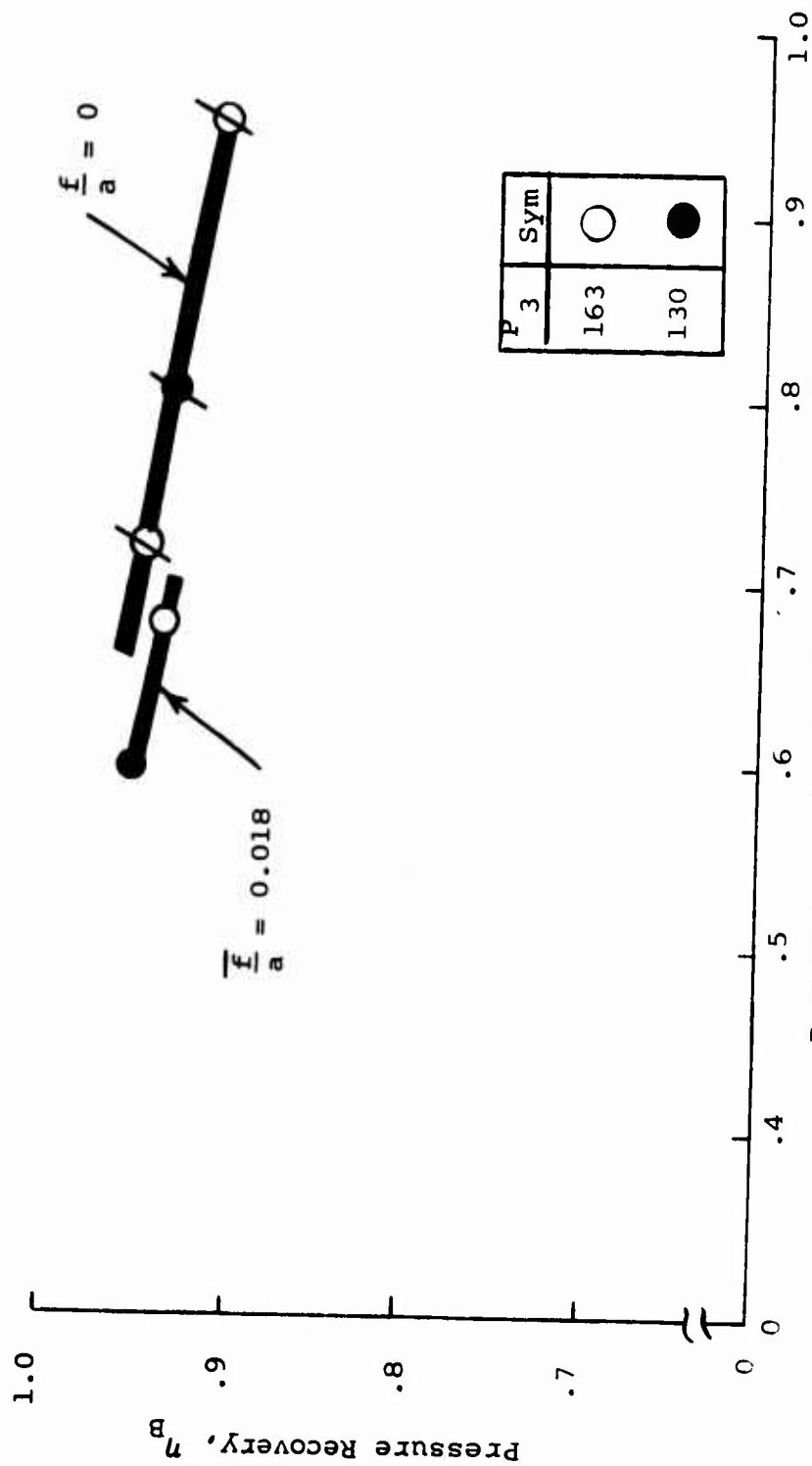


Figure 42. Burner Pressure Recovery vs Inlet Mach Number, $\theta=90^\circ$

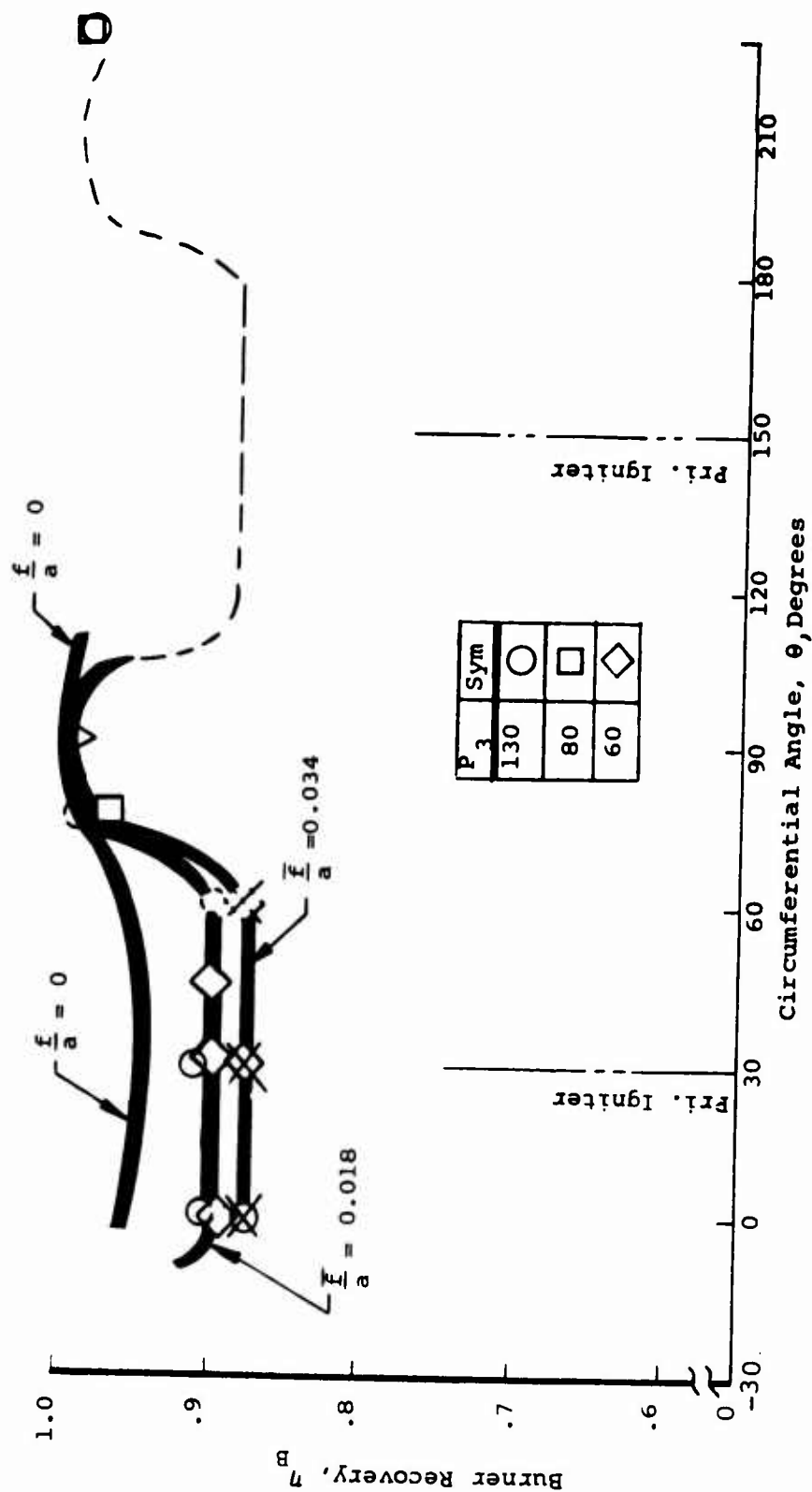


Figure 43. Circumferential Burner Pressure Recovery, $M_3 = 0.5$

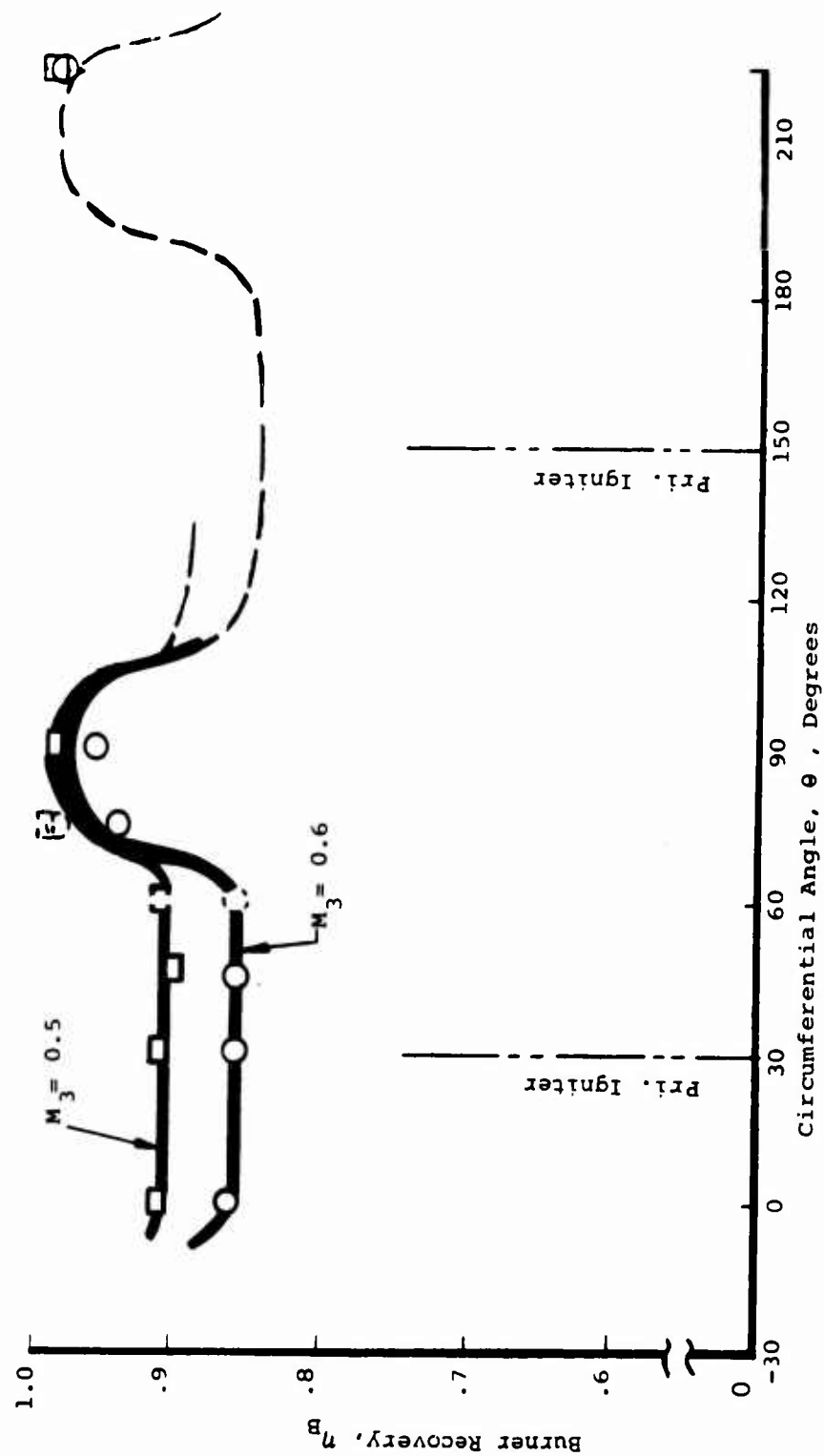


Figure 44. Effect of Burner Mach Number on Pressure Recovery, $f/a = 0.018$.

ratio of 0.018. It appears that the shape of the distribution is unchanged by the Mach number, and only the level of the recovery is reduced by increasing the Mach number.

COMPARISON OF EXPERIMENT AND THEORY

As the experimentally observed burner static pressure level was fairly constant during combustion, a comparison of burner recovery can be made between constant pressure theory and experiment. Figure 45 shows this comparison where the experimental data were all taken at the $\theta = 30^\circ$ station. It is seen that theory fairly well predicts the observed recovery especially at the lower values of fuel-air ratio. The agreement is particularly interesting since the theoretical recovery values do not include any pressure loss due to flow blockage caused by the primary igniters (Note the value of η_B at $f/a = 0$). A possible explanation for this mitigating effect is that, due to burning in the base region behind primary igniters, there is a reduction in the large dissipative, vortical flow usually associated with the process of dumped diffusion.

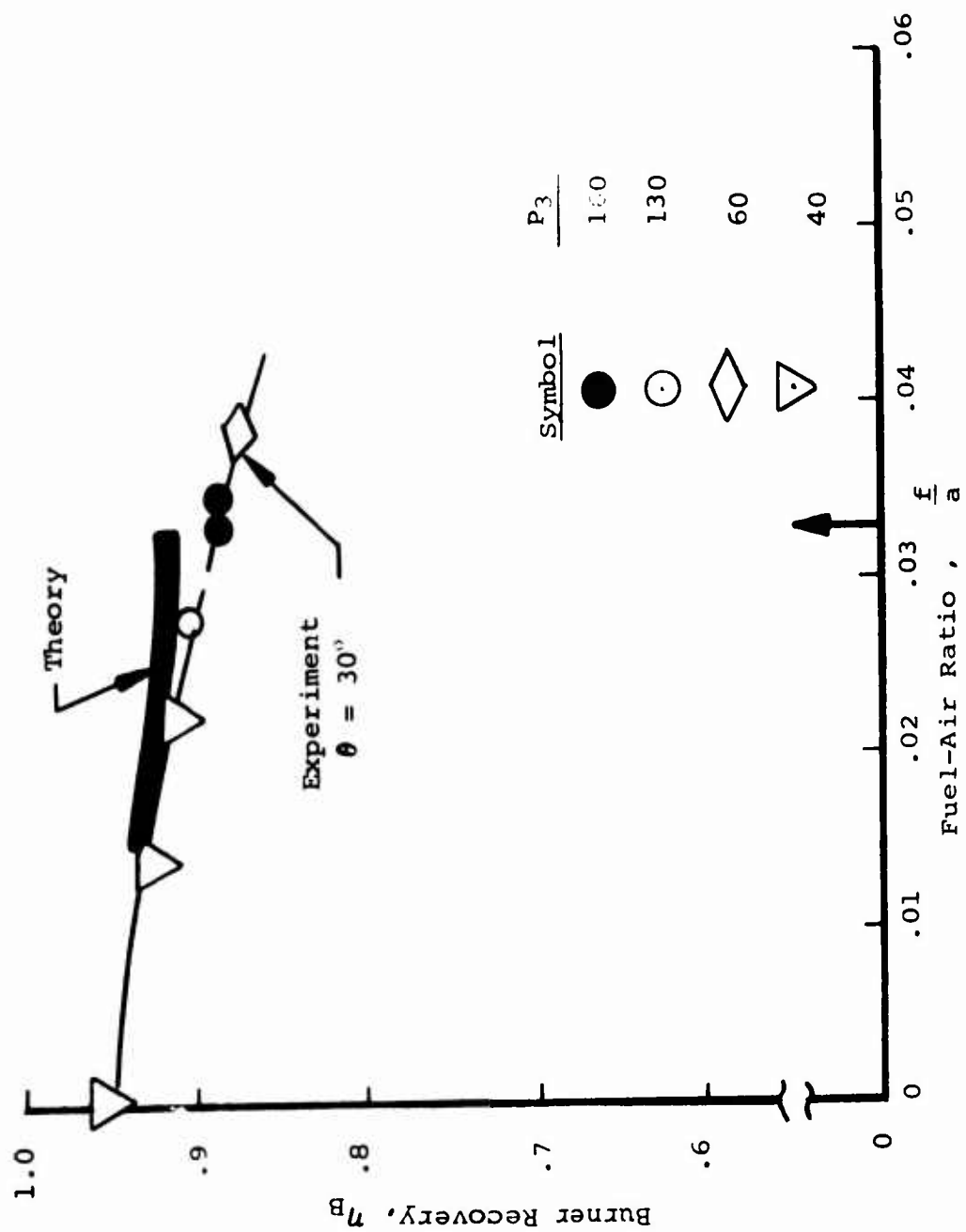


Figure 45. Comparison of Experiment With Theoretical Constant Pressure Burner Recovery, $M_3 = 0.5$.

VI. CONCLUSIONS AND RECOMMENDATIONS

CONCLUSIONS

From an analytical and experimental program studying the high-speed burner concept, the following items are deemed significant:

1. Consideration of the combined dump-diffuser and constant-pressure burner efficiencies indicate an optimum burner inlet Mach number equal to 0.5.
2. The GASL finite-rate combustion and turbulent mixing programs predicted the complete burning and mixing within the relatively short length of 1.1 ft for the specified geometry and fuel-air layer model.
3. Ignition and combustion of liquid JP-4 fuel were experimentally obtained over the range of operating conditions.
4. Combustion was manifest in the vicinity of the blunt-trailing-edge primary igniters, but not in the region between igniter stations. It appeared that the slot flameholder was ineffective, causing some 25 percent of the total fuel flow to remain unburned.
5. Comparison of experiment and recovery downstream of the primary igniters with predicted constant-pressure combustion recovery shows fairly good agreement.

RECOMMENDATIONS

It is believed that the reported experimental results prove the feasibility of the high-speed burner concept. However, it is clear that the present knowledge of the working of the slot flameholder is inadequate. Therefore, it is recommended that future effort be directed toward understanding the following flameholder phenomena:

1. blow-off stability limits
2. mechanism of flame initiation
3. effects of slot geometry

LITERATURE CITED

1. Johnsen, I.A., and Bullock, R.O., Editors, AERODYNAMIC DESIGN OF AXIAL-FLOW COMPRESSORS, NASA SP-36, NASA Cleveland, Ohio 1965.
2. Keenan, J.H., and Kaye, J., GAS TABLES, New York, John Wiley and Sons, 1948.
3. Fremont, et al., PROPERTIES OF COMBUSTION GASES SYSTEM: C_nH_{2n} -AIR, General Electric Co., Cincinnati, Ohio, 1955.
4. Ames Research Staff, EQUATIONS, TABLES AND CHARTS FOR COMPRESSIBLE FLOW, NACA TR 1135, 1953.
5. Henry, J., Wood, C.C., and Wilbur, S.W., SUMMARY OF SUB-SONIC-DIFFUSOR DATA, NACA RM L56F05, NACA, Hampton, Virginia, October 1956.
6. Henry, J., DESIGN OF POWER PLANT INSTALLATION PRESSURE LOSS CHARACTERISTICS OF DUCT COMPONENTS, NACA Wartime Report L 4F26, NACA, Hampton, Virginia, June 1944.
7. Runstadler, P.W., Jr., and Dean, R.C., Jr., STRAIGHT CHANNEL DIFFUSOR PERFORMANCE AT HIGH INLET MACH NUMBERS, Creare, Inc., Hanover, N. H., ASME Paper 68-WA/FE-19.
8. Lewis Research Laboratory Staff, BASIC CONSIDERATION IN THE COMBUSTION OF HYDROCARBON FUELS WITH AIR, NACA TR-1200, NASA, Cleveland, Ohio 1957.
9. Ingebo, R.D., PENETRATION OF DROPS INTO HIGH VELOCITY AIRSTREAMS, NASA TMX-1363, NASA, Cleveland, Ohio, April 1967.
10. Hoerner, S.F., FLUID DYNAMIC DRAG, Midland Park, N.J., S. F. Hoerner, Pub., August 1957.
11. Jakob, M., HEAT TRANSFER, Vol. I., New York, John Wiley and Sons, 1962.
12. Longwell, J.P., and Weiss, M.A., MIXING AND DISTRIBUTION OF LIQUIDS, Industrial and Engineering Chemistry, Vol. 45, No. 3, March 1953.

13. May, W.G., and Maddocks, F.E., MIT FUEL RESEARCH LABORATORY METEOR REPORT No. 54, MIT, Cambridge, Mass., April 1950.
14. Nicholson, H.M., and Field, J.P., THIRD SYMPOSIUM ON COMBUSTION FLAME AND EXPLOSION PHENOMENA, Baltimore, Md., The Williams and Wilkins Co., 1949, pp 44-68.
15. Surlock, A.C., MIT FUEL RESEARCH LABORATORY METEOR REPORT No. 19, MIT, Cambridge, Mass, July 1948.
16. DeZubay, E.A., CHARACTERISTICS OF DISC CONTROLLED FLAME, Aero Digest, Vol. 61, No. 1, July 1950, pp. 54-56; 102-104.
17. Weir, A., Rogers, D.E., and Cullen, R.E., UNIVERSITY OF MICHIGAN REPORT UMM-74, Willow Run Research Center, Willow Run, Michigan, September 1950.
18. Longwell, J.P., Chenevey, J.E., Clark, W.W., and Frost, E.E., THIRD SYMPOSIUM ON COMBUSTION, FLAME AND EXPLOSION PHENOMENA, Baltimore, Md., The Williams and Wilkins, Co., 1949, pp. 40-44.
19. Haddock, G.H., JET PROPULSION LABORATORY REPORT No. 3-24, California Institute of Technology, May 14, 1951.
20. Huellmantel, L.W., Ziemer, R.W., and Cambel, A.B., STABILIZATION OF PREMIXED PROPANE-AIR FLAMES IN RECESSED DUCTS, Jet Propulsion, Vol. 27, No. 1, January 1957.
21. Moretti, G., A NEW TECHNIQUE FOR THE NUMERICAL ANALYSIS OF NONEQUILIBRIUM FLOWS, AIAA J., Vol. 3, February, 1965, pp. 223-229.
22. Magnus, D., and Schechter, H., ANALYSIS OF ERROR GROWTH AND STABILITY FOR THE NUMERICAL INTEGRATION OF THE EQUATIONS OF CHEMICAL KINETICS, Report TR-607, General Applied Science Laboratories, Inc., Westbury, New York, June 1966.

23. Chinitz, W., and Baurer, T., AN ANALYSIS OF NON-EQUILIBRIUM HYDROCARBON-AIR COMBUSTION, 1965 Fall Meeting - Western States Section/ The Combustion Institute, Paper 65-19.
24. Nixon, A., et al., VAPORIZATION AND ENDOTHERMIC FUELS FOR ADVANCED ENGINE APPLICATION, APL-TDR-64-100, Parts II and III, and AFAPL-TR-67-114, Part I, Shell Development Co., 1964-1967.
25. Hawthorn, R., and Nixon, A., SHOCK TUBE IGNITION DELAY STUDIES OF ENDOTHERMIC FUELS, AIAA J., Vol. 4, March 1966, pp. 513-520.
26. Lee, K., Thring, M., and Beer, J., ON THE RATE OF COMBUSTION OF SOOT IN LAMINAR SOOT FLAME, Combustion and Flame, Vol. 6, 1962, pp. 137-145.
27. Zeiberg, S., and Bleich, G., FINITE-DIFFERENCE CALCULATION OF HYPERSONIC WAKES, AIAA J., Vol. 2, August 1964, pp. 1396-1402.
28. Edelman, R., DIFFUSION CONTROLLED COMBUSTION FOR SCRAMJET APPLICATIONS, (U), AIAA Second Prop. Joint Specialists' Conf., Colorado, June 1966 (Report Confidential).
29. Edelman, R., and Fortune, O., AN ANALYSIS OF MIXING AND COMBUSTION IN DUCTED FLOWS, AIAA 6th Aerospace Sci. Mtg., Paper 68-114, January 1968.

APPENDIX I
FLAME STABILIZATION AND IGNITION

In developing high-output combustors, it is necessary to stabilize the flame in a mixture of fuel and high-velocity air. This stabilization can be accomplished by placing a bluff object in the gas stream, and if conditions are chosen properly, a flame will be stabilized in the recirculation zone formed behind the bluff body.

A number of investigators have determined empirically the range of air-fuel ratios for which bluff bodies of various shapes and sizes will stabilize a flame as a function of mixture, velocity, pressure, and temperature. These experiments were somewhat idealized by using a vaporized and premixed fuel-air mixture. This is important because, as shown in Reference 13, flame stabilization is affected by the amount of liquid left in the vaporizing stream and drop size.

The nature of the flow in the recirculating zone of a flame stabilizer was illustrated by the work of Nicholson and Field (Reference 14). Small particles of sodium acetate were placed in the airstream. When one of these particles entered the flame zone, the resulting sodium vapor emitted light, which was recorded by high-speed motion pictures (1/5000 second). These motion pictures have shown very rapid mixing within the recirculating region, and it is generally felt that stabilization is accomplished by ignition of fresh mixture by mixing with the hot gases in the recirculating region. The hot combustion products leaving this zone cause ignition of the main body of fuel and air.

A quantitative understanding of combustion in this important eddy region would require much more detailed information on the heat balance, local combustion efficiencies, flow patterns, etc., than is now available. Nevertheless, several investigators, by making assumptions as to the mechanism of flame blowoff, have attempted to establish the groups of variables expected to control flame stabilization (References 14, 15, and 16). These analyses generally arrive at the conclusion that the mixture ratio at blowoff is a function of $v/p^{ad}bT^C$, where v is the velocity past the bluff

body, P is the absolute pressure, D is a characteristic dimension of the stabilizer, and T is the mixture absolute temperature. Figure 46 shows a typical correlation as published by DeZubay (Reference 16), showing the effect of body diameter, pressure and mixture velocity. The gas velocity varied from 40 to 550 ft/sec, the disc diameter varied from 1/4 in. to 1 in., and P , the absolute pressure, varied from 3 to 15 psia. The gas was a propane-air mixture initially at room temperature. The fuel-air ratio at blowoff is plotted as a function of the dimensional group $V/P^{.95}D^{.85}$, where D is the diameter of the circular flat disc used to stabilize the flame. It is seen that larger bodies, higher pressures, and lower velocities give wider stability limits and that a maximum value of the above group for stable operation exists in the region of stoichiometric.

In the work of Reference 17, the effect of pressure was studied and was also found to have an approximately inverse dependence in the stability criterion. This pressure effect is of great importance for the application of interest here. Flammability limits and laminar burning velocity have been found to be less significant, while spark ignition energy may have a larger effect. Similar correlations of the effect of diameter and velocity have been published by other investigators (References 15, 18, 19). There is considerable variation in the exponent of D (.45 to 1.00) and it is believed that these differences are too large to be attributed to experimental errors. Table VI summarizes the work done by several investigators. The first two arrived at an exponent of 1.00 and .86 using cones or flat discs. The next two, using rods mounted with their axes 90° to the direction of flow, found that an exponent of .5 best fitted their data. It is apparent from these data that the correlation of blowoff as a function of D^2 is not completely satisfactory. It would appear that a more accurate study of flameholders along with more knowledge of the aerodynamics as a function of velocity, shape, and heat release is needed.

The effect of temperature has been investigated in References 18 and 19. An exponent of 1.2 on the absolute temperature T best correlated the data.

TABLE VI. SUMMARY OF BLUNT-TRAILING-EDGE FLAMEHOLDER WORK				
Investigator	Correlating Group	Type of Flameholder*	Mixture Velocity Range (ft/sec)	Approach Temp. (°R) Fuel
Longwell, Chenevey, Clark, and Frost. Ref. 18	V/D	Cylinders (axis parallel to flow), cones, annuli, and V-gutters uncooled	200 to 950 past flameholder	760 Naptha
DeZubay Ref. 16	V/D ^{.86}	Disks and washers (perpendicular to flow) uncooled	40 to 550 past flameholder	550 propane
Surlock Ref. 15	V/D ^{.5}	Cylinders and gutters (axis perpendicular to flow) uncooled	60 to 310	540-610 City Gas and Propane
Haddock Ref. 19	V/D ^{.5}	Cylinders (axis perpendicular to flow) cooled	60 to 740	610 Hydrocarbon Blend (C ₆ C ₈)
* For annuli, D is the difference between outer and inner radii; for rods or V-gutters, D is the width measured perpendicular to the axis of gutter.				

Shown in Figure 46 are experimental data points for the slot type of flameholder which was computed from the data of Reference 20. It is seen that the loading parameter $v/p \cdot 95 D^{.85}$ collapses the data points and that at least for lean fuel-air mixtures the points lie on the DeZubay line. Rich mixtures fall above the line and indicate that a slot generates a more stable flameholder than a bluff body here.

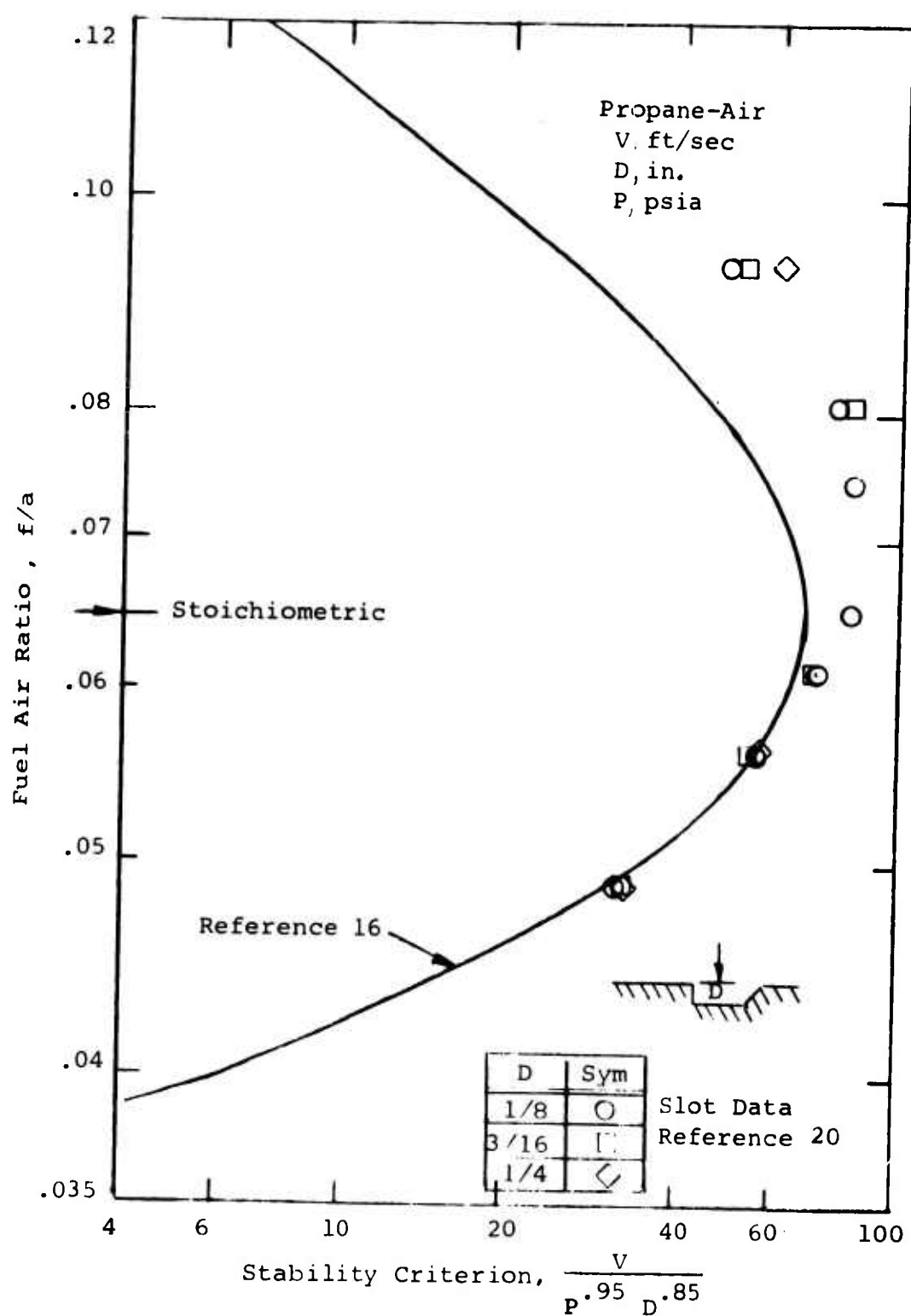


Figure 46. Flameholder Stability Limits.

APPENDIX II

REVIEW OF MIXING ANALYSIS

The rate at which fuel is transported radially by turbulent eddy diffusion depends on the time-averaged fuel concentration gradients and on the eddy diffusivity of mass, characterized by the turbulent diffusion coefficient D_T (ft²/sec). For axially symmetric flows, the turbulent diffusion equation may be written as:

$$\rho v \frac{\partial y}{\partial r} + \rho u \frac{\partial y}{\partial x} = \frac{1}{r} \frac{\partial}{\partial r} \left[\rho D_T r \frac{\partial y}{\partial r} \right] \quad (70)$$

where

y = local mass fraction of fuel = $f/f+a \approx f/a$

ρ = total density of mixture

v = radial velocity component

u = axial velocity component

r = radial distance

x = axial distance

In writing this equation, it was assumed that diffusion in the axial direction is small compared to convective bulk flow. Equation (70) may be rewritten in the form

$$\rho \left(v \frac{\partial y}{\partial r} + u \frac{\partial y}{\partial x} \right) = \rho D_T \left(\frac{1}{r} \frac{\partial y}{\partial r} + \frac{\partial^2 y}{\partial r^2} \right) + \frac{\partial y}{\partial r} \frac{\partial}{\partial r} (\rho D_T) \quad (71)$$

It is convenient (although not accurate) to assume that D_T is only a function of x or even constant in a given airstream. In addition, if compressibility effects are neglected and the radial velocity is very small, then Equation (71) becomes

$$\frac{\partial y}{\partial x} = \frac{D_T}{v} \left[\frac{\partial^2 y}{\partial r^2} + \frac{1}{r} \frac{\partial y}{\partial r} \right] \quad (72)$$

The solution to Equation (72) may be obtained by using standard Fourier transform techniques and is a function of the boundary and initial conditions. The solutions for three common injector configurations are shown in Table VII taken from Reference 12.

TABLE VII. SOLUTIONS TO THE DIFFUSION EQUATION	
Type of Fuel Injector	Solution
Point Source	$\frac{f}{a} = \frac{\dot{m}_f}{4\pi M_a} \frac{v}{D_T x} \exp \left[-\frac{v r^2}{4D_T x} \right] \quad (73)$
Disk Source (of Radius R)	$\frac{f}{a} = \frac{\dot{m}_f}{M_a R^2} \psi(r, x) \quad (74)$
Ring Source (Ring Radius R)	$\frac{f}{a} = \frac{\dot{m}_f}{M_a R^2} \varphi(r, x) \quad (75)$
where	
$M_a = \text{mass flux of air lb/sec, ft}^2$	
$\varphi = \frac{1}{\pi} K I_0 \left(2K \frac{r}{R} \right) \exp \left[-K \left(1 + \frac{r^2}{R^2} \right) \right] \quad (76)$	
$K = \frac{v R^2}{4D_T x} \quad (77)$	
$\psi = \frac{1}{2\pi D_T x R^2} \exp \frac{(-v R^2)}{4D_T x} \int_0^R r' \exp \frac{(-v r'^2)}{4D_T x} I_0 \frac{(v R r')}{2D_T x} dr' \quad (78)$	

I_0 is the modified Bessel function of the first kind, zero order. Both φ and ψ are plotted in Reference 12 over a range of flow conditions.

Since the governing diffusion equation is linear, the fuel-air distributions resulting from multi-source injections can be expressed by summaries of the individual source equations. This means that the fuel in a volume of air is a summation of the fuel contributed by each injection source acting as though it were the only source present. Therefore, we may write that

$$\frac{f}{a} = \sum_i (f/a)_i \quad (79)$$

The solutions described to this point are subject to the limitation of infinite duct size. Presence of a wall implies a boundary condition of the type

$$\left(\frac{\partial f/a}{\partial r} \right)_{r=r_w} = 0 \quad (80)$$

and consequently the general solution is no longer valid.

For a single point source or disk source located axially in a finite duct, these are available solutions for the fuel distribution. Thus for a point source injecting into a finite duct, Reference 12 gives the following expression:

$$\frac{\frac{f}{a}}{\left(\frac{f}{a}\right)_0} = 1 + \sum_{n=1}^{\infty} \frac{J_0(\alpha_n \frac{r}{\bar{R}})}{J_0^2} \exp \left[\frac{-D_T \alpha_n^2}{v \bar{R}} \right] \quad (81)$$

where

$(f/a)_0$ = after mixing fuel-air ratio

J_0 = Bessel function, zero order

\bar{R} = duct radius

α_n = roots of J_1 first-order Bessel function

Similar expressions can be derived for non-point and non-axial fuel injectors, but the resulting equations become very complex. Therefore, for the present combustion design, it was decided to use a graphical technique developed by Longwell and Weiss and shown to be a good approximation

in Reference 12. This graphical technique is based on the assumption that fuel diffuses from the wall as a mirror reflection of the fuel which would have diffused beyond the wall if the wall had not been there.

Turbulent Transport Properties

Predicting the fuel distribution accurately depends upon the utilization of the correct values for the turbulent transport coefficient. The terms D_T and v which appear in the diffusion equation as the ratio D_T/v may be reckoned as a diffusion parameter which has the dimension of length. Since the diffusivity D_T is proportional to the turbulent intensity of the airstream, one would expect D_T to vary directly with the flow velocity so that the ratio D_T/v should be constant.

Longwell and Weiss experimentally determined and showed in Reference 12 the variation of D_T/v as a function of v for a very volatile liquid-naptha and for the diesel fuel. Because of the presence of the liquid droplets, it was found that the value of D_T/v dropped off with increasing v . However, the value for naptha approached a constant ($D_T/v \approx .001$) beyond $v = 400$ ft/sec, since it was almost completely evaporated. Extrapolating the diesel fuel (kerosene) value to the air velocity of the present burner, 800 ft/sec, gives a value of $D_T/v = .0004$ ft.

APPENDIX III

REVIEW OF FINITE-RATE CHEMICAL KINETICS

For an analytic description of high-speed combustion problems, it is generally not adequate to assume equilibrium burning, since the time for the combustion process is too short. Hence, it is necessary to formulate and employ a finite-rate chemical kinetic combustion mechanism for the chemical system of interest.

Work at GASL, as described in Reference 21, resulted in the formulation of a finite-rate chemical kinetic model whose numerical solution technique was, without significant loss in accuracy, at least two orders of magnitude faster than standard techniques such as Runge-Kutta. The numerical solution technique of Reference 21 was improved upon in Reference 22, which (besides decreasing numerical solution time even more) made it practical to perform finite-rate chemical calculations for more complex systems, such as the burning of a hydrocarbon-air mixture.

One very important family of hydrocarbons is the paraffins (C_nH_{2n+2}). Work was done at GASL, as reported in Reference 23, to formulate a detailed chemical kinetic model for the oxidation of the paraffin propane. This was done because the oxidation processes inherent in the propane system are quite similar to heavier paraffins. As borne out by experimental results, the ignition delay and reaction times of paraffins even heavier than kerosene ($C_{10}H_{22}$) are within an order of magnitude of those for propane. The analysis employed 31 chemical species participating in 69 elementary reactions. This detailed model was employed in one-dimensional stream tube type calculations over a wide range of pressures, temperatures, and equivalence ratios. Results were compared with data from both shock tube and steady flow facilities (References 24 and 25). In general, the computed ignition delay times were well within the order of magnitude of the experimental data.

However, because this reaction mechanism for the hydrocarbon fuel system is extremely complex, it was found to be too expensive for use in flow-field calculations. In addition,

the lack of well-defined rate constants for many of the intermediate reactions justifies seeking smaller, yet representative, chemical systems for the combustion of kerosene. Therefore, the detailed kinetic model was used to formulate a relatively simple "quasi-global" kinetic model that would be appropriate for both fuel lean and fuel rich paraffin-air mixtures. It was desired to predict both ignition delay times and total reaction times to within an order of magnitude. The use of a "quasi-global" model with less than a dozen chemical species makes it economically feasible to perform multidimensional flow-field calculations.

The species employed in the quasi-global model are the paraffin C_nH_{2n+2} and the equilibrium combustion products: H_2 , O_2 , H_2O , CO_2 , CO , H , O , OH . In addition, N_2 is present as a diluent, and solid carbon (graphite) may also be considered to be present in rich mixtures. The reaction mechanism is comprised of the nine intermediate reactions shown in Table VIII.

The production rate of species i , in moles/cc/sec, is given by

$$\frac{dc_i}{d\tau} = \sum_{r=1}^{18} (\nu''_{i,r} - \nu'_{i,r}) k_r \prod_{j=1}^9 (C_j)^{\nu'_{j,r}} \quad (82)$$

for the reaction



where C_j is the molar concentration of the j^{th} species, ν_i is the stoichiometric coefficient i associated with the R_i species and k_r is either the forward or the reverse reaction rate constant. The above system has been solved by the linearization technique described in Reference 21. This technique involves the expansion of the product term in Equation (82) in Taylor's series and truncating to the lowest order term.

TABLE VIII. REACTION MECHANISM

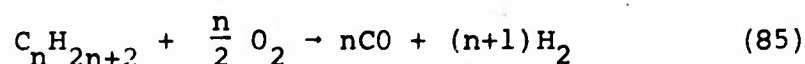
Reaction No.	Reaction	k_{f_i}	k_{b_i}
1	$\text{CO} + \text{OH} \xrightleftharpoons[k_{b1}]{k_{f1}} \text{CO}_2 + \text{H}$	$3.2 \times 10^{12} e^{(-3.1706/t)}$	$2.7 \times 10^{17} e^{-0.79} (-15.45/t)$
2	$\text{OH} + \text{H}_2 \xrightleftharpoons[k_{b2}]{k_{f2}} \text{H} + \text{H}_2\text{O}$	$6.3 \times 10^{13} e^{(-2.9693/t)}$	$2.4 \times 10^{14} e^{(-10.413/t)}$
3	$\text{OH} + \text{OH} \xrightleftharpoons[k_{b3}]{k_{f3}} \text{H}_2\text{O} + \text{O}$	$7.6 \times 10^{12} e^{(-.50327/t)}$	$6.9 \times 10^{13} e^{(-8.928/t)}$
4	$\text{O} + \text{H}_2 \xrightleftharpoons[k_{b4}]{k_{f4}} \text{OH} + \text{H}$	$3.3 \times 10^{12} e^{(-3.5934/t)}$	$1.4 \times 10^{12} e^{(-2.612/t)}$
5	$\text{H} + \text{O}_2 \xrightleftharpoons[k_{b5}]{k_{f5}} \text{OH} + \text{O}$	$2.4 \times 10^{14} e^{(-8.4298/t)}$	$3.2 \times 10^{11} e^{0.47} (-.05032/t)$
6	$\text{O} + \text{H} + \text{M} \xrightleftharpoons[k_{b6}]{k_{f6}} \text{OH} + \text{M}$	3×10^{14}	$7.5 \times 10^{14} e^{0.06} (-50.976/t)$
7	$\text{O} + \text{O} + \text{M} \xrightleftharpoons[k_{b7}]{k_{f7}} \text{O}_2 + \text{M}$	2.2×10^{13}	$2.5 \times 10^{16} e^{-0.5} (-59.336/t)$
8	$\text{H} + \text{H} + \text{M} \xrightleftharpoons[k_{b8}]{k_{f8}} \text{H}_2 + \text{M}$	$2 \times 10^{18} e^{-1}$	$2.4 \times 10^{19} e^{-0.86} (-51.958/t)$
9	$\text{H} + \text{OH} + \text{M} \xrightleftharpoons[k_{b9}]{k_{f9}} \text{H}_2\text{O} + \text{M}$	$2.3 \times 10^{21} e^{-1.5}$	$1.2 \times 10^{23} e^{-1.34} (-59.3996/t)$

The reaction rate constants are expressed in the standard Arrhenius form given by

$$k_r(t) = A t^{\alpha_r} \exp \left(- \frac{\beta_r}{t} \right) \quad (84)$$

where A , α_r and β_r are the constants given in Table VIII. The species enthalpy-temperature data have been curve fitted from the data in the JANAF Tables.

The quasi-global reaction was written as



This was combined with the above nine elementary reactions for the interaction of the more stable combustion products. The quasi-global fuel oxidation reaction rate is of the form

$$- \frac{dC_{C_n H_{2n+2}}}{d\tau} = k f(t) p^{\alpha'} C_{C_n H_{2n+2}}^{\beta'} C_{O_2}^{\gamma'} e^{-\frac{E}{RT}} \quad (86)$$

The activation energy E was based on experimental data and was determined to be 13,740 cal/mole. β' was set equal to 1/2 and γ' equal to 1. Comparisons with the detailed kinetic model for different temperature pressures, and equivalence ratios were used to determine the values of k , $f(t)$, and α' . The resulting fuel burning rate is

$$- \frac{dC_{C_n H_{2n+2}}}{d\tau} = 2 \cdot 10^8 \left[\frac{t(^{\circ}K)}{1111} - .5 \right] \left[p(\text{atm}) \right]^{.3} C_{C_n H_{2n+2}}^{\beta'} C_{O_2}^{\gamma'} e^{-\frac{13,740}{Rt}} \quad (87)$$

The applicable temperature range of the above quasi-global model and the nine elementary reactions used in conjunction with it is in the region of 800° to 3000°K. Comparison of the quasi-global model with the detailed kinetics model of Reference 23, and with experiments for ignition delay and

reaction times, results in agreement to within an order of magnitude.

Previous work at GASL (References 27, 28 and 29) resulted in the formulation of a numerical finite difference technique for the solution of multi-dimensional turbulent mixing problems employing the boundary layer equations for the general case of arbitrary Prandtl and Lewis numbers and axial pressure gradient. Semi-empirical eddy transport coefficients have been used, based on experimental results, such as the work presented in Reference 28.

The mixing analyses coupled to the finite rate chemical system have been used to analyze axisymmetric and plane two-dimensional hypersonic wakes (Reference 27), free jets (Reference 28), and ducted configurations (Reference 29).

The combination of the quasi-global chemical model coupled to the finite-difference mixing analysis is the analytical tool used for designing the present high-speed combustion chamber.

APPENDIX IV HEAT TRANSFER ANALYSIS

A heating analysis is made of the subject combustor, and a number of thermal protection schemes are evaluated. The heat flux is calculated by

$$q_{\text{conv}} = \frac{.023}{(Y_F)^{.2}} \left[\frac{c_p \mu^{.2}}{N_{\text{Pr}}^{2/3}} \right]_4 (\rho V)^{.8} (T_4 - T_w) \quad (88)$$

The results are plotted in Figure 47 which shows the effect of combustion gas temperature on heat flux with wall temperature as parameters. Note that with combustion temperatures of 3000°R, the heat flux varies from 300 BTU/sec-ft² for a cold wall (60°F) down to 130 BTU/sec-ft² for a wall at 2000°R.

Air, fuel, and heat-sink cooling methods were evaluated, and comparisons were made to determine the technique that is most advantageous for this application.

Air Cooling

Air-cooling requirements were calculated using a heat transfer equation similar to that presented above, and the results are presented in Figure 48. Here, the effect of heat flux on coolant-side wall temperature is shown with coolant air velocity as a parameter. An anticipated requirement might be to use a coolant air velocity of 80 ft/sec at 150 psia to maintain the coolant-side wall temperature at 1600°F while subjected to a heat flux of 130 BTU/sec-ft². The coolant airflow rate would then be 2.6 lbm/sec for a 1/8 inch annulus circumscribing a 6-inch diameter. Air cooling for the centerbody would have similar flow requirements. Maximum bulk heating of the coolant air would be of the order of 200° to 300°F.

Fuel Cooling

Fuel-cooling requirements were calculated using

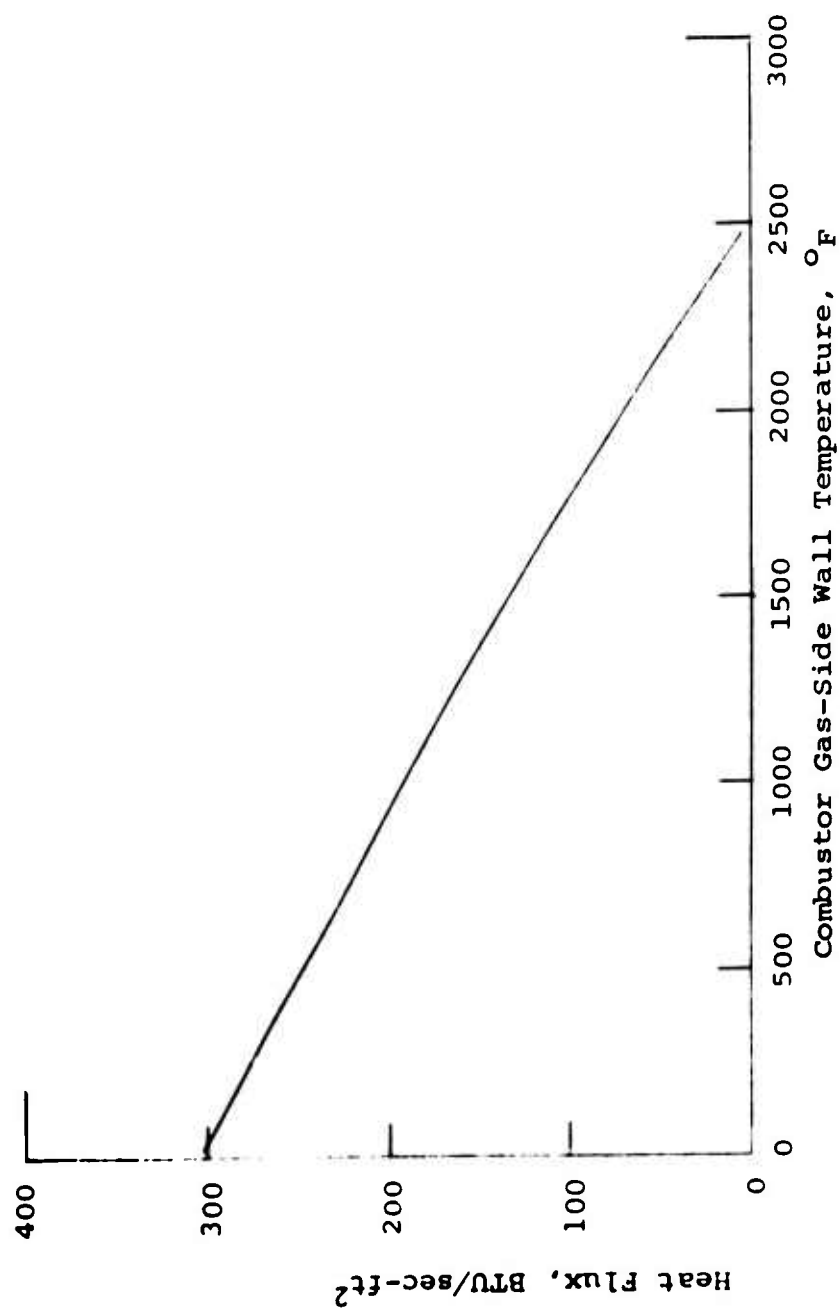


Figure 47. Effect of Wall Temperature on Heat Flux.

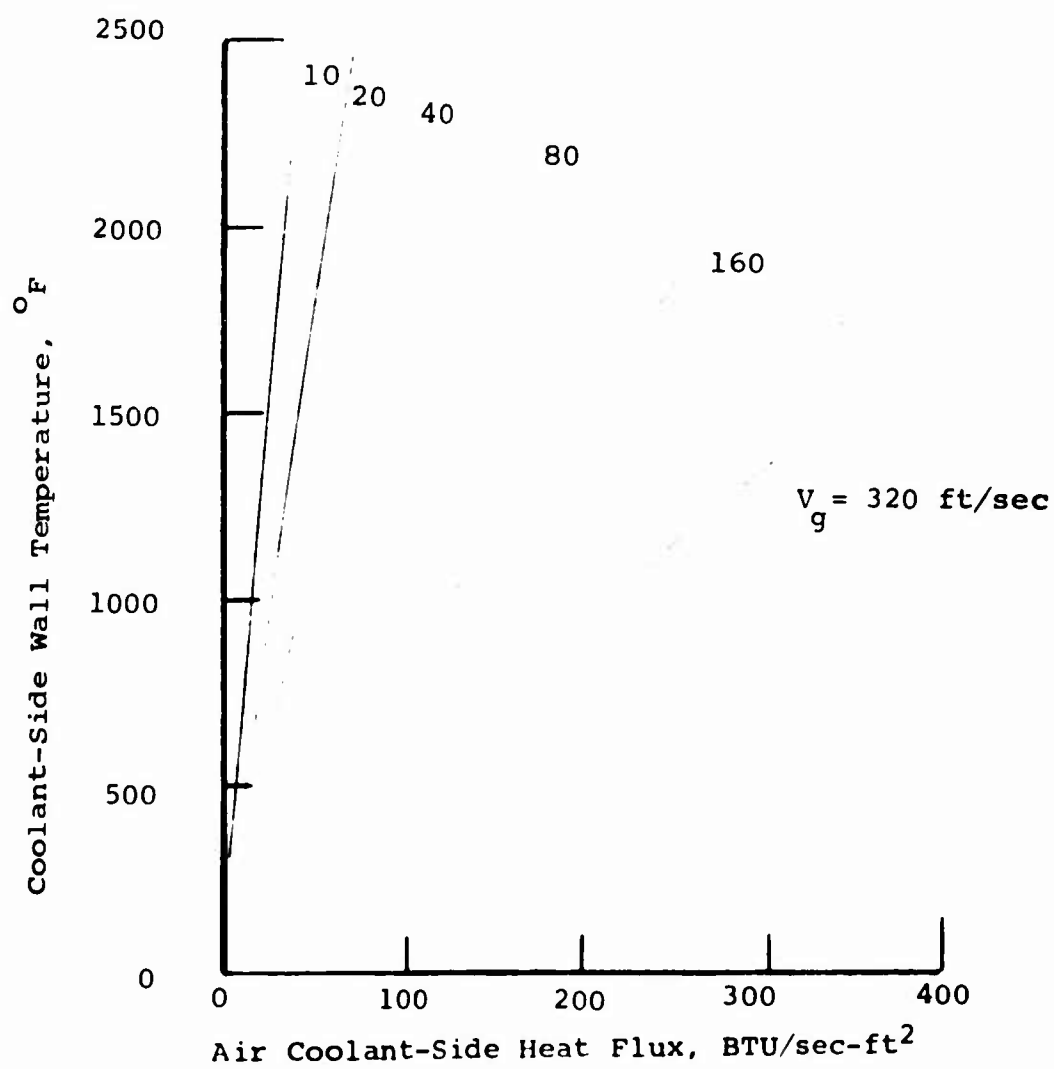


Figure 48. Effect of Heat Flux on Coolant-Side Wall Temperature.

$$q_{\text{conv}} = .027 (\rho V)_g^{.8} (T_w - T_g) \left(\frac{k \text{Pr}}{\mu^{.8}} \right)_g \left(\frac{\mu}{\mu_w} \right)_g^{1.4} \quad (89)$$

and liquid JP-4 as the coolant. Figure 49 shows the effect of heat flux on coolant fuel-side temperatures with fuel velocity as a parameter. A total fuel flow of approximately 0.2 lb/sec corresponds to airflow of 5 lb/sec and has only 10 percent of the heat capacity required to cool the entire combustor. Fuel cooling, therefore, can be used for cooling specific local areas but not the entire center-body or outer liner surface areas.

Heat-Sink Cooling

Heat-sink cooling characteristics were determined by using Schneider charts representing analytical solutions for transient, one-dimensional heat conduction in single-layer plates with constant ambient temperature and with finite internal and surface conductance. Figure 50 shows the temperature response of the combustor walls with complete combustion as a function of time with wall thickness as a parameter. Figure 51 shows the effect of heat flux on wall temperature for a test duration of 60 seconds with wall thickness as a parameter.

It can be observed from these figures that heat-sink cooling subjects the walls to temperature response throughout the entire test run and to very high metal temperature exposure during the latter part of a test run; however, this technique is preferred on the basis of: (1) achieving minimum required wall temperature within a few seconds, (2) simplicity, and (3) lowest cost.

Structural Considerations

Thermal stress resulting from temperature differentials across the combustor liner walls may be determined approximately by

$$S_t = \frac{E \delta \Delta T}{2(1-\beta)} \quad (90)$$

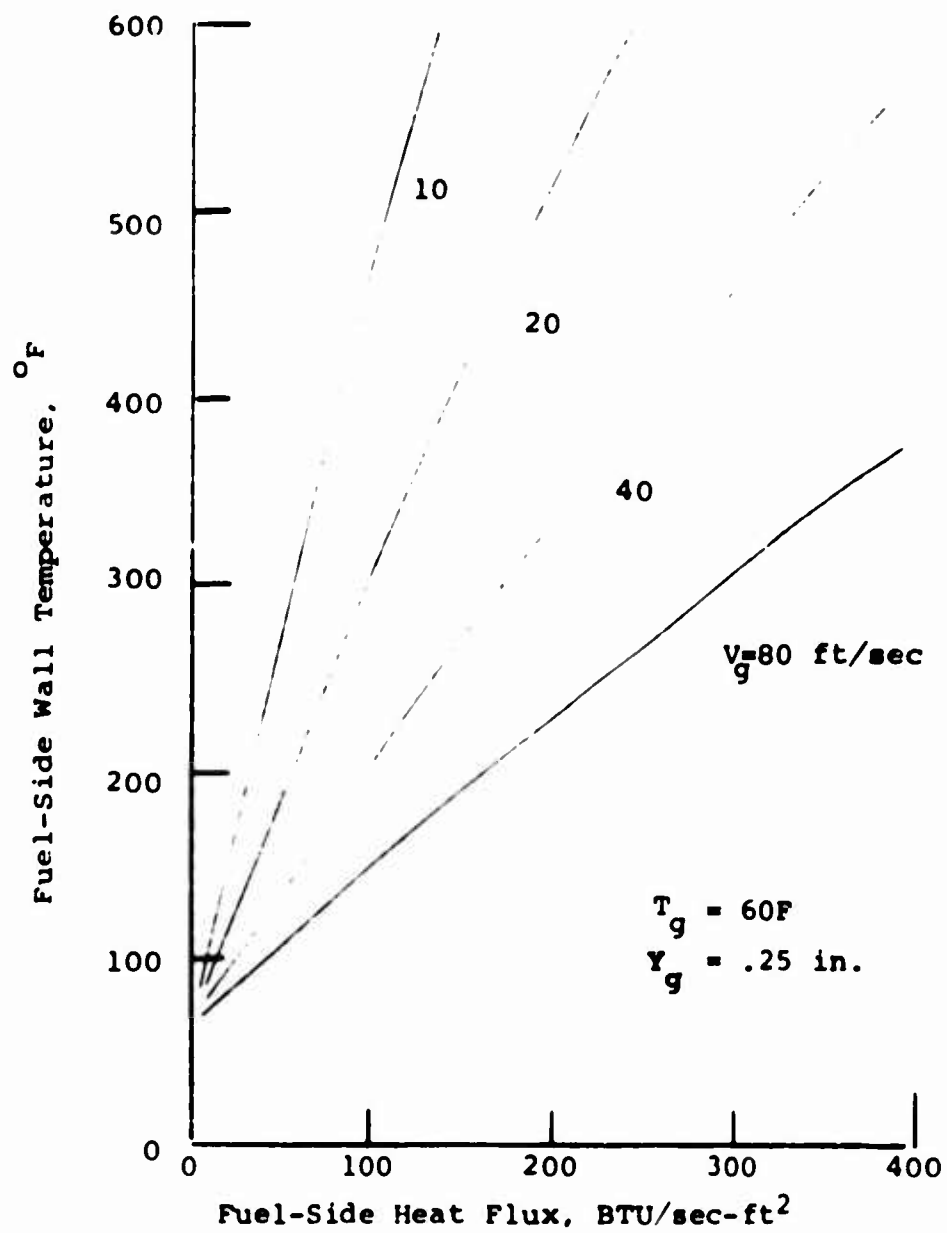


Figure 49. Effect of Heat Flux on JP-4 Coolant Fuel-Side Wall Temperature.

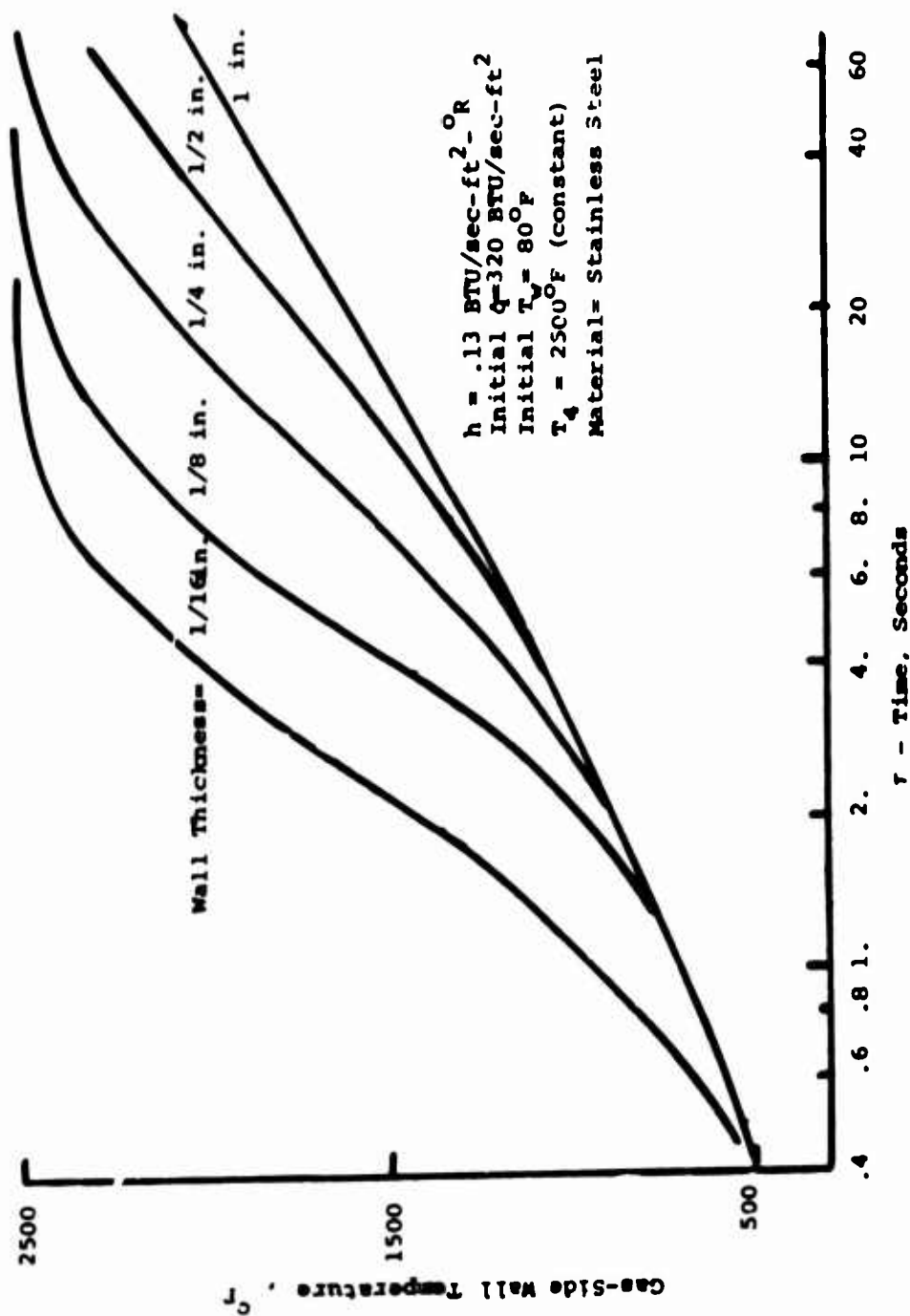


Figure 50. Temperature of Combustor Wall

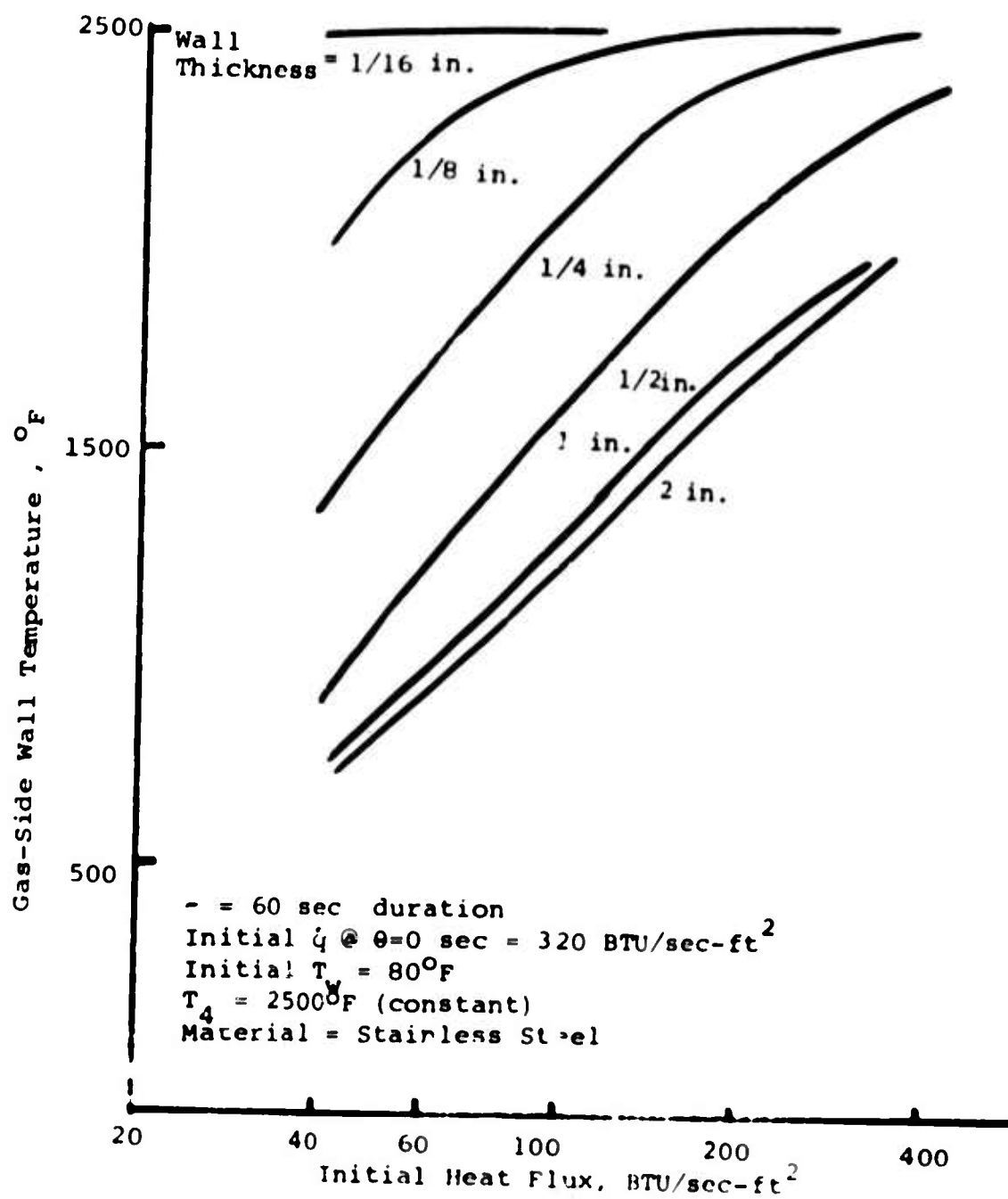


Figure 51. Effect of Heat Flux on Wall Temperature, τ = 60 seconds.

where

E = the modulus of elasticity

δ = coefficient of thermal expansion

ΔT = the temperature differential

β = Poisson's ratio

Thin-walled tube-type wall structures minimize thermal stresses; however, a practical shell-type wall thickness is 1/4 inch. An air-cooled stainless steel wall of this thickness, when subjected to the 2500°F ambient temperature gas with corresponding fuel flux of 130 BTU/sec-ft² and wall temperature differential of 800°F, sustains thermal stress amplitudes of 140,000 psi.

For a stainless steel heat sink-type wall liner with 1 inch wall thickness, maximum wall temperature differentials are of the order of 1400°F. This results in local stress amplitudes of 240,000 psi. Since actual compressive stresses will not exceed the yield point because of thermal strain, cyclic-strain analysis will indicate the approximate number of test cycles to failure. Cycles to failure are expressed as

$$N_F = \left[\frac{EC}{2(\sigma_a - \sigma_e)} \right]^2 \quad (91)$$

where

σ_a = the stress amplitude

σ_e = the endurance limit

$$C = 1/2 \log \frac{100}{100 - R_z}$$

R_a = the area reduction, percent

APPENDIX V
THERMOCOUPLE-PROBE CORRECTION

An analysis is made of the radiation and conduction errors associated with the platinum thermocouple probes used in the exit-plane instrumentation rake. Assuming the thermocouple bead to be a hemisphere, a summation of heat fluxes can be written as

$$q_{\text{conv}} + q_{\text{rad}} + q_{\text{cond}} = 0 \quad (92)$$

where

$$\begin{aligned} q_{\text{conv}} &= \text{convective heating flux} \\ q_{\text{rad}} &= \text{radiation heat loss} \\ q_{\text{cond}} &= \text{conductive heat loss} \end{aligned}$$

For a hemisphere with fluid properties taken at burner design conditions, the Nusselt number is $N_{\text{Nu}}=100$. Taking the surface area of the bead as $A=17.5 \cdot 10^{-6}\text{ft}^2$, the convective flux can be written as

$$q_{\text{conv}} = hA[T_4 - T_w] = 0.193 \cdot 17.5 \cdot 10^{-6}[T_4 - T_w] \quad (93)$$

where

$$\begin{aligned} T_4 &= \text{gas temperature} \\ T_w &= \text{wall temperature} \end{aligned}$$

The radiation heat flux can be described by

$$q_{\text{rad}} = \sigma A \epsilon T_w^4 \quad (94)$$

where the back radiation is ignored and

$$\begin{aligned} \sigma &= \text{Stephan-Boltzmann constant} \\ \epsilon &= \text{emissivity} = 0.018 \end{aligned}$$

Finally, the conduction is estimated by assuming the lead wire to be infinitely long and computing this heating rate as a function of time. From Reference 11, the flux at the interface between lead wire and bead is

$$q_{\text{cond}} = \frac{kA[T_w - T_{\infty}]}{\sqrt{\pi\alpha\tau}} \quad (95)$$

where

T_{∞} = wire temperature at infinity \approx room temp

α'' = thermal diffusivity = $k/\rho C_p$

τ = time, sec

A = cross-sectional area of wire

Table IX lists the pertinent characteristics of the thermocouple lead wire.

TABLE IX. THERMOCOUPLE LEAD WIRE CHARACTERISTICS				
Type	$k = \left(\frac{\text{BTU}}{\text{sec, } ^\circ\text{R, ft}} \right)$	$\alpha'' \text{ (ft}^2\text{/sec)}$	Dia of Wire (in.)	$q_{\text{cond}} \text{ (BTU/sec)}$
Plat. 10% Rhod.	0.0048	0.0155	0.014	$1.99 \cdot 10^{-7} (T_w - 540)$ (96)
Plat.	0.0114	0.0311	0.014	$2.98 \cdot 10^{-7} (T_w - 540)$ (97)

Solving the above equations at time equal to 2 seconds gives the gas temperature as a function of the junction (wall) temperature and is shown in Figure 52.

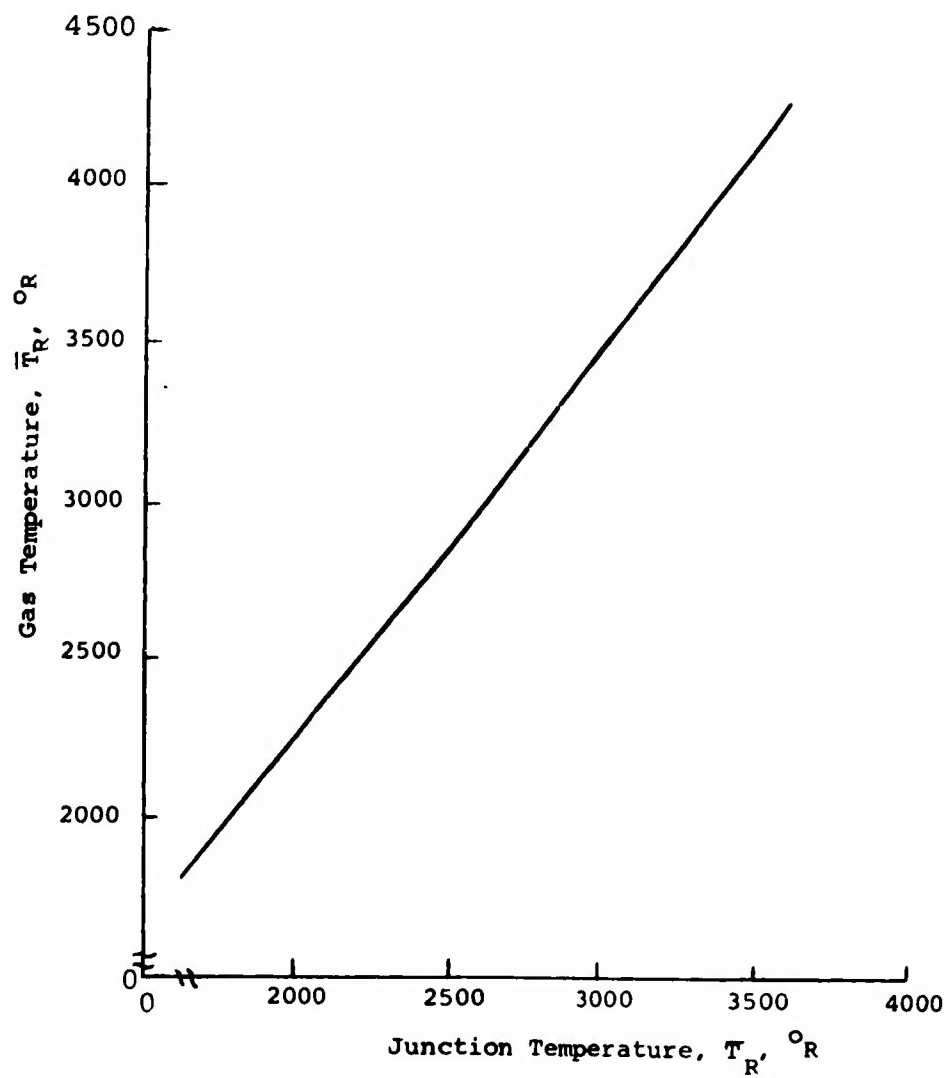


Figure 52. Thermocouple Probe Correction Chart.

APPENDIX VI
TOTAL TEMPERATURE DISTRIBUTION DATA

This section presents the experimental data associated with the total temperature distributions. Four sets of data are shown, corresponding to Figures 34 through 37.

The value T_R represents the measured temperature and \bar{T}_R is the value corrected with Figure 52.

TABLE X. DATA LOG: ALTITUDE, 100% POWER CONDITION									
Run	P_3 (psia)	T_3 (°R)	M_3	f/a	T_{af} (°R)	T_A			θ (deg)
						T_{R1} \bar{T}_{R1}	T_{R2} \bar{T}_{R2}	T_{R3} \bar{T}_{R3}	
30	73	1075	0.6	0.023	2500	2300 2600	2275 2590	2185 2500	30
63	70	965	0.42	0.022	2240	1810 2000	1870 2120	1810 2000	45
58	72	1005	0.57	0.022	2500	1730 1900	1840 2100	1765 2000	75
50	65	1010	0.57	0.022	2400	940 -	940 -	940 -	90
68	77	990	0.45	0.021	2300	1375	1285	1285	225

TABLE XI. DATA LOG: ALTITUDE, 60% POWER CONDITION									
Run	P ₃ (psia)	T ₃ (°R)	M ₃	f/a	T _{af} (°R)	T ₄			θ (deg)
						T _{R1} T _{R1}	T _{R2} T _{R2}	T _{R3} T _{R3}	
40	50	950	0.56	0.021	2240	2065 2340	2105 2380	1920 2150	30
64	55	920	0.57	0.012	1700	1460 -	1620 -	1540 -	45
59	53	980	0.57	0.018	2100	1650 1920	1700 2000	1675 1950	75
49	65	1010	0.57	0.022	2400	940 -	940 -	940 -	90
69	47	940	0.6	0.02	2200	940	940	940	225

TABLE XII. DATA LOG: SEA LEVEL, 100% POWER CONDITION									
Run	P ₃ (psia)	T ₃ (°R)	M ₃	f/a	T _{af} (°R)	T ₄			θ (deg)
						T _{R1} T _{R1}	T _{R2} T _{R2}	T _{R3} T _{R3}	
43	168.5	1157	0.64	0.033	3000	2770 3200	2860 3300	2800 3250	30
60	160	1050	0.60	0.019	2200	1785 2000	1815 2050	1730 1950	45
57	165	1040	0.59	0.018	2160	945 -	945 -	945 -	75
48	161	1070	0.59	0.018	2200	1140 -	1100 -	1100 -	90
65	167	1010	0.54	.0185	2200	1190 -	1190 -	1190 -	225

TABLE XIII. DATA LOG: SEA LEVEL, 60% POWER CONDITION									
Run	P ₃ (psia)	T ₃ (°R)	M ₃	f/a	T _{af} (°R)	T ₄			θ (deg)
						T _{R1} T _{R1}	T _{R2} T _{R2}	T _{R3} T _{R3}	
44	140	1100	0.66	0.013	1900	1800 2000	1835 2050	1760 1950	30
61	140	1080	0.60	0.015	2000	1745 1950	1810 2050	1745 1950	45
56	138	1085	0.59	0.016	2100	1285 -	1380 -	1450 -	75
45	132	1000	0.57	0.016	2020	945 -	945 -	945 -	90
67	133	1020	0.67	0.015	1950	940 -	940 -	940 -	225

UNCLASSIFIED

Security Classification		
DOCUMENT CONTROL DATA - R & D		
(Security classification of title, body of abstract and indexing annotation must be entered when the overall report is classified)		
1. ORIGINATING ACTIVITY (Corporate author) General Applied Science Laboratories, Inc. Merrick and Stewart Avenues Westbury, L.I., New York 11590		2a. REPORT SECURITY CLASSIFICATION Unclassified
		2b. GROUP
3. REPORT TITLE A FEASIBILITY STUDY OF A HIGH-SPEED BURNER		
4. DESCRIPTIVE NOTES (Type of report and inclusive dates) Final Report		
5. AUTHOR(S) (First name, middle initial, last name) Irving Fruchtman		
6. REPORT DATE February 1970	7a. TOTAL NO. OF PAGES 132	7b. NO. OF REFS 29
8a. CONTRACT OR GRANT NO. DAAJ02-68-C-0092	8b. ORIGINATOR'S REPORT NUMBER(S) USAAVIABS Technical Report 70-5	
8c. PROJECT NO. Task 1G162204A01409	8d. OTHER REPORT NO(S) (Any other numbers that may be assigned this report) GASL TR-730	
10. DISTRIBUTION STATEMENT This document is subject to special export controls, and each transmittal to foreign governments or foreign nationals may be made only with prior approval of U.S. Army Aviation Materiel Laboratories, Fort Eustis, Virginia 23604.		
11. SUPPLEMENTARY NOTES		12. SPONSORING MILITARY ACTIVITY U.S. Army Aviation Materiel Laboratories, Fort Eustis, Virginia 23604
13. ABSTRACT The theoretical analyses, the design, and the experimental verification of a high-speed combustion chamber are described. For turbomachines, this type of burner is used when compressor outflow speed is so high that diffusion to low speed presents severe pressure loss penalties. The present study showed that for a low-mass-flow, high-pressure-ratio turbomachine, combined diffuser and combustor losses are minimum for a burner entrance Mach number of about 0.5. The use of the GASL finite-rate chemistry and turbulent mixing programs is discussed along with the combustor modeling and flame spread predictions. Finally, a series of experiments is described, and burner pressure loss and temperature profiles are shown over a wide range of burner airflow conditions, i.e., pressures from 1 to 11 atmospheres and inlet air temperatures from ambient to 1200°R.		

DD FORM 1473

REPLACES DD FORM 1473, 1 JAN 64, WHICH IS OBSOLETE FOR ARMY USE.

UNCLASSIFIED

Security Classification

UNCLASSIFIED

Security Classification

14	KEY WORDS	LINK A		LINK B		LINK C	
		ROLE	WT	ROLE	WT	ROLE	WT
	Burner High-Speed Combustor Optimum Diffuser-Burner System Reacting Flow Prediction Experimental Verification						

UNCLASSIFIED

Security Classification